

Theory of hierarchically organized neuronal oscillator dynamics that mediate rodent rhythmic whisking

Highlights

- We model the hierarchical brainstem circuitry that generates rhythmic whisking
- The onset of inspiration drives the first whisk within a breathing cycle
- Subsequent whisks are generated by an autonomous, all-inhibitory neuronal oscillator
- Formulas describe the modularity of rhythmic control in terms of the known circuitry

Authors

David Golomb, Jeffrey D. Moore, Arash Fassihi, Jun Takatoh, Vincent Prevosto, Fan Wang, David Kleinfeld

Correspondence

golomb@bgu.ac.il (D.G.),
dk@physics.ucsd.edu (D.K.)

In brief

Rhythmic whisking is a prominent component of rodent behavior. Golomb et al. solve a hierarchical model of the whisking circuitry. The first whisk within a breathing cycle is derived from inhalation; subsequent whisks arise from an all-inhibitory oscillator. This framework supports longstanding observations of concurrent driven and autonomous motor actions.

Article

Theory of hierarchically organized neuronal oscillator dynamics that mediate rodent rhythmic whisking

David Golomb,^{1,2,3,9,*} Jeffrey D. Moore,⁴ Arash Fassihi,⁵ Jun Takatoh,⁶ Vincent Prevosto,⁶ Fan Wang,^{6,7} and David Kleinfeld^{5,8,*}

¹Department of Physiology and Cell Biology, Ben Gurion University, Be'er-Sheva 8410501, Israel

²Department of Physics, Ben Gurion University, Be'er-Sheva 8410501, Israel

³Zlotowski Center for Neuroscience, Ben Gurion University, Be'er-Sheva 8410501, Israel

⁴Department of Molecular and Cellular Biology, Harvard University, Cambridge, MA, USA

⁵Department of Physics, University of California at San Diego, La Jolla, CA 92093, USA

⁶Department of Brain and Cognitive Science, Massachusetts Institute of Technology, Cambridge, MA 02139, USA

⁷McGovern Institute, Massachusetts Institute of Technology, Cambridge, MA 02139, USA

⁸Department of Neurobiology, University of California at San Diego, La Jolla, CA 92093, USA

⁹Lead contact

*Correspondence: golomb@bgu.ac.il (D.G.), dk@physics.ucsd.edu (D.K.)

<https://doi.org/10.1016/j.neuron.2022.08.020>

SUMMARY

Rodents explore their environment through coordinated orofacial motor actions, including whisking. Whisking can free-run via an oscillator of inhibitory neurons in the medulla and can be paced by breathing. Yet, the mechanics of the whisking oscillator and its interaction with breathing remain to be understood. We formulate and solve a hierarchical model of the whisking circuit. The first whisk within a breathing cycle is generated by inhalation, which resets a vibrissa oscillator circuit, while subsequent whisks are derived from the oscillator circuit. Our model posits, consistent with experiment, that there are two subpopulations of oscillator neurons. Stronger connections between the subpopulations support rhythmicity, while connections within each subpopulation induce variable spike timing that enhances the dynamic range of rhythm generation. Calculated cycle-to-cycle changes in whisking are consistent with experiment. Our model provides a computational framework to support longstanding observations of concurrent autonomous and driven rhythmic motor actions that comprise behaviors.

INTRODUCTION

Motor output is the manifestation of an animal's behavior. How is this controlled through internal brain dynamics? The movement of an animal's body may be considered in terms of overlapping sequences of individual motor actions (Tinbergen, 1951). Each action is a movement primitive that involves the stereotypic activation of different muscles by premotor nuclei, along with potential adjustments of their activation by proprioceptive feedback (von Holst, 1939, 1973). The coordination of motor actions into behaviors nominally occurs through pre-premotor (pre²motor) nuclei, the next level in a hierarchy of neuronal control (Weiss, 1941; Mussa-Ivaldi and Bizzi, 2000; Moore et al., 2014b). Pre²motor nuclei are distributed across a plethora of motor centers, from the neocortical pre²motor outputs of infragranular projection neurons that appear to govern complex sequencing down to pre²motor nuclei in the brainstem and spinal cord that generate repetitive movements. Far from a rigid hierarchy, pre²motor nuclei can initiate behav-

iors that involve strong as well as partial coordination among motor actions (Kaplan et al., 2020).

The behaviors that comprise active orofacial sensation involve vibrissa touch, lingual touch, and smell. The underlying motor actions are driven by premotor nuclei in the brainstem for the control of whisking, licking, nose twitching, heading, and sniffing, the rapid breathing that occurs when a rodent forages or is otherwise attentive (Lund et al., 1998; Deschênes et al., 2012; Kurnikova et al., 2017; McElvain et al., 2018; Ruder and Arber, 2019). Of particular interest, orofacial motor actions have a rhythmic component and, further, are arranged in a tractable hierarchy (McElvain et al., 2018; Wallach et al., 2020). Inhalation, controlled by the preBötzing complex (pBötC) in the medulla (Smith et al., 1991), drives sniffing and further acts as a pre²motor master oscillator to many premotor nuclei that are involved in rhythmic orofacial motor actions (Moore et al., 2013; Kleinfeld et al., 2014a).

Rodents can rhythmically whisk over a broad range of frequencies (Berg and Kleinfeld, 2003; Carvell and Simons, 1990),

yet whisking is typically paced by breathing (Moore et al., 2013; Ranade et al., 2013; Welker, 1964) (Figure 1A). During sniffing, the breathing and whisking are phase-locked at a one-to-one ratio (Figure 1B). Whisking may also free-run between breaths, but the whisking cycle is rapidly reset by the onset of inhalation (Figures 1C and 1D). Beyond whisking per se, past work has identified the population of neurons that are both necessary and sufficient for whisking. These cells lie in a region denoted the ventral intermediate reticular zone (vIRt) that is adjacent to the pBötC (Moore et al., 2013; Deschênes et al., 2016b). Past work further identified the pattern of connectivity and the sign of their synaptic interactions (Moore et al., 2013; Deschênes et al., 2016b; Takatoh et al., 2013, 2021, 2022).

The goal of the present work is 2-fold. First, to decipher the underlying mechanisms for the generation of rhythmic whisking and breathing, where some cycles are different than other cycles in the rhythm. We analyze existing (Moore et al., 2013; Takatoh et al., 2022) and new experimental data. We then seek an analytically tractable model that encompasses past experimental results as well as provides insights to the hierarchical control of whisking from the pre²motor level down to the motion of the vibrissae. Second, to formulate a model that appears sufficiently general to answer the need, first posed by von Holst (1939, 1973), for a mechanism of partial coordination of rhythms involved in locomotion and exploratory, bodily movements. This need is amplified by the rebirth of attention to the multiplicity of inputs and feedback loops that govern motion, as reviewed by Merel et al. (2019).

Detailed background

Results from a variety of experimental procedures in both adult rats and mice indicate that the vast majority of neurons that comprise the vIRt release the inhibitory transmitter GABA or glycine. Juxtacellular recording from vIRt neurons, followed by *in situ* hybridization, showed that nine of ten cells were GABAergic, while one was glutamatergic (Deschênes et al., 2016b); i.e., 0.9 of vIRt neurons are inhibitory. Retrograde labeling experiments from the vibrissa facial motor nucleus (vFMN) to the vIRt using the organic dye fluoro-gold, followed by *in situ* hybridization (≈ 300 neurons), showed that 0.86 of double labeled cells are glycinergic, 0.54 are GABAergic, and 0.13 are glutamatergic (Moore et al., 2013); i.e., a complementary measurement shows that 0.9 of vIRt neurons are inhibitory. Transsynaptic retrograde labeling experiments based on glycoprotein-deleted rabies (Takatoh et al., 2021), followed by *in situ* hybridization (≈ 600 neurons), found that 0.67 are GABAergic and 0.30 are glutamatergic (Takatoh et al., 2022), i.e., 0.7 of vIRt neurons are inhibitory. Of critical importance, removal of the glutamatergic neurons does not impact the rhythm generation by the vIRt oscillator (Takatoh et al., 2022). Further, inhibitory vIRt neurons form connections among each other (Takatoh et al., 2021). In our model, we take the vIRt to contain solely interconnected inhibitory cells.

Pharmacologically isolated inhibitory neurons in the vIRt appear to spike at a uniform rate; they are not intrinsic “bursting” (Takatoh et al., 2021). Nor, under normal conditions, is there evidence that the rate of spiking by individual vIRt neurons occurs at the whisking frequency. Rather, vIRt neurons are observed to

produce bursts of spikes either in phase with vibrissa protraction or in phase with vibrissa retraction (Moore et al., 2013; Deschênes et al., 2016b; Takatoh et al., 2022); we label these two populations vIRt^{pro} and vIRt^{ret}, respectively. The neurons that spike in phase with retraction form the dominant premotor input to the vFMN neurons that drive the intrinsic muscles in the mystacial pad and protract the vibrissae (Deschênes et al., 2016b). Thus the premotor vIRt^{ret} input acts to shunt or negate motoneuron output. This implies that the onset of whisking requires a concomitant excitatory input to the vFMN neurons.

Selective physical or chemical lesion of neurons (Moore et al., 2013), or near-complete inactivation of vIRt synapses by the expression of tetanus light chain in parvalbumin neurons (Takatoh et al., 2022), abolishes whisking on the side of the lesion. These procedures maintain modulation of the set point (Kleinfeld et al., 2014b; Takatoh et al., 2022). In other experiments, pharmacological activation of the vIRt induces long epochs of continuous whisking on the ipsilateral side in the lightly anesthetized rodent (Moore et al., 2013, 2014a). These results indicate that the vIRt is both necessary and sufficient to generate the whisking rhythm independent of breathing.

A breathing cycle in rodents may initiate one whisking cycle that is locked to breathing, or multiple whisking cycles. When whisking and sniffing approximately synchronize at a 1:1 ratio during exploration, a special case but one that is behaviorally relevant, it is useful to describe the vibrissa angle, $\theta(t)$, by an idealized representation (Hill et al., 2011; Kleinfeld and Deschênes, 2011). Here,

$$\theta(t) = \theta^{\text{set}}(t) - \theta^{\text{amp}}(t)[1 + \cos \varphi(t)] \quad (\text{Equation 1})$$

where θ^{set} is the slowly varying set point, which corresponds to full protraction of the vibrissae, and θ^{amp} is the slowly varying amplitude of the rhythmic sweep. The rapidly varying phase in the whisk cycle, denoted $\varphi(t)$, is found from

$$\left\langle \frac{d\varphi(t)}{dt} \right\rangle_t = 2\pi f_{\text{pBötC}}, \quad (\text{Equation 2})$$

where $f_{\text{pBötC}}$ is the frequency of the pBötC input to the vIRt^{ret}, and also the whisking frequency in this case, and $\langle \dots \rangle_t$ means time-averaging. These model parameters can be compared with values of θ^{set} , θ^{amp} , and $\varphi(t)$ that are extracted from experimental measurements of whisking through the use of a Hilbert transform (Hill et al., 2011).

For the case of several whisking cycles within a single breathing cycle, the extra whisks are known as intervening whisks (Moore et al., 2013) (Figure 1E). Measurements with head-fixed rodents show that the onset of the first whisk is locked to the onset of inhalation. However, the timing of the subsequent whisks slowly drifts, i.e., whisking is unlocked from breathing and even whisking on the two sides of the face dephases between breaths (Moore et al., 2013; Deschênes et al., 2016b). The amplitude of the intervening whisks is concomitantly reduced. The whisks are resynchronized at the next inhalation (Moore et al., 2013; Deschênes et al., 2016b) (Figure 1E). This is an example of partial coordination posed by von Holst, (1939, 1973). The occurrence of intervening whisks between bouts of inhalation implies that both inhibitory input from the

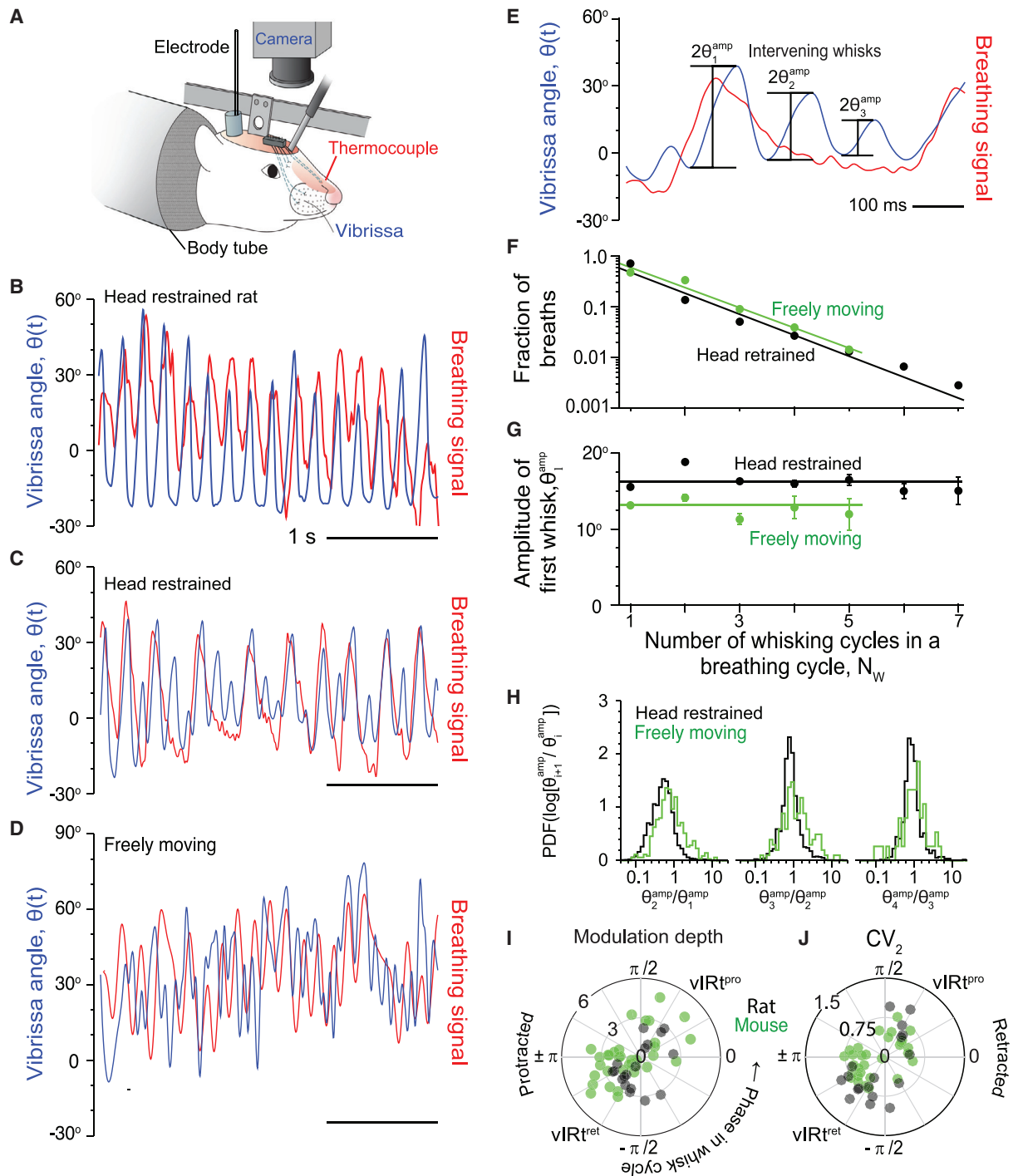


Figure 1. Analysis of existing and new data related to breathing and whisking

(A) Typical experimental setup for recording from head-restrained rodents.

(B and C) Time series of breathing (red) and whisking (blue) for a head-restrained rat (Moore et al., 2013).

(D) Time series of breathing (red) and whisking (blue) for a free moving rat.

(E) Annotated whisking and breathing. The values θ_1^{amp} , θ_2^{amp} , and θ_3^{amp} denote the amplitudes of the first, second, and third whisks within the same breathing cycle.

(F) Semi-logarithmic plot of the number of breaths for which there are N_W whisking cycles. The dotted lines are exponential fits with slopes of 0.95 (restrained; four female Long Evans rats, 250–350 g) (Moore et al., 2013) and 0.92 (free; new data).

(G) Amplitude of the first whisk θ_1^{amp} within a breathing cycle versus N_W . Bars denote the standard error.

(legend continued on next page)

pBötC and inhibitory interactions within the vIRt contribute to whisking rhythmogenesis. Of interest, a molecular manipulation to diminish the conductance of inhibitory inputs solely to vIRt^{ret} cells reduces the amplitude of whisking, quenches the occurrence of intervening whisks, yet preserves the locking of whisking to breathing (Takatoh et al., 2022).

With respect to descending control, vIRt neurons receive excitatory inputs from superior colliculus (Kaneshige et al., 2018; McElvain et al., 2018), deep cerebellar nucleus (Takatoh et al., 2021, 2022), and a midbrain reticular region near the red nucleus (Takatoh et al., 2022). Recordings from photo-tagged vIRt cells reveals a transition from either quiescence or tonic spiking to rhythmic bursts of spikes (Takatoh et al., 2022). It is an open issue as to whether the same projections to vIRt neurons depolarizes the vFMN neurons.

Computational challenges

The experimental observations raise computational challenges. We ask (1) how does the rodent generate robust, rhythmic whisking that can lock to breathing as well as free-run between breaths? This addresses the issue of partial correlation of the whisking and breathing. (2) How can an oscillator that generates periodic bursts of action potentials be constructed from solely inhibitory neurons? Networks with all-inhibitory synapses typically produce two types of bursting patterns. One type is network-wide asynchronous bursts of spikes (Golomb, 2007; Golomb and Rinzel, 1993), which is not observed for the vIRt. Another type is bursts of spikes that alternate among different clusters of neurons whose membership may evolve over time (Golomb and Rinzel, 1994; Golomb et al., 2001). In contrast, the vIRt oscillator requires two fixed populations of neurons that alternately produce bursts of spikes. In considering this issue, it is important to recall that inhibition can synchronize single spikes between pairs of neurons if the synapses are sufficiently fast (Chow and Kopell, 2000; Van Vreeswijk et al., 1994). This is different than the current case, where we study synchronization of bursts of spikes across neurons that are not intrinsic bursters. (3) How can we achieve high variability in the spiking patterns of vIRt neurons, recalling that variability is associated with asynchronous dynamics (van Vreeswijk and Sompolinsky, 1996, 1998) as opposed to oscillations. The experimental observation that the spiking pattern of vIRt neurons is irregular will have implications with regard to the patterns of connectivity among vIRt neurons. Further, what improvements in functional output are achieved, if any, by variability in the output of the circuit (Pehlevan and Sompolinsky, 2014)?

To address these questions, we construct a circuit model of the vIRt that incorporates the known anatomical connections, spiking and synaptic properties of the associated neurons, and the interaction of the vIRt with the pBötC and the vFMN. The ar-

chitecture of the model is similar to that used in studies of binocular rivalry: Wilson (2003) and Shpiro et al. (2007), albeit with different neuronal gain functions, and Soloduchin and Shamir (2018). We formulate our model with conductance-based equations for “realistic” neurons. Yet, as our goal is to identify key parameters that control rhythmic whisking and the interaction of the pBötC and vIRt oscillators. We apply averaging of the currents generated by the spiking output of neurons and reduce this model to analytical expressions for the time-dependent spike rate within populations of the underlying neurons.

RESULTS

Experiments

Hypotheses for the generation and synchrony of bursts of spikes in the vIRt

Two hypotheses may explain the generation and synchrony of bursts of spikes in vIRt neuronal populations. One is that the input from pBötC is necessary to drive and synchronize bursts of spikes in vIRt neurons, which implicitly entrains whisking to the breathing rhythm. Consequently, whisking oscillations should vanish, or at least decay, after each input from the pBötC. A second hypothesis is that rhythmic bursts of spikes are generated and synchronized by the inhibitory interactions among vIRt neurons. Under this scenario, synchrony of spiking between individual neurons within the vIRt can prevail without input from the pBötC; external input is necessary only to lock the whisk cycle to the breathing rhythm. These hypotheses are not exclusive. Whisking is synchronized to breathing, yet whisking can be pharmacologically induced independent of breathing (Moore et al., 2013, 2014a; Deschênes et al., 2016b). Furthermore, whisking can occur for many cycles after onset of inhalation (Moore et al., 2013; Deschênes et al., 2016b); in this case the amplitude of the so-called intervening whisks appear to decay following inhalation (Figure 7 in Deschênes et al. [2016b]). Thus, it is possible that the input from the pBötC synchronizes neurons the vIRt, yet, in addition, these neurons may also synchronize on their own.

Intervening whisks occur between breaths and are weaker than the inhalation locked breath

We aim to determine which of the above two hypotheses is most consistent with experimental observations. If input from pBötC is necessary to drive oscillations, the amplitudes of intervening whisks should decay with time from the most recent inhalation. If rhythmic bursts of spikes are generated and synchronized solely by vIRt neurons, the amplitudes of consecutive whisks should not decay. To resolve the mechanism, we reanalyzed the data on whisking by head-restrained rats (Moore et al., 2013) (Figures 1B and 1C) and obtained and analyzed new data on whisking by freely moving rats (Figure 1D). Angular

(H) Probability density function of $\log(\theta_{i+1}^{\text{amp}}/\theta_i^{\text{amp}})$ versus θ_i^{amp} for $i = 1, 2, 3$. The normalization of each distribution is $\int_{-\infty}^{\infty} d[\log(\theta_{i+1}^{\text{amp}}/\theta_i^{\text{amp}})] \log(\theta_{i+1}^{\text{amp}}/\theta_i^{\text{amp}}) = 1$.

(I) Modulation depth of the spike rates of vIRt neurons. Black circles are from intracellular recordings with lightly anesthetized rats (6 female Long Evans rats, 250–350-g 18 cells) (Deschênes et al., 2016b). Green circles are from extracellular recordings from optically tagged cells in awake mice (six female C57BL/6 mice, 20–22 g) (Takatoh et al., 2022). The depth is calculated from the spike rates as $(\text{minimum} - \text{maximum})/\text{average}$ where the averaging is on a per cycle basis. Data plotted as a function of the phase in the whisk cycle at which the spike rate is maximal.

(J) New analysis to determine the coefficient of variation CV_2 as a function of the phase in the whisk cycle. Same data and notations as in (I), except that CV_2 could be calculated for only 30 of 35 recordings from mice.

amplitudes of consecutive whisks during one breathing cycle are denoted by $\theta_1^{\text{amp}}, \theta_2^{\text{amp}}, \dots, \theta_{N_W}^{\text{amp}}$ (Figure 1E), where N_W is the number of whisks in a breathing cycle. We observe that the number of breathing cycles that includes N_W whisking cycles decreases exponentially, with almost identical decay constants for head-restrained and freely moving rats (Figure 1F). Further, θ_1^{amp} is essentially the same for the two behavioral conditions, with $\theta_1^{\text{amp}} \approx 15^\circ$ (Figure 1G). These findings add to past work that showed a slight reduction in whisking frequency with head fixation (Berg and Kleinfeld, 2003). Thus head fixation quantitatively but not qualitatively affects the amplitude of whisking.

We computed the probability distribution function (PDF) of the ratio $\theta_{i+1}^{\text{amp}} / \theta_i^{\text{amp}}$ as a means to quantify the average dependence of the amplitude on the index, i (Figure 1H). We observe that the amplitude of the second whisk after a breath, i.e., θ_2^{amp} , is smaller than the amplitude directly affected by input from the pBötC, i.e., θ_1^{amp} . The amplitude of successive whisks asymptotes to a constant value, approximated by $\theta_4^{\text{amp}} / \theta_1^{\text{amp}} = 0.43$ for head-restrained rats and $\theta_4^{\text{amp}} / \theta_1^{\text{amp}} = 0.64$ for freely moving rats. The diminished steady-state amplitude applies to whisks generated solely by the vIRt, as opposed to driven by the pBötC. It indicates that the vIRt can generate sustained oscillations without input from the pBötC.

Analysis of spiking during “bursts” reveals irregular spike timing

The variability in spike timing of neurons in a circuit provides clues to the nature and extent of the underlying synaptic connections (Rosenbaum et al., 2017). Specifically, if the synaptic coupling within each subpopulation, vIRt^{pro} or vIRt^{ret}, is small, neurons in the nuclei are expected to spike regularly because they receive input that varies only weakly with time (Softky and Koch, 1993). If the coupling within a subpopulation is strong, neurons may spike irregularly (van Vreeswijk and Sompolinsky, 1996; Renart et al., 2010). Previous work reported that individual vIRt neurons preferred to spike upon retraction versus protraction of the vibrissae in rats (Deschênes et al., 2016b, 2016a) (Figure 1I). We now calculated the spike-to-spike variability of these individual vIRt^{pro} and vIRt^{ret} neurons during the inter-spike intervals within bursts (Figure 1J). Our metric is the coefficient of variation CV_2 (Holt et al., 1996). We find that $CV_2 = 0.75 \pm 0.05$ (mean \pm SEM). We also calculate CV_2 from extracellular recordings of inhibitory neurons in the vIRt of mice (Takato et al., 2022) and find that $CV_2 = 0.55 \pm 0.02$. These relatively large values imply that the timing of spikes from individual vIRt neurons is irregular during a burst.

Circuit model

Architecture

Our model of the circuit for rhythmic whisking consists of the vIRt per se and the motoneurons in the vFMN that drive the intrinsic vibrissa muscles, along with rhythmic input from the pBötC and constant input from a high-order excitatory drive (Figure 2; STAR Methods). In the absence of a connectome for the vIRt oscillator, we base the architecture on the observed segregation of vIRt neurons into two functional clusters, i.e., the vIRt^{ret} and vIRt^{pro} subpopulations (Figure 2A). There are N neurons in

each population. The probability that a neuron from one population is inhibited by a neuron from the same or the second population is given by the fraction K/N , where K is smaller than but of order N . We take the architecture to be symmetric, so the strength of individual synapses within a subpopulation of vIRt neurons, i.e., between pairs of vIRt^{ret} neurons and between pairs of vIRt^{pro} neurons, is g_{intra} . Similarly, we assume that the strength of individual synapses between neurons in the two subpopulations, i.e., between a pair of vIRt^{ret} and vIRt^{pro} neurons, is symmetric with g_{inter} .

The observation that the vIRt^{ret} and vIRt^{pro} subpopulations are active in anti-phase supports the choice that vIRt^{ret} neurons, but not the vIRt^{pro} neurons, receive rhythmic inhibitory input from the pBötC. Since the vIRt neurons are inhibitory, this is consistent with potential synchrony of breathing and whisking. The vIRt^{ret} neurons rhythmically inhibit neurons in the vFMN. With this architecture, vIRt^{ret} neurons are inhibited during pBötC activity, and vIRt^{pro} and vFMN neurons are active. In addition, all neurons receive a constant depolarizing input, denoted I_{ext}^r for the vIRt^{ret} and vIRt^{pro} subpopulations and I_{ext}^f for the vFMN population. This completes the neuronal circuit (Figure 2A).

Single neuron, motoneuron, and vibrissa dynamics

Single neurons in the vIRt and the vFMN are represented by conductance-based schemes (Figure 2B). In addition to spike-generating ionic channels, we require that vIRt neurons possess slow internal dynamics as a means to produce bursts of spikes. The parsimonious solution is to include a slow K^+ -channel that causes spike-frequency adaptation (Soloduchin and Shamir, 2018). The conductances and adaptation time constants of these channels are g_{adapt}^r and τ_a^r for all vIRt neurons and g_{adapt}^f and τ_a^f for vFMN neurons. These currents naturally occur in vFMN neurons (Magarinos-Ascoñe et al., 1999; Nguyen et al., 2004).

The spike rate versus input current relation, i.e., $f-I_{\text{ext}}^r$ curve, for vIRt neurons with various values of g_{adapt}^r show that the $f-I_{\text{ext}}^r$ curve rises linearly just above the current threshold I_0^r for a sufficiently large value of g_{adapt}^r (Shriki et al., 2003) (Figure 2C). The transformation from the spiking patterns of vFMN neurons to vibrissa movement is calculated with the use of a simplified version of a mechanical model (Simony et al., 2010) (Figure 2D). We exploit the slow timescale of the adaptation current, the self-consistent assumptions of asynchronous spike activity, and the near-constant external inputs to the neurons to develop a rate model for spiking (Figure 2E).

Whisking paced by rhythmic inhibition from the pBötC

A first mode of whisking makes use of the vIRt^{ret} as a relay and nonlinear filter. The synchronous drive of whisking by input from pBötC to the vIRt^{ret}, that, in turn, inhibits neurons in the vFMN, i.e., “inhibition of inhibition,” provides near synchrony of inhalation and whisking (Figure 1B). Beyond this qualitative description, we analyzed a minimal model with only feedforward connections from the pBötC to the vIRt^{ret} and from the vIRt^{ret} to the vFMN (Figure 3A). Numerical simulation of the conductance-based equations (Equations 16, 17, 18, 19, 20, 21, 22, 23, 24, 25, 26, 27, 28, 29, 30, and 31 in STAR Methods) for sets of physiologically plausible parameters show that vIRt^{ret} neurons are silenced during spiking of the pBötC (Figures 3B and 3C). This

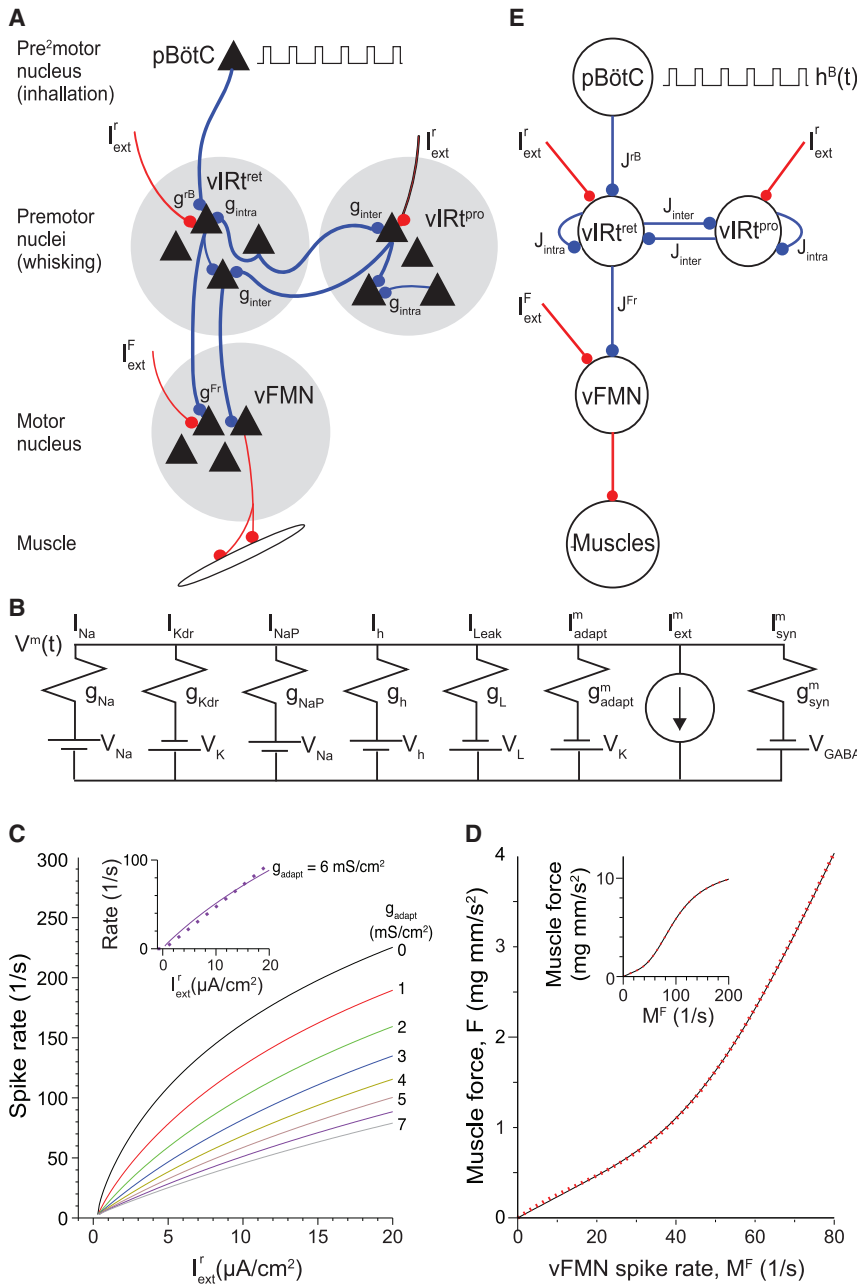


Figure 2. Architecture of the brainstem circuit model for whisking

(A) The neuronal-level circuit for conductance-based modeling. The triangles are neurons. The blue and red colors denote inhibitory and excitatory connections, respectively. The currents I_{ext}^r and I_{ext}^F represent constant external depolarizing input to the vIRt and vFNM neuronal populations, respectively. Conductances between neuronal pairs are denoted by g_{intra} for pairs of neurons that belong to the same subpopulation, by g_{inter} for neuronal pairs from two different subpopulations, and by g_{Fr} for vIRt^{ret}-to-vFNM connections. The amplitude of the square-wave pBötC-to-vIRt^{ret} input is denoted by g^{rB} .

(B) Schematic of the different currents in the cellular model for vIRt cells; the same model applies to vFNM neurons with possibly different conductances. The currents are a leak current, I_L , the transient sodium current, I_{Na} , the delayed rectifier potassium current, I_{Kdr} , the persistent sodium current I_{NaP} , the mixed cation h-current, I_h , an M-type K^+ current, I_{adapt} , external excitatory currents from other brain areas, I_{ext} and synaptic currents I_{syn} that comprise I_{intra} , I_{inter} and I^{Fr} . Details in [STAR Methods](#).

(C) Spiking rate versus I_{ext}^r curves of the single vIRt neuron model for values of g_{adapt} that range from 0 to 7 mS/cm². The insert is for $g_{adapt} = 6$ mS/cm² with the spike rate versus I_{ext}^r curve as solid and a linear approximation as dotted, as used in the rate model.

(D) The force developed by an intrinsic muscle that moves vibrissae as a function of the average spike rate of vFNM neurons, M^F . The solid black line denotes simulation results, and the dotted red line denotes a fit. Details in [STAR Methods](#).

(E) Schematic of the rate model in which each population of neurons is described by an activation variable that controls its synaptic outputs, and another activation variable that controls the adaptation current. The interactions J_{intra} and J_{inter} replace g_{intra} and g_{inter} , respectively.

of whisking depend on specific cellular and extrinsic parameters, both here and later in the description of autonomous oscillations. We find that the average number of spikes produced during the time interval of pBötC activity by a vIRt^{ret} neuron

silencing leads to heightened spiking in vFNM neurons and concurrent large amplitudes of rhythmic whisking (Figures 3B–3D).

Conversion to a rate model

We reduced the conductance equations to a rate model (“summary of the rate model” in [STAR Methods](#) and Equations 32, 33, 34, 35, 36, 37, 38, 39, 40, 41, 42, 43, 44, 45, and 46) to gain insight into the behavior of the feedforward circuit (Equations 47, 48, 49, 50, 51, 52, 53, 54, 55, 56, 57, 58, 59, 60, 61, 62, 63, 64, 65, 66, 67, 68, 69, 70, 71, 72, 73, 74, 75, 76, 77, 78, 79, 80, 81, 82, 83, 84, 85, 86, 87, 88, 89, 90, 91, 92, 93, 94, 95, and 96; Figure S1). This is a crucial aspect of our analysis. It provides the framework, and formulas, to determine how different aspects

is an approximately linearly decreasing function of the pBötC to vIRt total synaptic strength, g^{rB} , until the value of the strength reaches zero (Equations 62, 63, 77, and 85) (Figures 3E and 3F; analysis is confirmed by numerical simulations of the conductance-based model). Conversely, the activity of the vFNM neurons is a linearly increasing function of g^{rB} between a threshold value and a saturation value of g^{rB} (Equations 72, 73, 80, 81, 82, and 86; Figure 3G). The whisking amplitude increases with increasing values of g^{rB} , above threshold, until a saturated value is reached (Figure 3H).

Our rate-based analysis (“summary of the rate model” in [STAR Methods](#); Figure S1) highlights the competition between

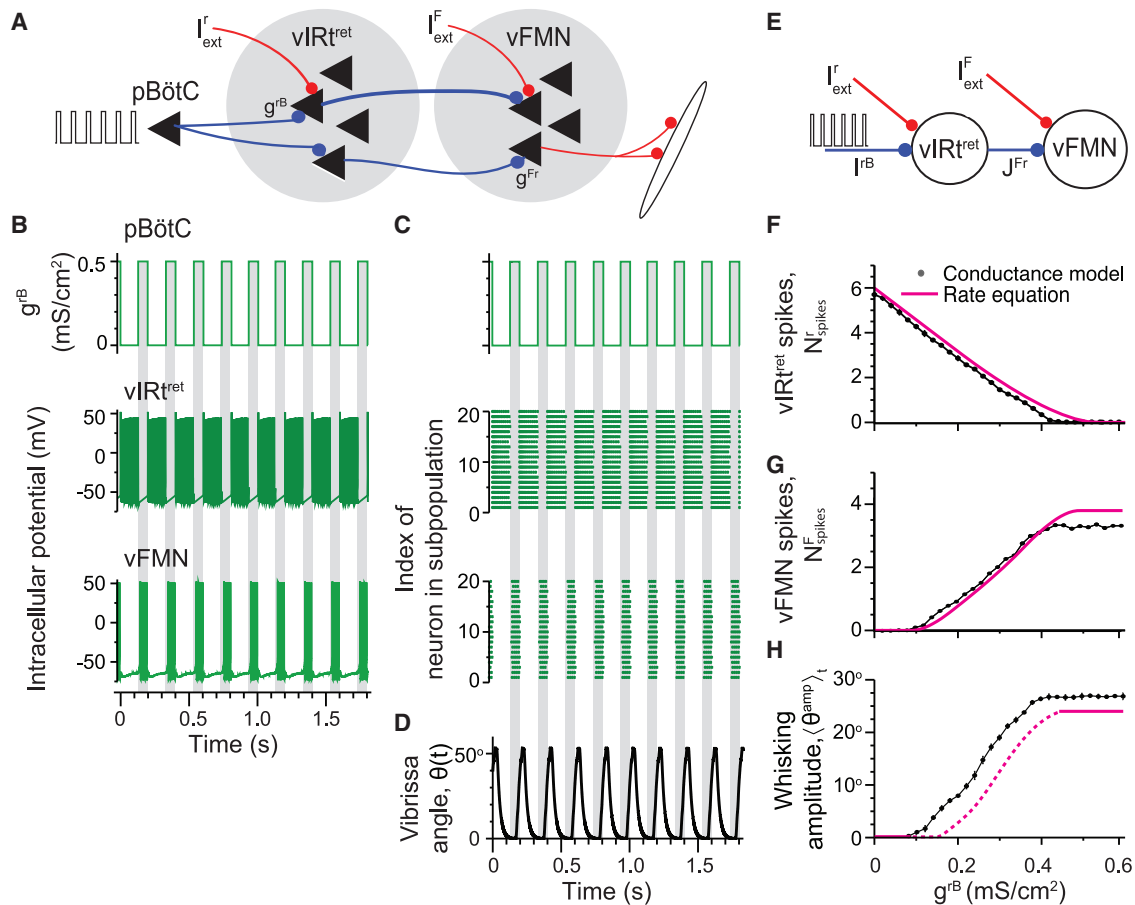


Figure 3. Dynamics of a conductance-based and rate-based feedforward circuit for whisking

(A) Schematic of the conductance-based circuit with input from the pBötC to the vIRt^{ret} and from the vIRt^{ret} to the vFMN to drive whisking. The vIRt^{pro} subpopulation plays no role. We further set $g_{intra} = 0$. We chose $g^B = 0.5$ mS/cm², $g_{Fr} = 0.12$ mS/cm², $I_{ext}^r = 20$ μ A/cm², $I_{ext}^F = 3.1$ μ A/cm², $K = 25$, $g_{adapt}^r = 7$ mS/cm², $g_{adapt}^F = 0.3$ mS/cm², $N = 100$, $T_{pBötC} = 200$ ms, $T_{rand} = 10$ ms, $\Delta T_{vIRt} = 70$ ms. Details of all calculations are in [STAR Methods](#).

(B) Time courses of spiking for an example neuron from the vIRt^{ret} and vFMN subpopulations.

(C) Rastergrams across twenty neurons in the simulated subpopulations.

(D) The calculated vibrissa angle $\theta(t)$, calculated with the model of the motor plant and common parameters.

(E) The reduced rate-based circuit with input from the pBötC to the vIRt^{ret} and from the vIRt^{ret} to the vFMN to drive whisking.

(F–H) Circuit properties as the synaptic conductance from the pBötC is increased. Parameters are as in (A), except that g^B is varied. Properties are computed using three modeling strategies. First, by numerical simulations of the conductance-based model (solid black line and circles). Simulations were carried out over five realizations for each parameter set, and the error bars denote standard deviation. Second, by numerical simulations of the rate model equations (dotted magenta line). Third, from analytical solution of the rate model (solid magenta line). The average number of spikes produced by the vIRt^{ret} neurons per whisk is shown in (F). The average number of spikes produced by vFMN neurons per whisk is shown in (G). The average amplitude of each whisk is shown in (H).

the excitatory drive, i.e., $I_{ext}^r - I_0^r$, and the rhythmic inhibition from the pBötC in determining the amplitude of a whisk. When g^B is moderate in magnitude, the vIRt^{ret} neurons cease to spike just after the beginning of the pBötC activity. In contrast, when g^B is sufficiently large the vIRt^{ret} neurons are silent during the entire period of pBötC activity. The essential lesson is that the whisking frequency and amplitude decouple.

Turning to the motor output, the number of spikes produced by vFMN neurons is zero below a minimum value of g^B . The number reaches a saturation level if and when vIRt^{ret} neurons become completely silent during pBötC activity. Between these two values the number, denoted N_{spikes}^F , increases monotonically

and near linearly as a function of g^B . The whisking amplitude depends on the muscular force that moves the vibrissae and this too increases monotonically with N_{spikes}^F . We conclude that the disinhibitory mechanism of whisking leads to a sigmoid dependence of the maximum protraction angle on the pBötC activity strength.

Rhythmic whisking without input from the pBötC

A second mode of whisking depends on the viability of the vIRt circuit alone to function as a stand-alone oscillator and drive rhythmic whisking via the projection from vIRt^{ret} neurons to those in the vFMN neurons (Figure 4A). This subsystem is solely

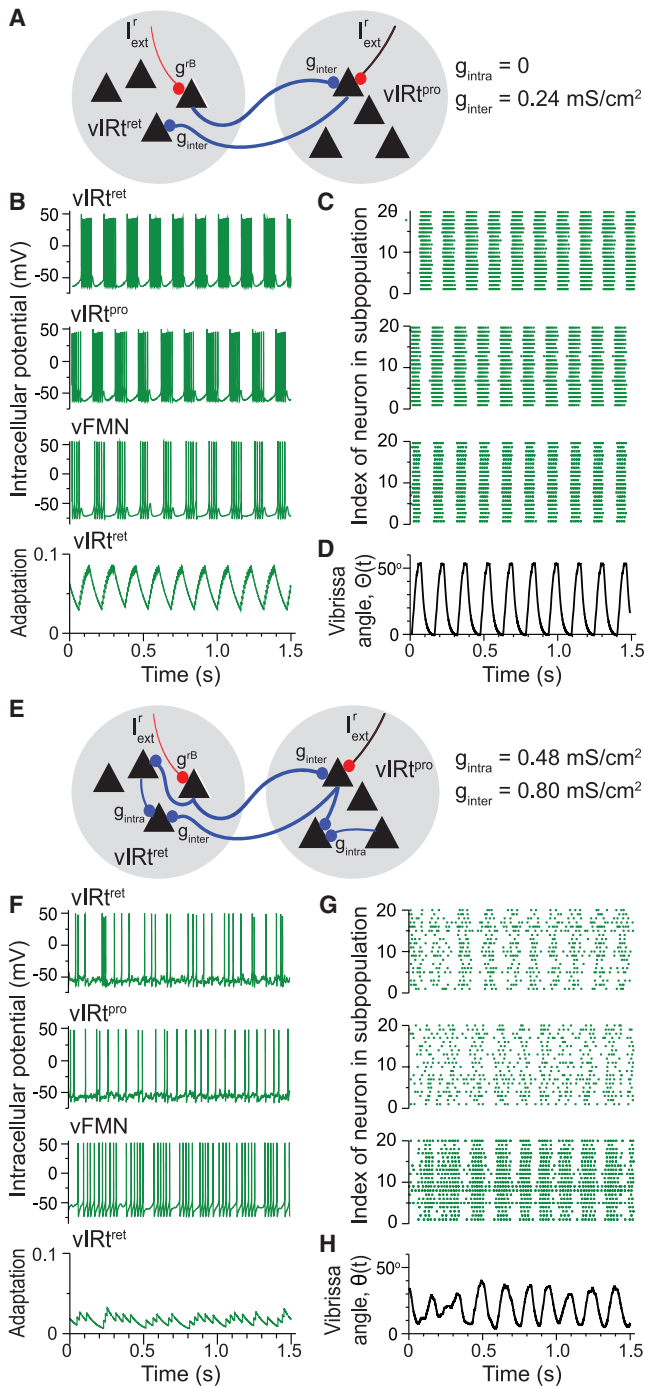


Figure 4. Dynamics of conductance-based circuits without pBötC input to the vIRt

(A) Schematic of the circuit with connections only between vIRt^{ret} and vIRt^{pro} subpopulations, for which we set $g_{intra} = 0$. We chose $g_{inter} = 0.24 \text{ mS/cm}^2$, $g_{adapt} = 7 \text{ mS/cm}^2$, $I_{ext} = 20 \text{ } \mu\text{A/cm}^2$, $K = 25$, and $N = 100$.

(B) Time courses of spiking for an example neuron from the vIRt^{ret}, vIRt^{pro}, and vFMN subpopulations.

(C) Rastergrams across twenty neurons in the simulated subpopulations.

(D) The calculated vibrissa angle $\theta(t)$ with the model of the motor plant.

(E) Schematic of the circuit with connections both between vIRt^{ret} and vIRt^{pro} subpopulations and within each subpopulation, for which

we set $g_{intra} = 0.48 \text{ mS/cm}^2$ and $g_{inter} = 0.80 \text{ mS/cm}^2$; other parameters as in (A). (F) Time courses of spiking for an example neurons for the vIRt^{ret}, vIRt^{pro}, and vFMN subpopulations. (G) Rastergrams across twenty neurons in the simulated subpopulations. (H) The calculated vibrissa angle $\theta(t)$.

responsible for intervening whisks. A minimal circuit contains only connections between the vIRt^{ret} and vIRt^{pro} subpopulations, i.e., $g_{inter} \neq 0$ but $g_{intra} = 0$. Individual neurons in this two-subpopulation system can generate alternating burst of spikes (Figure 4B). The network robustly oscillates at physiological frequencies, as seen in the spike raster plots and in the rhythmic cycling of the calculated vibrissa motion (Figures 4C and 4D). Of note, the two subpopulations alternate between regular spiking and quiescence; variability within the spike trains is small (Figure S2). This minimal circuit captures the desired rhythmic output of vIRt neurons, but not the observed variability (Figure 1J).

The spiking patterns of vIRt neurons becomes irregular when intra-neuronal connections are added within each subpopulation, i.e., $g_{inter} \neq 0$ and $g_{intra} \neq 0$, with $CV_2 = 0.5$ for the example of Figures 4E and 4F. Neurons in the two subpopulations spike throughout both halves of the whisking cycle (Figure 4G), but with a bias so that the summed activity across many neurons leads to a rhythmic albeit noisy trajectory of whisking (Figure 4H). This simulated activity is similar to most experimentally observed trajectories (Moore et al., 2013; Deschênes et al., 2016b) (Figures 1B–1D). Based on these numerical results, we focus on the analysis of a circuit for the vIRt that includes both inter- and intra-neuronal connections (Figure 5A).

Three modes of vIRt dynamics: uniform, oscillatory and bistable

The analysis of the rate equations (“summary of the rate model” in STAR Methods and Equations 97, 98, 99, 100, 101, 102, 103, 104, 105, 106, 107, 108, 109, 110, 111, 112, 113, 114, 115, 116, 117, 118, 119, 120, 121, 122, 123, 124, 125, 126, 127, 128, 129, 130, 131, 132, 133, 134, 135, 136, 137, 138, and 139) yields insights to the dependence of whisking on network parameters (Figure 5). There are three forms of output dynamics as a function of the difference in conductances

$$\Delta g_{syn} = g_{inter} - g_{intra} \quad (\text{Equation 3})$$

When Δg_{syn} is smaller than a critical value, denoted g_{tr} , neurons within both the vIRt^{ret} and vIRt^{pro} subpopulations are tonically active (Figure 5B). The average spiking activity of the vIRt^{ret} subpopulation is equal to that of the vIRt^{pro} subpopulation and is a weakly decreasing function of Δg_{syn} (Figure 5B). Thus, the vIRt does not drive rhythmic whisking (Figure 5D). When Δg_{syn} is increased to surpass g_{tr} but remain smaller than a second critical value, denoted g_{det} , neurons within the vIRt^{ret} and vIRt^{pro} subpopulations alternate in their activity (Figures 5B–5D). Thus, the vIRt functions as an oscillator. While the average spiking activity is a weakly decreasing function of Δg_{syn} (Figure 5B), the amplitude of whisking increases monotonically as a function of $I_{ext} - I_0$ until saturation is reached (Figure 5E). As Δg_{syn} increases further so that it surpasses g_{det} , the output ceases to

we set $g_{intra} = 0.48 \text{ mS/cm}^2$ and $g_{inter} = 0.8 \text{ mS/cm}^2$; other parameters as in (A).

(F) Time courses of spiking for an example neurons for the vIRt^{ret}, vIRt^{pro}, and vFMN subpopulations.

(G) Rastergrams across twenty neurons in the simulated subpopulations.

(H) The calculated vibrissa angle $\theta(t)$.

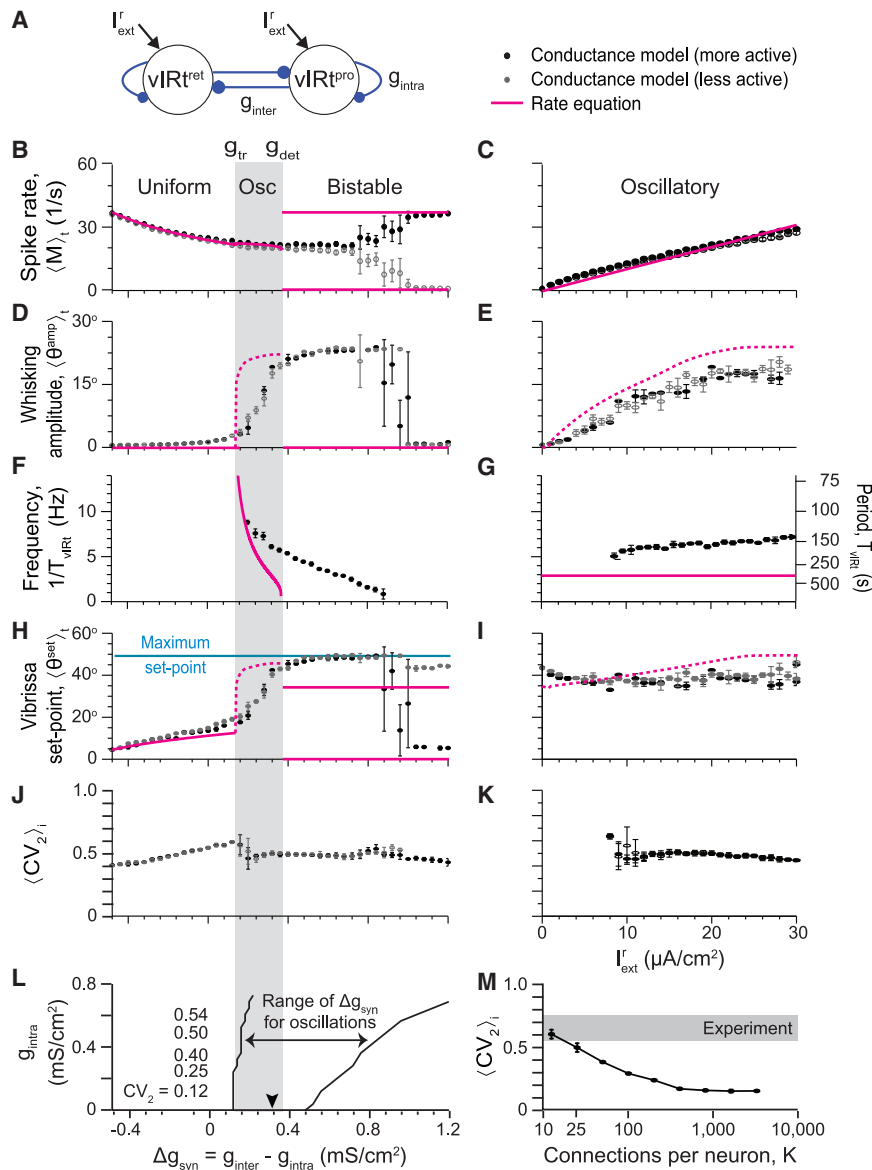


Figure 5. Dynamical properties of circuits without pBötC input to the vIRT

(A) Schematic of the circuit. The dynamics are calculated for $g_{intra} = 0.48$ mS/cm², $g_{adapt} = 7$ mS/cm², $g_{adapt}^F = 0.3$ mS/cm², $I_{ext}^r = 3.1$ μ A/cm², and $K = 25$. The excitatory input fixed at $I_{ext}^r = 20$ μ A/cm² and g_{inter} is varied in terms of $\Delta g_{syn} = g_{inter} - g_{intra}$ for (B), (D), (F), (H), and (J). Δg_{syn} is fixed at $\Delta g_{syn} = 0.32$ mS/cm² (black arrow in L) with I_{ext}^r varying for (C), (E), (G), (I), and (K). Properties are computed using three modeling strategies as in Figures 3F and 3G, and we use the same notation. The rate equation is calculated analytically in the limit that $\tau_s = 0$ (solid magenta line) and numerically for $\tau_s = 10$ ms (dashed magenta line).

(B and C) The average spike rate (M_i). The values for the vIRt^{ret} and vIRt^{pro} are equal in the uniform state, as the neuronal subpopulations are constantly spiking, and in the symmetric oscillatory state, since the neuronal subpopulations are alternately active. As Δg_{syn} increases, one subpopulation becomes more active than the other, and the less active subpopulation becomes silent at large values of Δg_{syn} . The rate model exhibits a transition from a symmetric oscillatory state to a bistable state at a value of $\Delta g_{syn} = g_{det}$ while the actual transition in the conductance-based model occurs when Δg_{syn} has further increased. The values of g_{tr} and g_{det} are defined in STAR Methods.

(D and E) The average whisking amplitude ($\langle \theta^{amp} \rangle_t$). Analytical results are computed in (G) for the uniform and the bistable state.

(F and G) The whisking frequency $1/T_{vIRt}$.

(H and I) The whisking set point ($\langle \theta^{set} \rangle_t$). Analytical results are computed in (I) for the uniform and the bistable state.

(J and K) The coefficient of variation $\langle CV_2 \rangle_i$ calculated solely from the conductance-based equations.

(L) Phase diagram showing the three dynamical regimes, uniform (left), oscillatory (middle), and bistable (right) computed using the conductance-based model. Values of the coefficient of variation $\langle CV_2 \rangle_i$ calculated for several values of Δg_{syn} and g_{intra} are written.

(M) The coefficient of variation $\langle CV_2 \rangle_i$, calculated as a function of K . The gray ribbon denotes typical experimentally measured values for CV_2 (Figure 1J).

oscillate and becomes bistable (Figures 5B and 5D). Here, vIRt^{ret} neurons are predominantly active while vIRt^{pro} neurons are predominantly quiescent, or vice versa, so that output from the vIRt^{ret} can only shift the set point of the vibrissae. Of biological importance for high-level control of whisking, the period is independent of the strength of the external input, I_{ext}^r (Figure 5G). Thus, as noted above, whisking frequency and amplitude decouple.

The rate formalism does not include variability and thus differences in the calculated output between the conductance-based formalism and the rate model are expected. For $g_{tr} < \Delta g_{syn} < g_{det}$, simulation of the conductance-based model shows that the period is a weakly increasing function of the external input, i.e., a factor of 1.4 over the full range of input current (Figure 5G),

for realistic parameters. For $\Delta g_{syn} > g_{det}$, the bistable output obtained in simulations of the conductance equations occurs for larger values of Δg_{syn} than predicted by the rate equations. The discrepancy is related to the irregular spiking (Figures 4E–4H). While the average activity across the vIRt^{ret} and vIRt^{pro} subpopulations is well predicted from the rate formulation as a function of both Δg_{syn} (Figure 5B) and I_{ext}^r (Figure 5C, with Δg_{syn} just shy of the value of g_{det}), the vIRt^{ret} and vIRt^{pro} neurons do not spike completely in alternation. Thus, for $\Delta g_{syn} > g_{det}$, there is a wide range of values of Δg_{syn} for which one neuronal subpopulation is more active than the other and oscillations remain. The difference in activity between the more and the less active subpopulation increases with Δg_{syn} until only one subpopulation is active and the network is solely bistable. We conclude that oscillations

emerge at an intermediate range of Δg_{syn} , and the bursting frequency decreases with Δg_{syn} in this regime.

Set point increases with Δg_{syn} and varies weakly with I_{ext}

We now turn to the set point of the vibrissae. For the uniform region, the inhibitory output from the vIRt initially counters the excitatory input to the vFMN and the vibrissae are almost fully retracted. The vibrissae gradually protract and, upon the onset of oscillations, the set point reaches the full protracted position concurrent with saturation of the amplitude of whisking (Figure 5H). This set point is maintained until the onset of bistability; depending on the state of the vIRt^{ret} subpopulation, the set point either continues to be maintained or returns to fully a retracted position. The set point is largely unaffected by changes in the external input to the vIRt (Figure 5I). The maximal value of the set point during the oscillatory state is larger than the value when the vIRt^{ret} neurons comprise the active subpopulation in a bistable region, since the adaptation current does not reach its maximal value at the beginning of the active phase within an oscillatory period. All told, the set point is a function of the external input to the vFMN and both non-rhythmic and rhythmic component of output of the vIRt.

Whisking amplitude increases with Δg_{syn} and I_{ext}

The output from the vIRt^{ret} subpopulation is used to drive motoneurons in the vFMN, whose spiking is subject to adaptation. The output from the motoneurons, in turn, serves as input to a model of the musculature in the mystacial pad and thus drives whisking. The whisking amplitude, θ^{amp} (Equation 1), is at or near zero in the uniform region and increases sharply when Δg_{syn} exceeds g_{tr} , for which the output of the vIRt oscillates, until the amplitude reaches a saturation value (Figure 5D). In addition, the whisking amplitude is a monotonically increasing function of I_{ext} , up to saturation, consistent with the increase in activity (Equation 131) with increasing external input (Figure 5E).

g_{intra} is the substrate for variability in spike timing

Variability, as measured by CV_2 (Figure 1I), is outside of the rate formalism we apply. In contrast, numerical simulations of the conductance-based equations yield variable spike rates as a “finite size” effect that originates from the modest number of synaptic inputs to a cell, i.e., the values for the circuit parameters includes $K = 25$ (Figures 4E–4H) as a realistic estimate. This significantly contributes to non-zero-values of CV_2 that extends across all values of Δg_{syn} and external input I_{ext} (Figures 5J and 5K). Sparse connectivity leads to variability since the number of inputs to each neuron from pre-synaptic partners is random and the identities of the pre-synaptic partners are also random (van Vreeswijk and Sompolinsky, 1998; Golomb and Hansel, 2000; Börgers and Kopell, 2003) The circuit produces a state in which one subpopulation spikes more than the other one in a broader range of Δg_{syn} as g_{intra} increases, and thus the variability increases (Figures 5B, 5C, 5L, S2B, and S2C). This leads to a quantitative relationship between range of oscillations and the value of g_{intra} : large values of g_{intra} give rise to larger values of variability. The implication is that variability increases the resilience of the oscillatory output.

Spiking variability during bursts, measured by CV_2 , decreases as K increases while the ratio K/N and the products Kg_{intra} and Kg_{inter} remain unchanged (Figure 5M). This occurs because fluctua-

tations in the input synaptic conductances to a neuron are averaged out. CV_2 does not go to zero for larger K because the interspike intervals during bursts decrease with time due to the adaptation current, even without any fluctuations in the synaptic inputs (Figures S2J and S2K). The measured CV_2 (Figure 1J) is consistent with the value we consider, i.e., $K = 25$ (Figure 5M).

The composite system of pBötC input and vIRt oscillations exhibits two types of whisks

Up to now we separately analyzed the two sources of rhythmic whisking, i.e., feedforward drive by the pBötC and whisking driven by internal vIRt dynamics. Although the coupling from the pBötC to the vIRt is likely to be strong, the composite system is expected to operate in a manner largely predicted from the two mechanisms for rhythmic whisking, i.e., drive from the pBötC and autonomous oscillations, since there is no known feedback from the vIRt to the pBötC (Deschênes et al., 2016b). To further understand the behavior of the composite system, we first simulated the conductance-based equations for the full circuit (Figure 2A). Choosing parameters equal to those of solely the vIRt circuit (Figures 4E–4H), we see that the vIRt^{ret} neurons are silenced by activity in the pBötC, the vIRt^{pro} neurons are excited, and the vFMN neurons are excited (Figures 6A and 6B). This leads to protraction of the vibrissae, with amplitude θ_1^{amp} , in a manner that is nearly synchronous with inhalation (Figures 6B and 6C). The amplitude of this whisk is invariably larger than those of the subsequent intervening whisks, i.e., $\theta_2^{\text{amp}}, \theta_3^{\text{amp}}, \dots$, that are generated by the internal vIRt dynamics (Figure 6C).

Dependence of amplitudes and time differences on synaptic strengths

We performed numerical studies of the composite system to test aspects of the coordination of the pBötC-driven and vIRt-generated dynamics (Figures 6D–6F). First, we observed that the average amplitude of the first whisk increases approximately linearly with increasing values of g^{RB} until saturation is observed (Figure 6D). This dependency resembles that for the circuit with solely feedforward inhibition (Figure 3H). The non-zero value of θ_1^{amp} for $g^{\text{RB}} = 0$ reflects the non-zero average amplitude of the rhythmic whisks that occur from the vIRt circuit dynamics and is similar to the amplitudes of intervening whisks θ_i^{amp} , which are almost independent of g^{RB} for $i \geq 3$ (Figure 6D). In contrast, we observed that the average amplitude of the first whisk is essentially independent of g_{inter} (Figure 6E), consistent with the first whisk affected mainly by the pBötC-induced inhibition of inhibition. In contrast to θ_1^{amp} , the average amplitude of intervening whisks increases with increasing values of g_{inter} until saturation is reached (Figure 6E); this is consistent with the increase in whisking amplitude with increasing values of Δg_{syn} in isolated vIRt circuits (Figure 5D). The amplitude θ_2^{amp} is somewhat larger than θ_3^{amp} , consistent with the experimental observations in head-restrained rats (Figure 1H).

Lastly, we studied the instantaneous timing between whisks. The time $t_{w,i}$ is defined as the time of the maximal whisking angle during the i -th whisk in the breathing cycle. The average value of the difference in time between consecutive whisks, denoted $\langle t_{w,i+1} - t_{w,i} \rangle_t$, is observed to increase with g_{inter} (Figure 6F). This matches expectations for oscillations that are generated

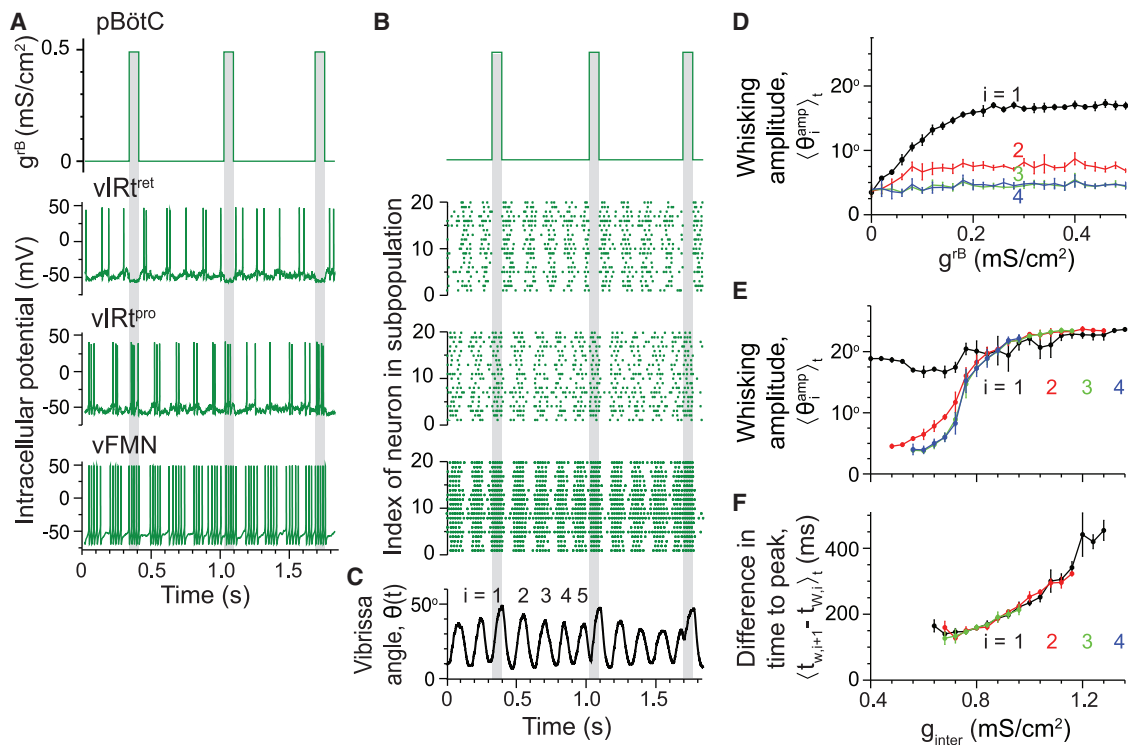


Figure 6. Dynamics of a conductance-based circuit with pBötC input to the vIRt

See Figure 2A for the schematic. We used the same parameters as the simulation without pBötC input (Figures 4E–4H, 5A, 5B, 5D, 5F, 5H, and 5J) plus $g^B = 0.5 \text{ mS/cm}^2$, $T_{pBötC} = 700 \text{ ms}$, $T_{rand} = 150 \text{ ms}$, and $\Delta t_{pBötC} = 70 \text{ ms}$.

(A) Time courses of spiking for an example neuron for the vIRt^{ret}, vIRt^{pro}, and vFMN subpopulations.

(B) Rastergrams across twenty neurons in the simulated subpopulations.

(C) The calculated vibrissa angle $\theta(t)$.

(D) The calculated whisking amplitudes as a function of g^B with $g^{inter} = 0.64 \text{ mS/cm}^2$. The first whisk is driven by the pBötC input and subsequent intervening whisks, with $i = 2-4$, are driven by internal vIRt dynamics. Error bars in (D–F) denote SD.

(E) The calculated whisking amplitude as a function of g^{inter} .

(F) The slowing down of whisking for the intermediate whisks is shown by plotting $\langle t_{w,i+1} - t_{w,i} \rangle_t$ as a function of g^{inter} .

by the vIRt (Figure 5F). The two mechanisms of whisking operate cooperatively. The disinhibition mechanism generates the first, often largest, whisks, and the vIRt mechanism is responsible for the subsequent ones.

Analysis of phase resetting reveals strong pBötC input

In general, output from the pBötC not only drives protraction of the vibrissae through the pBötC \rightarrow vIRt^{ret} \rightarrow vFMN relay (Figures 3A and 3E) but impacts the timing of the vIRt oscillator and results in partial coordination among the two oscillators. A central question is how individual whisking responses depend on the difference between the time of the maximum protraction angle of the previous whisk, designated $t_{w,1}$, and the onset time of pBötC activity, designated t_B (Figure 7A). We quantify the timing of the whisk immediately following the onset time of pBötC activity by the time of its maximum protraction angle, designated $t_{w,2}$. When a protraction is quickly followed by inhalation, the subsequent protraction occurs rapidly (Figure 7B, top line). This result matches experimental observations (Moore et al., 2013) (Figures 1A and 1B), where this rapid succession of protractions is referred to as a “double pump” (Towal and Hartmann, 2008; Deutsch et al., 2012). In contrast, when inhalation starts during protraction, the

peak of the subsequent protraction is delayed, assuming that the vibrissa continues to protract as long as the vIRt^{ret} is silent (Figure 7B, bottom line). The relation between protraction events and inhalation across all data shows that the time between successive whisks, designated $\Delta t_{w,21} = t_{w,2} - t_{w,1}$, varies linearly with the time between the onset of inhalation and the previous protraction, designated $\Delta t_{Bw,1} = t_B - t_{w,1}$. Formally,

$$\Delta t_{w,21} = s_{w,21} \Delta t_{Bw,1} + \Delta t_{w,21}(0) \quad (\text{Equation 4})$$

where the data yield a slope of $s_{w,21} = 0.82$ and an intercept of $\Delta t_{w,21}(0) = 88 \text{ ms}$ (Figure 7C; only cases where breathing frequency is much less than intrinsic vIRt frequency are included in the data analysis). Thus a whisk is either advanced or delayed relative to the normal whisking period depending on the value of $\Delta t_{Bw,1}$.

For the limiting case of an arbitrarily large value of input from the pBötC, the vibrissae asymptote to their maximum angle while the pBötC is active. They reach maximum protraction just as the pBötC stops spiking, i.e., for $\Delta t_{w,2B} = \Delta t_{pBötC}$ where $\Delta t_{w,2B} \equiv t_{w,2} - t_B$ is the time between the onset of inhalation

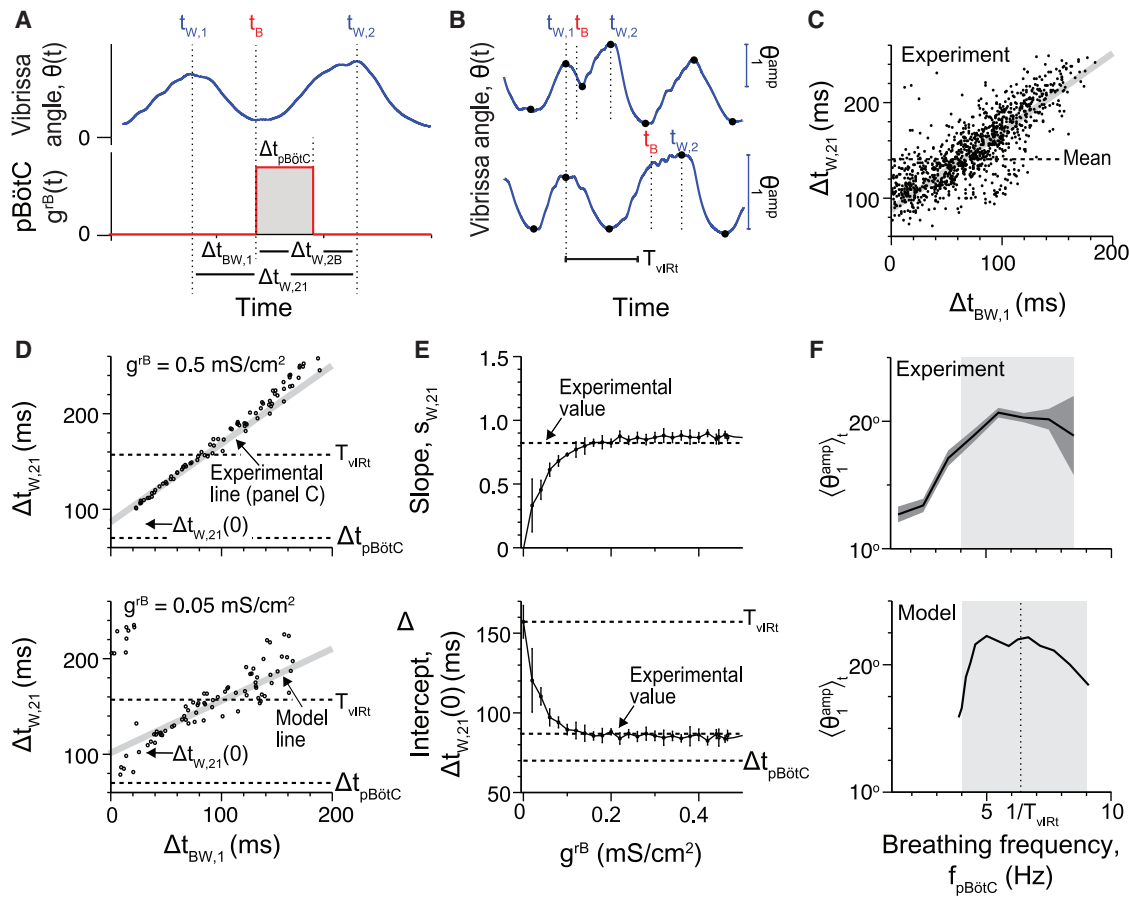


Figure 7. Effects of pBötC activity on the timing and amplitude of the subsequent whisk

(A) Cartoon to define the symbols.

(B) Stimulations of the conductance model to show the vibrissa angle $\theta(t)$ for two aspects of the timing of breathing relative to whisking (Figure 4). The common vertical dotted line, labeled $t_{w,1}$, denotes the peak of a whisk just prior to input from the pBötC. The top trace is an example of input from the pBötC just after the time of the peak and the bottom trace is an example of relatively late input. Model parameters: $g^{rB} = 0.5 \text{ mS/cm}^2$, $T_{\text{pBötC}} = 700 \text{ ms}$, $T_{\text{rand}} = 150 \text{ ms}$ (defined in STAR Methods), $\Delta t_{\text{pBötC}} = 70 \text{ ms}$. Other parameters are as in Figures 4E–4H.

(C) Experimental results from head-restrained rats (Moore et al., 2013) of the total time between protraction, $\Delta t_{w,21}$, as a function of the time of inhalation after the last protraction, $\Delta t_{Bw,1}$. The gray line is the linear fit over the full range. The mean is over all trials.

(D) The calculated total time $\Delta t_{w,21}$ as a function of $\Delta t_{Bw,1}$ for two values of input conductance from the pBötC, i.e., $g^{rB} = 0.5 \text{ mS/cm}^2$ (top) and 0.05 mS/cm^2 (bottom). The gray line is the experimental fit from (C) (top) and the linear fit over the range $40 < \Delta t_{Bw,1} < 140 \text{ ms}$ (bottom). For $g^{rB} = 0.05 \text{ mS/cm}^2$ and small values of $\Delta t_{Bw,1}$, the deduced values of $\Delta t_{w,21}$ may be large since the first increase in the vibrissa angle caused by input from the pBötC may be too small to be detected as a separate new whisk.

(E) The slope $s_{w,21}$ (top) and the intercept $\Delta t_{w,21}(0)$ (bottom) as a function of g^{rB} . Error bars denote SD. The dotted lines denote the experimental values from (C).

(F) The whisking amplitude $\langle \theta_{1}^{amp} \rangle_t$ versus breathing frequency $f_{\text{pBötC}}$. The top panel shows the frequency computed from experimental data from head-restrained rats (Moore et al., 2013). The gray area highlights the range of exploratory sniffing frequencies. The bottom panel shows the frequency calculated as a function of breathing frequency for $T_{\text{rand}} = 10 \text{ ms}$.

and the next protraction, and $\Delta t_{\text{pBötC}}$ is the width of the inhibitory input from the pBötC to vIRt^{ret} neurons. Thus $t_{w,2}$ occurs at $t_B + \Delta t_{\text{pBötC}}$. In this limiting case, $\Delta t_{w,21} = \Delta t_{Bw,1} + \Delta t_{\text{pBötC}}$ so that the slope of the $\Delta t_{w,21}$ versus $\Delta t_{Bw,1}$ line is $s_{w,21} = 1$ and the intercept is $\Delta t_{w,21}(0) = \Delta t_{\text{pBötC}}$ (Equation 4). More realistically, the delay $\Delta t_{w,2B}$ is expected to decrease as $\Delta t_{Bw,1}$ increases in value, since the vibrissae will be part-way to maximal protraction; this reduces the value of the slope.

Simulation of the conductance-based equations indeed show that $\Delta t_{w,21}$ is proportional to $\Delta t_{Bw,1}$ (Figure 7D; see Figure S3 for ex-

ceptions). The slope of the line for $\Delta t_{w,21}$ versus $\Delta t_{Bw,1}$ is greater for larger values of g^{rB} ; it starts from 0 for $g^{rB} = 0$ and increases to a saturation value of $s_{w,21} = 0.87$, which is close to the experimental value (Figures 7C and 7E). The intercept $\Delta t_{w,21}(0)$ is equal to T_{vIRt} for $g^{rB} = 0$ and decreases to a saturation value of $\Delta t_{w,21}(0) = 85 \text{ ms}$; this is approximately the time needed to generate a whisk when the onset of pBötC activity arrives just after the previous maximum protraction. The conclusion from this analysis and its relation to the experimental data (Figure 7C) is that input from the pBötC to the vIRt^{ret} is strong, such that the

pBötC largely resets the state of the vIRt oscillator, with $g^{\text{rb}} > 0.2$ mS/cm².

The input from the pBötC also affects the average amplitude of the following whisk, $\langle \theta_1^{\text{amp}} \rangle_t$. Experimental measurements of $\langle \theta_1^{\text{amp}} \rangle_t$ versus the breathing frequency, $f_{\text{pBötC}}$, reveal that $\langle \theta_1^{\text{amp}} \rangle_t$ reaches a maximal value within the 4–10 Hz range of exploratory whisking (Figure 7F). This dependence is captured by the conductance-based model (Figure 1F) when the input to vIRt^{ret} neurons from the pBötC has a duration of $\Delta t_{\text{pBötC}} \approx 70$ ms; see also Figure S4. This corresponds to a boost in amplitude of protraction by feedforward inhibition from the pBötC that is timed to the inactivation of vIRt^{ret} neurons.

Response to suppressed inhibitory input to vIRt^{ret} neurons is consistent with experimental observations

Recent work (Takatoh et al., 2022) showed that regular whisking in mice is perturbed through the expression of a gephyrin-specific ubiquitin ligase, designated GFE3 (Gross et al., 2016), in vIRt^{ret} neurons. This manipulation suppresses the post-synaptic inhibitory current. The consequences are that no intervening whisks occur, the dominant whisking-breathing ratio is almost always one-to-one, and the whisking amplitude decreased by about a factor of two (Takatoh et al., 2022).

Can we account for the change caused by GFE3 expression in vIRt^{ret} neurons with the current model for whisking (Figure 2A)? Toward this goal, we assume that GFE3 expression decreases the post-synaptic inhibitory conductance for all inputs to each vIRt^{ret} neuron by a common factor of x , where $x \in [0, 1]$ and

$$g^{\text{rb}} \leftarrow xg^{\text{rb}}, \quad g^{\text{rr}} \leftarrow xg^{\text{intra}}, \quad \text{and} \quad g^{\text{rp}} \leftarrow xg^{\text{inter}}, \quad (\text{Equation 5})$$

while all other conductances remain unchanged (Figure 8A). Numerical simulations of the conductance-based (Figure 8B) and the rate (Figure S5A) equations show that as x varies from one to zero, the amplitude of intervening whisks diminishes until intervening whisks disappear below a critical value, that is, $x \approx 0.6$. Mechanistically, the generation of oscillations by mutual inhibition between the vIRt^{ret} and vIRt^{pro} subpopulations of neurons is disrupted since GFE3 diminishes the strength of the vIRt^{pro}-to-vIRt^{ret} but not vIRt^{ret}-to-vIRt^{pro} pathway.

A seeming paradox is that the average time difference between consecutive whisks, i.e., $\langle t_{w(i+1)} - t_{wi} \rangle_t$, increases for $i=1$ and only weakly decreases $i=2$ and 3 as x decreases (Figures 8C and S5B). Further, the amplitude θ_1^{amp} first increases then decreases as x varies from one to zero. The primary reason for these increases is that intervening whisks leave the vibrissae, on average, at a protracted angle when the pBötC inhibition begins (Figure 7B, top), opposed to the more retracted initial angle when intervening whisks are blocked by GFE3. A secondary reason is that intervening whisks lead to greater adaptation of the facial motoneurons in comparison with a state of silent vFMN neurons. As x continues to decrease, θ_1^{amp} eventually is diminished to zero as a consequence of weak disinhibition of vIRt^{ret} neurons. The observed elimination of intervening whisks and a 2-fold decrement in θ_1^{amp} correspond to $x \approx 0.3$. We predict that blocking inhibition among the vIRt^{ret} neurons will decrease spiking irregularity (Figure 8D).

DISCUSSION

We delimited and evaluated two mechanisms and their interplay that drive rhythmic spiking in neurons of the vibrissa oscillator, the vIRt, in the medulla. The vIRt is comprised predominantly of inhibitory neurons. Our model (Figures 2A and 2E) explains published (Moore et al., 2013; Towal and Hartmann, 2006; Ranade et al., 2013; Berg and Kleinfeld, 2003; Takatoh et al., 2022) and new (Figures 1D and 1F–1H) behavioral data on whisking in terms of the underlying anatomy and physiology (Moore et al., 2013; Deschênes et al., 2016b; Takatoh et al., 2013), including newly reanalyzed variability (Figure 1J). The first mechanism is feedforward control by strong inhibitory input from the pBötC inhalation oscillator to one subpopulation of neurons in the vIRt (Figure 3). This input results in disinhibition of the neurons in the facial nucleus that control the intrinsic muscles and leads to protraction of the vibrissae. The second mechanism is autonomous generation of rhythmic spiking activity across two subpopulations of neurons in the vIRt (Figures 4 and 5). More than the classic half-center oscillator scheme, in which reciprocal inhibition between two neurons (Brown, 1911) plus a mechanism for cellular or synaptic adaptation (Marder and Calabrese, 1996; Satterlie, 1985; Isett et al., 2018) leads to oscillations; here, the autonomous generation of oscillations requires two subpopulations of neurons (Figures 2A and 2E). The connections within each subpopulation lead to variability in neuronal spike times (Figures 4E–4H). This in turn increased the dynamic range of the rhythmic output and makes the rhythm robust against changes in network parameters, such as the specific value of synaptic conductances (Figures 5F, 5L, and 5M).

The interaction of the two mechanisms for spiking by neurons in the vIRt is observed when the breathing rate is slow (Figures 1C–1H). The first whisk in a breathing cycle is driven by output from the pBötC and has the greatest amplitude (Figure 1E). The subsequent whisks are driven exclusively by the vIRt. The ratio of the interval between breaths to the interval between whisks is non-integer (Moore et al., 2013; Deschênes et al., 2016b). This is consistent with the relatively fixed period of the vIRt oscillator (Figures 4D, 4H, and 5G) and the apparent lack of feedback from whisking, either corollary discharge from the vIRt or reafferent whisking input from the trigeminal to the breathing complex (Moore et al., 2015). Further, resetting the state of vIRt neurons by strong input from pBötC leads to non-monotonic protractions, such events may appear as “double pumps” in vibrissa touch (Towal and Hartmann, 2006; Deutsch et al., 2012) (Figures 6C and 7B). As a general issue, the drive of vibrissa movement by incommensurate rhythmic signals from breathing and vIRt oscillators results in a pattern of partial correlation between breathing and whisking, in line with the ideas of von Holst for the interactions of rhythmic motor actions across both active sensing as well as locomotion (von Holst, 1939, 1973).

Beyond the classic half-center oscillator, past work with all-inhibitory networks focused on three architectures. The first architecture is small loops of neurons with an odd number of cells in the loop (Kling and Szekely, 1968; Ádám and Kling, 1971), analogous to a ring oscillator in electronics. A pulse of spikes will propagate around the network. This circuit provides the

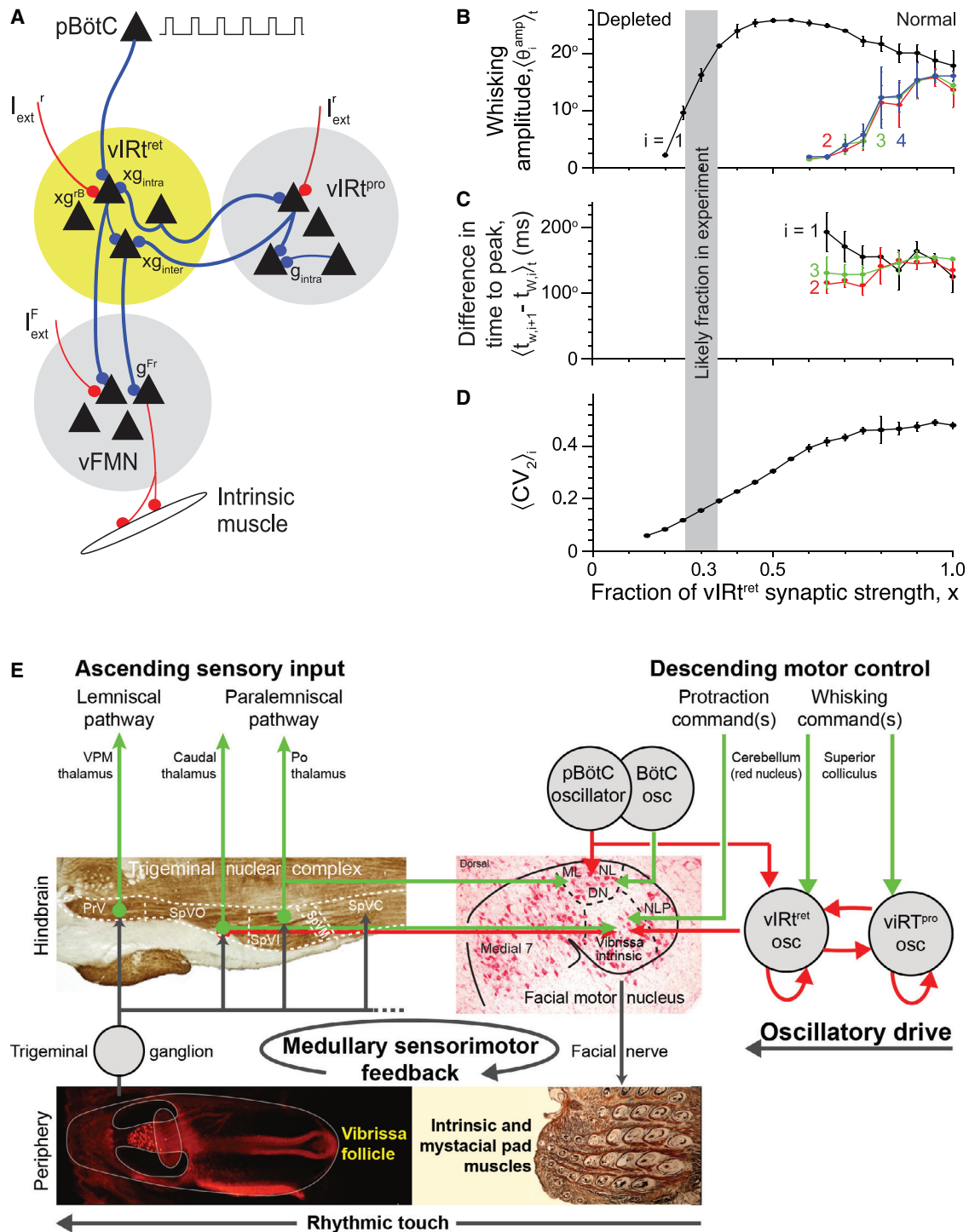


Figure 8. Analysis of perturbations to vIRt^{ret} synapses and summary of brainstem control of whisking

(A) Diagram for dynamics of the vibrissa oscillator with the vIRt^{ret} under partial gephyrin degradation to weaken all GABAergic inhibitory inputs to vIRt^{ret} neurons (yellow circle). We simulate the conductance-based model and assume that all synapses in the vIRt^{ret} are equally weakened by a factor of x . A. We chose $g_{intra} = 0.48$ mS/cm², $g_{inter} = 0.8$ mS/cm², $g_{Fr} = 0.5$ mS/cm², $g_{adapt} = 7$ mS/cm², $I_{ext}^r = 20$ μ A/cm², $I_{ext}^F = 3.1$ μ A/cm², $K = 25$, and $N = 100$ for our simulations.

(B) The amplitude of the four consecutive whisks after the onset of pBötC activity, denoted by $i = 1, 2, 3, 4$, as a function of x (Equation 5). Error bars denote SD. The yellow band in (B–D) indicates the fraction estimated from the data in Takatch et al. (2022).

(C) The times between average successive whisks ($\langle t_{w,i+1} - t_{w,i} \rangle_t$) as a function of x .

(legend continued on next page)

basic motif for the generation of the swim rhythm in the leech (Stent et al., 1978). The second architecture is populations of inhibitory neurons without spatial structure to their connectivity. Such homogeneous networks, for the case of all-to-all coupling, may show synchronous spiking. This circuit provides the basic motif for the generation of fast gamma rhythms in mammalian cortex (Whittington et al., 1995), although the circuit in neocortex may incorporate other cell types (Börger et al., 2005). All-inhibitory networks can produce seemingly complex spiking behavior as well. One instantiation is that groups of neurons that tend to spike together coalesce in clusters that spike alternately over time (Golomb and Rinzel, 1994). A second instantiation is networks in which all of the neurons spike asynchronously (Golomb and Hansel, 2000; Neltner et al., 2000). The third architecture of relevance to the present work makes use of two subpopulations of neurons, each with an adaptation current, to generate alternating burst of spikes. This architecture has been used to model rhythmic spiking by spinal cord circuits involved in locomotion (Ausborn et al., 2018). Guided by the observation (Moore et al., 2013; Deschênes et al., 2016b; Takatoh et al., 2022) of two subpopulations of neurons in the vIRt, we incorporated and advanced such an architecture by incorporating two strengths of inhibition (Figure 2A).

We model the vIRt using conductance-based equations and map the all-inhibitory network onto rate equations (Shriki et al., 2003; Golomb et al., 2006a; Hayut et al., 2011). Each neuronal population is represented by two variables: a fast synaptic variable and a slow adaptation variable. To map the conductance-based equations onto rate equations, we estimate the difference between the average neuronal membrane potential and the reversal potential of the synapses. Therefore, such rate equations are a good approximation for excitatory systems, where the average membrane potential lies far from the synaptic reversal potential for glutamergic synapses. In inhibitory networks, the average membrane potential lies close to the reversal potential for GABAergic synapses. Nonetheless, we find that the average difference between the neuronal membrane potential and the synaptic reversal potential can be accurately calculated and the reduction of conductance-based to rate-based equations holds (Figure 5).

Five general lessons about neuronal dynamics from our two-population circuit (Figure 2) follow from the analysis of the rate model. The dynamic properties of the network is shown to have three regions of output as a function of the difference between the strengths of inter- and intra-population synaptic conductances, Δg_{syn} (Equations 10, 11, and 12) (Figures 5B, 5F, and 5L). Only the central region leads to rhythmic bursts of spikes across the two subpopulations (Figure 5). Interestingly, the oscillatory region of this model is similar to that used to understand the perceptual issue of binocular rivalry within in cortical circuits (Wilson, 2003; Shpiro et al., 2007; Soloduchin and Shamir, 2018). A decision in the context of rivalry can be presented by a transition from the oscillatory to the bistable state.

A second general second lesson is that the frequency of whisking and the amplitude of a whisk are decoupled. Within the region for vIRt-driven whisking, the frequency of oscillations is directly tied to the timescale of the adaptation current (Equations 116 and 124). In contrast, the whisking frequency is independent of the external input, which gates the oscillations, as well as controls the amplitude of whisking for both pBötC-drive (Equations 62 and 63) and intrinsic-driven whisking (Equation 124). The third lesson is that the range of the region for vIRt-driven whisking, controlled by the value of Δg_{syn} , is proportional to the strength of the adaptation current.

A fourth general lesson is that the extent of synaptic connectivity within each subpopulation of inhibitory neurons balances the trade-off between variability in spike rate and the range of conductances that support whisking. The variability is a so-called “finite size” effect (Figure 5M). Unfortunately, we cannot determine an analytical expression for the variability with the current methods. Nonetheless, numerical simulations show that the variability leads to an increase in dynamic range of the oscillatory region (Figures 5F, 5L, and S2F).

A final general lesson from our model follows from the absence of feedback from the vIRt^{ret} or vIRt^{pro} neurons to the pBötC. The direct modulation of vIRt^{ret} output from the pBötC is strong and leads to a resetting of the rhythm. Thus the absence of feedback implies that the rhythmic dynamics of the vibrissae can be largely predicted as the combination of drive to the vIRt^{ret} neurons by the pBötC and autonomous oscillations generated within the vIRt. The need for orofacial motor actions to protect the patency of the airway suggests that unidirectional drive from the pBötC may be a general medullary design rule.

What is the consequence of the choice of a threshold-linear f - I curve (Figure 2C; Equation 32) as opposed to a saturating f - I curve? For our choice, the whisking frequency is independent of I'_{ext} (Figure 5G; Equation 124). In contrast, the use of a saturating gain function (Shpiro et al., 2007) causes the oscillation frequency first to decrease and then increase with the external input to the two populations; there is also a possibility of a stationary regime between the two oscillatory states. This dependency of the oscillation frequency on the external input occurs because the active population almost reaches saturation, whereas with a linear gain function the neurons will spike far from their saturation rate.

The whisking oscillator circuit is a major component of a larger circuit for active sensing with vibrissae. The rhythmicity of inspiration, via the pBötC, and the vIRt, define the period and shape of the unperturbed waveform for a whisk through drive to the intrinsic muscles for each vibrissa. Further, the pBötC and the Böttinger complex (BötC) activate protraction and retraction extrinsic muscles in the mystacial pad, which shift the pivot point for the vibrissae (Hill et al., 2008; Moore et al., 2013). Beyond these internal signals, vibrissa touch leads to rapid feedback that modifies the shape of the whisking waveform (Nguyen and Kleinfeld, 2005; Bellavance et al., 2017). Feedback is mediated

(D) Dependence of (CV_2) of vIRt^{ret} neurons on the value of x .

(E) Summary of the circuitry that underlies the vibrissa motor plant. The vIRt drives rhythmic motion, and the shape of the waveform is set by the motor plant and feedback pathway that change the input to intrinsic and extrinsic motoneurons, and thus contact forces, upon touch. Figures updated from published summary (Bellavance et al., 2017; Kleinfeld and Deschênes, 2011).

by both excitatory and inhibitory projections from spinal trigeminal nuclei to the extrinsic muscles (Figure 8E); in this manner the spinal trigeminal nuclei act as premotor nuclei. Rapid feedback can lead to a transient decrease in contact force, such that the contact force per whisk has a double peak. This modulation is posited to play a role in texture discrimination by slip-stick friction (Ritt et al., 2008; Lottem and Azouz, 2009; Schwarz, 2016; Isett et al., 2018). Rapid feedback also minimizes the contact time (Bellavance et al., 2017). Finally, feedback also occurs on the timescale of multiple whisks through a shift in the set point of whisking (Towal and Hartmann, 2006; Mitchinson et al., 2007) and, in principle, could involve high-order input to the vRt^{ret} .

STAR★METHODS

Detailed methods are provided in the online version of this paper and include the following:

- KEY RESOURCES TABLE
- RESOURCE AVAILABILITY
 - Lead contact
 - Materials availability
 - Data and code availability
- EXPERIMENTAL MODEL AND SUBJECT DETAILS
- METHOD DETAILS
 - Summary of the rate model
 - Glossary
 - Conductance-based (CB) network model: architecture
 - CB network model: sizes and connectivity
 - CB network model: dynamics of single vFMN neurons
 - CB network model: dynamics of single vRt neurons
 - CB network model: inhibitory synaptic currents
 - CB network model: vibrissa movement
 - Schema for a rate model
 - Reduction of a CB model to a rate model
 - Rate model for vibrissa movement
 - Analytical solution of the rate model for the pBötC-vRt^{ret}-vFMN circuit
 - Analytical calculation of the vibrissa set-point angle at rest and at saturation for the pBötC-vRt^{ret}-vFMN circuit
 - Analytical solution of the rate model for the vRt^{ret}-vRt^{pro} circuit
 - The oscillation period T_{vRt} increases monotonically with J_{inter}
 - Numerical methods details
 - Experimental methodological details for rats
- QUANTIFICATION AND STATISTICAL ANALYSIS
 - Vibrissa tracking
 - Population- and time-averaged quantities
 - Extracting whisking amplitudes

SUPPLEMENTAL INFORMATION

Supplemental information can be found online at <https://doi.org/10.1016/j.neuron.2022.08.020>.

ACKNOWLEDGMENTS

We thank Martin Deschênes for discussions and Lawrence Abbott for comments on an early version of the manuscript. This work was supported by NIH grant U19 NS107466 and National Science Foundation grant PHY-1748958. Conversations that led to this work occurred at the Kavli Institute for Theoretical Physics program “Recording, analyzing, manipulating, and modeling whole brain activity,” funded by NIH grant R25 GM067110 and Gordon and Betty Moore Foundation grant 2919.02.

AUTHOR CONTRIBUTIONS

D.G., D.K., V.P., J.T., and F.W. planned the project. D.G. performed all calculations and wrote all code. A.F. acquired new data. D.G., D.K., J.D.M., A.F., and V.P. analyzed data. D.G. and D.K. prepared figures and wrote the manuscript with contributions from all authors.

DECLARATION OF INTERESTS

The authors declare no competing interests.

Received: January 21, 2022

Revised: July 6, 2022

Accepted: August 17, 2022

Published: September 15, 2022

REFERENCES

- Ádám, A., and Kling, U. (1971). On the behaviour of some cyclically symmetric networks. *Acta Cybernet.* 7, 69–79.
- Argaman, T., and Golomb, D. (2018). Does layer 4 in the barrel cortex function as a balanced circuit when responding to whisker movements? *Neuroscience* 368, 29–45. <https://doi.org/10.1016/j.neuroscience.2017.07.054>. <http://www.ncbi.nlm.nih.gov/pubmed/28774782>.
- Ausborn, J., Snyder, A.C., Shevtsova, N.A., Rybak, I.A., and Rubin, J.E. (2018). State-dependent rhythmogenesis and frequency control in a half-center locomotor cpg. *J. Neurophysiol.* 119, 96–117. <https://doi.org/10.1152/jn.00550.2017>. <http://www.ncbi.nlm.nih.gov/pubmed/28978767>.
- Bellavance, M.A., Takato, J., Lu, J., Demers, M., Kleinfeld, D., Wang, F., and Deschênes, M. (2017). Parallel inhibitory and excitatory trigemino-facial feedback circuitry for reflexive vibrissa movement. *Neuron* 95, 673–682.e4.
- Berg, R.W., and Kleinfeld, D. (2003). Rhythmic whisking by rat: retraction as well as protraction of the vibrissae is under active muscular control. *J. Neurophysiol.* 89, 104–117. <https://doi.org/10.1152/jn.00600.2002>. http://www.ncbi.nlm.nih.gov/entrez/query.fcgi?cmd=Retrieve&db=PubMed&dopt=Citation&list_uids=12522163.
- Börgers, C., Epstein, S., and Kopell, N.J. (2005). Background gamma rhythmicity and attention in cortical local circuits: a computational study. *Proc. Natl. Acad. Sci. USA* 102, 7002–7007. <https://doi.org/10.1073/pnas.0502366102>. <https://www.ncbi.nlm.nih.gov/pubmed/15870189>.
- Börgers, C., and Kopell, N. (2003). Synchronization in networks of excitatory and inhibitory neurons with sparse, random connectivity. *Neural Comput.* 15, 509–538. <https://doi.org/10.1162/089976603321192059>. <http://www.ncbi.nlm.nih.gov/pubmed/12620157>.
- Brown, T.G. (1911). The intrinsic factors in the act of progression in the mammal. *Proc. R. Soc. Lond. B* 88, 308–319.
- Carvell, G.E., and Simons, D.J. (1990). Biometric analyses of vibrissal tactile discrimination in the rat. *J. Neurosci.* 10, 2638–2648.
- Chow, C.C., and Kopell, N. (2000). Dynamics of spiking neurons with electrical coupling. *Neural Comput.* 12, 1643–1678. http://www.ncbi.nlm.nih.gov/entrez/query.fcgi?cmd=Retrieve&db=PubMed&dopt=Citation&list_uids=10935921.
- Clack, N.G., O’Connor, D.H., Huber, D., Petreanu, L., Hires, A., Peron, S., Svoboda, K., and Myers, E.W. (2012). Automated tracking of whiskers in videos

- of head fixed rodents. *PLoS Comp. Biol.* 8, e1002591. <https://doi.org/10.1371/journal.pcbi.1002591>. <http://www.ncbi.nlm.nih.gov/pubmed/22792058>.
- Cramer, N.P., and Keller, A. (2006). Cortical control of a whisking central pattern generator. *J. Neurophysiol.* 96, 209–217. <https://doi.org/10.1152/jn.00071.2006>. http://www.ncbi.nlm.nih.gov/entrez/query.fcgi?cmd=Retrieve&db=PubMed&dopt=Citation&list_uids=16641387.
- Deschênes, M., Kurnikova, A., Elbaz, M., and Kleinfeld, D. (2016a). Circuits in the ventral medulla that phase-lock motoneurons for coordinated sniffing and whisking. *Neural Plast.* 2016, 7493048.
- Deschênes, M., Moore, J., and Kleinfeld, D. (2012). Sniffing and whisking in rodents. *Curr. Opin. Neurobiol.* 22, 243–250. <https://doi.org/10.1016/j.conb.2011.11.013>. <https://www.ncbi.nlm.nih.gov/pubmed/22177596>.
- Deschênes, M., Takatoh, J., Kurnikova, A., Moore, J.D., Demers, M., Elbaz, M., Furuta, T., Wang, F., and Kleinfeld, D. (2016b). Inhibition, not excitation, drives rhythmic whisking. *Neuron* 90, 374–387. <https://doi.org/10.1016/j.neuron.2016.03.007>. <http://www.ncbi.nlm.nih.gov/pubmed/27041498>.
- Deutsch, D., Pietr, M., Knutsen, P.M., Ahissar, E., and Schneidman, E. (2012). Fast feedback in active sensing: touch-induced changes to whisker-object interaction. *PLoS One* 7, e44272.
- Ermentrout, B. (1994). Reduction of conductance-based models with slow synapses to neural nets. *Neural Comput.* 6, 679–695.
- Ermentrout, B. (1998). Neural networks as spatio-temporal pattern-forming systems. *Reports on Progress in Physics* 61, 353.
- Golomb, D. (2007). Neuronal synchrony measures. *Scholarpedia* 2, 1347.
- Golomb, D. (2014). Mechanism and function of mixed-mode oscillations in vibrissa motoneurons. *PLoS One* 9, e109205. <https://doi.org/10.1371/journal.pone.0109205>. <http://www.ncbi.nlm.nih.gov/pubmed/25275462>.
- Golomb, D., Ahissar, E., and Kleinfeld, D. (2006a). Coding of stimulus frequency by latency in thalamic networks through the interplay of GABAB-mediated feedback and stimulus shape. *J. Neurophysiol.* 95, 1735–1750. http://www.ncbi.nlm.nih.gov/entrez/query.fcgi?cmd=Retrieve&db=PubMed&dopt=Citation&list_uids=16267113.
- Golomb, D., and Hansel, D. (2000). The number of synaptic inputs and the synchrony of large, sparse neuronal networks. *Neural Comput.* 12, 1095–1139. http://www.ncbi.nlm.nih.gov/entrez/query.fcgi?cmd=Retrieve&db=PubMed&dopt=Citation&list_uids=10905810.
- Golomb, D., Hansel, D., and Mato, G. (2001). Mechanisms of synchrony of neural activity in large networks. In *Neuro-Informatica and Neural Modelling. Handbook of Biological Physics*, 4, F. Moss and S. Gielen, eds. (Elsevier Science), pp. 887–968.
- Golomb, D., and Rinzel, J. (1993). Dynamics of globally coupled inhibitory neurons with heterogeneity. *Phys. Rev. E Stat. Phys. Plasmas Fluids Relat. Interdiscip. Topics* 48, 4810–4814. http://www.ncbi.nlm.nih.gov/entrez/query.fcgi?cmd=Retrieve&db=PubMed&dopt=Citation&list_uids=9961165.
- Golomb, D., and Rinzel, J. (1994). Clustering in globally coupled inhibitory neurons. *Phys. D* 72, 259–282.
- Golomb, D., Wang, X.J., and Rinzel, J. (1994). Synchronization properties of spindle oscillations in a thalamic reticular nucleus model. *J. Neurophysiol.* 72, 1109–1126. http://www.ncbi.nlm.nih.gov/entrez/query.fcgi?cmd=Retrieve&db=PubMed&dopt=Citation&list_uids=7807198.
- Golomb, D., Yue, C., and Yaari, Y. (2006). Contribution of Persistent Na⁺ Current and M-Type K⁺ Current to Somatic Bursting in CA1 Pyramidal Cells: Combined Experimental and Modeling Study. *Journal of Neurophysiology* 96. <https://doi.org/10.1152/jn.00205.2006>.
- Gross, G.G., Straub, C., Perez-Sanchez, J., Dempsey, W.P., Junge, J.A., Roberts, R.W., Trinh, I. A., Fraser, S.E., De Koninck, Y., De Koninck, P., et al. (2016). An e3-ligase-based method for ablating inhibitory synapses. *Nat. Methods* 13, 673–678. <https://doi.org/10.1038/nmeth.3894>.
- Guest, J.M., Seetharama, M.M., Wendel, E.S., Strick, P.L., and Oberlaender, M. (2018). 3d reconstruction and standardization of the rat facial nucleus for precise mapping of vibrissal motor networks. *Neuroscience* 368, 171–186.
- Gutnisky, D.A., Yu, J., Hires, S.A., To, M.S., Bale, M.R., Svoboda, K., and Golomb, D. (2017). Mechanisms underlying a thalamocortical transformation during active tactile sensation. *PLoS Comput. Biol.* 13, e1005576. <https://doi.org/10.1371/journal.pcbi.1005576>. <https://www.ncbi.nlm.nih.gov/pubmed/28591219>.
- Hansel, D., and Sompolinsky, H. (1998). Modeling feature selectivity in local cortical circuits. In *Methods in Neuronal Modeling: From Ions to Networks*, C. Koch and I. Segev, eds. (MIT Press), pp. 499–567.
- Harish, O., and Golomb, D. (2010). Control of the firing patterns of vibrissa motoneurons by modulatory and phasic synaptic inputs: a modeling study. *J. Neurophysiol.* 103, 2684–2699. <https://doi.org/10.1152/jn.01016.2009>. <http://www.ncbi.nlm.nih.gov/pubmed/20200122>.
- Hattox, A.M., Priest, C.A., and Keller, A. (2002). Functional circuitry involved in the regulation of whisker movements. *J. Comp. Neurol.* 442, 266–276.
- Hayut, I., Fanselow, E.E., Connors, B.W., and Golomb, D. (2011). LTS and FS inhibitory interneurons, short-term synaptic plasticity, and cortical circuit dynamics. *PLoS Comput. Biol.* 7, e1002248.
- Hill, D.N., Bermejo, R., Zeigler, H.P., and Kleinfeld, D. (2008). Biomechanics of the vibrissa motor plant in rat: rhythmic whisking consists of triphasic neuromuscular activity. *J. Neurosci.* 28, 3438–3455.
- Hill, D.N., Curtis, J.C., Moore, J.D., and Kleinfeld, D. (2011). Primary motor cortex reports efferent control of vibrissa motion on multiple timescales. *Neuron* 72, 344–356. <https://doi.org/10.1016/j.neuron.2011.09.020>. <http://www.ncbi.nlm.nih.gov/pubmed/22017992>.
- Holt, G.R., Softky, W.R., Koch, C., and Douglas, R.J. (1996). Comparison of discharge variability in vitro and in vivo in cat visual cortex neurons. *J. Neurophysiol.* 75, 1806–1814. <https://doi.org/10.1152/jn.1996.75.5.1806>. <https://www.ncbi.nlm.nih.gov/pubmed/8734581>.
- Isett, B.R., Feasel, S.H., Lane, M.A., and Feldman, D.E. (2018). Slip-based coding of local shape and texture in mouse s1. *Neuron* 97, 418–433.e5. <https://doi.org/10.1016/j.neuron.2017.12.021>. <https://www.ncbi.nlm.nih.gov/pubmed/29307709>.
- Kaneshige, M., Shibata, K.I., Matsubayashi, J., Mitani, A., and Furuta, T. (2018). A descending circuit derived from the superior colliculus modulates vibrissal movements. *Front. Neural Circuits* 12, 100. <https://doi.org/10.3389/fncir.2018.00100>. <https://www.ncbi.nlm.nih.gov/pubmed/30524249>.
- Kaplan, H.S., Salazar Thula, O.S., Khoss, N., and Zimmer, M. (2020). Nested neuronal dynamics orchestrate a behavioral hierarchy across timescales. *Neuron* 105, 562–576.e9.
- Kleinfeld, D., and Deschênes, M. (2011). Neuronal basis for object location in the vibrissa scanning sensorimotor system. *Neuron* 72, 455–468. <http://www.ncbi.nlm.nih.gov/pmc/articles/PMC3971931/pdf/nihms-334967.pdf>.
- Kleinfeld, D., Deschênes, M., Wang, F., and Moore, J.D. (2014a). More than a rhythm of life: breathing as a binder of orofacial sensation. *Nat. Neurosci.* 15, 647–651.
- Kleinfeld, D., Moore, J.D., Wang, F., and Deschênes, M. (2014b). The brainstem oscillator for whisking and the case for breathing as the master clock for orofacial motor actions. *Cold Spring Harb. Symp. Quant. Biol.* 79, 29–39.
- Kling, U., and Szekely, G. (1968). Simulations of rhythmic activities. i. functions of networks with cyclic inhibitions. *Kybernetik* 5, 89–103.
- Kurnikova, A., Moore, J.D., Liao, S.M., Deschênes, M., and Kleinfeld, D. (2017). Coordination of orofacial motor actions into exploratory behavior by rat. *Curr. Biol.* 27, 688–696.
- Lottem, E., and Azouz, R. (2009). Mechanisms of tactile information transmission through whisker vibrations. *J. Neurosci.* 29, 11686–11697. <https://doi.org/10.1523/JNEUROSCI.0705-09.2009>. <http://www.ncbi.nlm.nih.gov/pubmed/19759315>.
- Lund, J.P., Kolta, A., Westberg, K.G., and Scott, G. (1998). Brainstem mechanisms underlying feeding behaviors. *Curr. Opin. Neurobiol.* 8, 718–724.
- Magarinos-Ascoñe, C., Núñez, A., and Delgado-García, J.M. (1999). Different discharge properties of rat facial nucleus motoneurons. *Neuroscience* 94, 879–886. [https://doi.org/10.1016/s0306-4522\(99\)00335-8](https://doi.org/10.1016/s0306-4522(99)00335-8). http://www.ncbi.nlm.nih.gov/entrez/query.fcgi?cmd=Retrieve&db=PubMed&dopt=Citation&list_uids=10579578.

- Marder, E., and Calabrese, R.L. (1996). Principles of rhythmic motor pattern generation. *Physiol. Rev.* **76**, 687–717.
- Mathis, A., Mamidanna, P., Cury, K.M., Abe, T., Murthy, V.N., Mathis, M.W., and Bethge, M. (2018). Deeplabcut: markerless pose estimation of user-defined body parts with deep learning. *Nat. Neurosci.* **21**, 1281–1289. <https://doi.org/10.1038/s41593-018-0209-y>. <https://www.ncbi.nlm.nih.gov/pubmed/30127430>.
- McAfee, S.S., Ogg, M.C., Ross, J.M., Liu, Y., Fletcher, M.L., and Heck, D.H. (2016). Minimally invasive highly precise monitoring of respiratory rhythm in the mouse using an epithelial temperature probe. *J. Neurosci. Methods* **263**, 89–94. <https://doi.org/10.1016/j.jneumeth.2016.02.007>. <https://www.ncbi.nlm.nih.gov/pubmed/26868731>.
- McElvain, L.E., Friedman, B., Karten, H.J., Svoboda, K., Wang, F., Deschênes, M., and Kleinfeld, D. (2018). Circuits in the rodent brainstem that control whisking in concert with other orofacial motor actions. *Neuroscience* **368**, 152–170. <https://doi.org/10.1016/j.neuroscience.2017.08.034>. <http://www.ncbi.nlm.nih.gov/pubmed/28843993>.
- Merel, J., Matthew Botvinick, M., and Wayne, G. (2019). Hierarchical motor control in mammals and machines. *Nat. Commun.* **10**, 5489.
- Meunier, C., and Borejsza, K. (2005). How membrane properties shape the discharge of motoneurons: a detailed analytical study. *Neural Comput.* **17**, 2383–2420. <https://doi.org/10.1162/0899766054796923>. http://www.ncbi.nlm.nih.gov/entrez/query.fcgi?cmd=Retrieve&db=PubMed&dopt=Citation&list_uids=16156933.
- Mitchinson, B., Martin, C.J., Grant, R.A., and Prescott, T.J. (2007). Feedback control in active sensing: rat exploratory whisking is modulated by environmental contact. *Proc. Biol. Sci.* **274**, 1035–1041.
- Moore, J.D., Deschênes, M., Furuta, T., Huber, D., Smear, M.C., Demers, M., and Kleinfeld, D. (2013). Hierarchy of orofacial rhythms revealed through whisking and breathing. *Nature* **497**, 205–210. <https://doi.org/10.1038/nature12076>. <http://www.ncbi.nlm.nih.gov/pubmed/23624373>.
- Moore, J.D., Deschênes, M., Kurnikova, A., and Kleinfeld, D. (2014a). Activation and measurement of free whisking in the lightly anesthetized rodent. *Nat. Protoc.* **9**, 1792–1802.
- Moore, J.D., Kleinfeld, D., and Wang, F. (2014b). How the brainstem controls orofacial behaviors comprised of rhythmic actions. *Trends Neurosci.* **37**, 370–380. <https://doi.org/10.1016/j.tins.2014.05.001>. <https://www.ncbi.nlm.nih.gov/pubmed/24890196>.
- Moore, J.D., Mercer Lindsay, N., Deschênes, M., and Kleinfeld, D. (2015). Vibrissa self-motion and touch are reliably encoded along the same somatosensory pathway from brainstem through thalamus. *PLoS Biol.* **13**, e1002253.
- Mussa-Ivaldi, F.A., and Bizzi, E. (2000). Motor learning through the combination of primitives. *Philos. Trans. R. Soc. Lond. B Biol. Sci.* **355**, 1755–1769. <https://doi.org/10.1098/rstb.2000.0733>. <https://www.ncbi.nlm.nih.gov/pubmed/11205339>.
- Neltner, L., Hansel, D., Mato, G., and Meunier, C. (2000). Synchrony in heterogeneous networks of spiking neurons. *Neural Comput.* **12**, 1607–1641. http://www.ncbi.nlm.nih.gov/entrez/query.fcgi?cmd=Retrieve&db=PubMed&dopt=Citation&list_uids=10935920.
- Nguyen, Q.T., and Kleinfeld, D. (2005). Positive feedback in a brainstem tactile sensorimotor loop. *Neuron* **45**, 447–457.
- Nguyen, Q.T., Wessel, R., and Kleinfeld, D. (2004). Developmental regulation of active and passive membrane properties in rat vibrissa motoneurons. *J. Physiol.* **556**, 203–219.
- Pehlevan, C., and Sompolinsky, H. (2014). Selectivity and sparseness in randomly connected balanced networks. *PLoS One* **9**, e89992. <https://doi.org/10.1371/journal.pone.0089992>.
- Ranade, S., Hangya, B., and Kepecs, A. (2013). Multiple modes of phase locking between sniffing and whisking during active exploration. *J. Neurosci.* **33**, 8250–8256.
- Renart, A., de la Rocha, J., Bartho, P., Hollender, L., Parga, N., Reyes, A., and Harris, K.D. (2010). The asynchronous state in cortical circuits. *Science* **327**, 587–590. <https://doi.org/10.1126/science.1179850>. <http://www.ncbi.nlm.nih.gov/pubmed/20110507>.
- Ritt, J.T., Andermann, M.L., and Moore, C.I. (2008). Embodied information processing: vibrissa mechanics and texture features shape micromotions in actively sensing rats. *Neuron* **57**, 599–613. <https://doi.org/10.1016/j.neuron.2007.12.024>. <http://www.ncbi.nlm.nih.gov/pubmed/18304488>.
- Rosenbaum, R., Smith, M.A., Kohn, A., Rubin, J.E., and Doiron, B. (2017). The spatial structure of correlated neuronal variability. *Nat. Neurosci.* **20**, 107–114.
- Ruder, L., and Arber, S. (2019). Brainstem circuits controlling action diversification. *Annu. Rev. Neurosci.* **42**, 485–504. <https://www.ncbi.nlm.nih.gov/pubmed/31283898>. <https://doi.org/10.1146/annurev-neuro-070918-050201>.
- Satterlie, R.A. (1985). Reciprocal inhibition and postinhibitory rebound produce reverberation in a locomotor pattern generator. *Science* **229**, 402–404.
- Schwarz, C. (2016). The slip hypothesis: tactile perception and its neuronal bases. *Trends Neurosci.* **39**, 449–462. <https://doi.org/10.1016/j.tins.2016.04.008>. <https://www.ncbi.nlm.nih.gov/pubmed/27311927>.
- Seung, H.S., Lee, D.D., Reis, B.Y., and Tank, D.W. (2000). The autapse: a simple illustration of short-term analog memory storage by tuned synaptic feedback. *J. Comput. Neurosci.* **9**, 171–185. http://www.ncbi.nlm.nih.gov/entrez/query.fcgi?cmd=Retrieve&db=PubMed&dopt=Citation&list_uids=11030520.
- Shapiro, A., Curtu, R., Rinzel, J., and Rubin, N. (2007). Dynamical characteristics common to neuronal competition models. *J. Neurophysiol.* **97**, 462–473. <https://doi.org/10.1152/jn.00604.2006>. <http://www.ncbi.nlm.nih.gov/pubmed/17065254>.
- Shriki, O., Hansel, D., and Sompolinsky, H. (2003). Rate models for conductance-based cortical neuronal networks. *Neural Comput.* **15**, 1809–1841. <https://doi.org/10.1162/08997660360675053>. <http://www.ncbi.nlm.nih.gov/pubmed/14511514>.
- Simony, E., Bagdasarian, K., Herfst, L., Brecht, M., Ahissar, E., and Golomb, D. (2010). Temporal and spatial characteristics of vibrissa responses to motor commands. *J. Neurosci.* **30**, 8935–8952. <https://doi.org/10.1523/JNEUROSCI.0172-10.2010>. <http://www.ncbi.nlm.nih.gov/pubmed/20592215>.
- Smith, J.C., Ellenberger, H.H., Ballanyi, K., Richter, D.W., and Feldman, J.L. (1991). Pre-Bötzing complex: a brainstem region that may generate respiratory rhythm in mammals. *Science* **254**, 726–729. <https://doi.org/10.1126/science.1683005>.
- Softky, W.R., and Koch, C. (1993). The highly irregular firing of cortical cells is inconsistent with temporal integration of random epsps. *J. Neurosci.* **13**, 334–350. <http://www.ncbi.nlm.nih.gov/pubmed/8423479>.
- Soloduchin, S., and Shamir, M. (2018). Rhythmogenesis evolves as a consequence of long-term plasticity of inhibitory synapses. *Sci. Rep.* **8**, 13050. <https://doi.org/10.1038/s41598-018-31412-7>. <http://www.ncbi.nlm.nih.gov/pubmed/30158555>.
- Stent, G.S., Kristan, W.B., Friesen, W.O., Ort, C.A., Poon, M., and Calabrese, R.L. (1978). Neuronal generation of the leech swimming movement. *Science* **200**, 1348–1357. <https://doi.org/10.1126/science.663615>. <https://www.ncbi.nlm.nih.gov/pubmed/663615>.
- Takato, J., Nelson, A., Zhou, X., Bolton, M.M., Ehlers, M.D., Arenkiel, B.R., Mooney, R., and Wang, F. (2013). New modules are added to vibrissal premotor circuitry with the emergence of exploratory whisking. *Neuron* **77**, 346–360.
- Takato, J., Park, J.H., Lu, J., Li, S., Thompson, P.M., Han, B.X., Zhao, S., Kleinfeld, D., Friedman, B., and Wang, F. (2021). Constructing an adult orofacial premotor atlas in Allen mouse CCF. *eLife* **10**, e67291. <https://doi.org/10.7554/eLife.67291>. <https://www.ncbi.nlm.nih.gov/pubmed/33904410>.
- Takato, J., Prevosto, V., Thompson, P.M., Lu, J., Chung, L., Harrahill, A., Li, S., Zhao, S., He, Z., Golomb, D., et al. (2022). The whisking oscillator circuit. *Nature*. <https://doi.org/10.1038/s41586-022-05144-8>.
- Tinbergen, N. (1951). *The Study of Instinct* (Oxford University Press).
- Towal, R.B., and Hartmann, M.J. (2006). Right-left asymmetries in the whisking behavior of rats anticipate head movements. *J. Neurosci.* **26**, 8838–8846.

Towal, R.B., and Hartmann, M.J. (2008). Variability in velocity profiles during free-air whisking behavior of unrestrained rats. *J. Neurophysiol.* *100*, 740–752.

Van Vreeswijk, C., Abbott, L.F., and Ermentrout, G.B. (1994). When inhibition not excitation synchronizes neural firing. *J. Comput. Neurosci.* *1*, 313–321. <http://www.ncbi.nlm.nih.gov/pubmed/8792237>.

van Vreeswijk, C., and Hansel, D. (2001). Patterns of synchrony in neural networks with spike adaptation. *Neural Comput.* *13*, 959–992. <https://doi.org/10.1162/08997660151134280>.

van Vreeswijk, C., and Sompolinsky, H. (1996). Chaos in neuronal networks with balanced excitatory and inhibitory activity. *Science* *274*, 1724–1726. <http://www.ncbi.nlm.nih.gov/pubmed/8939866>.

van Vreeswijk, C., and Sompolinsky, H. (1998). Chaotic balanced state in a model of cortical circuits. *Neural Comput.* *10*, 1321–1371. <http://www.ncbi.nlm.nih.gov/pubmed/9698348>.

von Holst, E. (1939/1973). Relative coordination as a phenomenon and as a method of analysis of central nervous function. In *The Collected*

Papers of Erich von Holst, R. Martin, ed. (University of Miami), pp. 33–135.

Wallach, A., Deutsch, D., Oram, T.B., and Ahissar, E. (2020). Predictive whisker kinematics reveal context-dependent sensorimotor strategies. *PLoS Biol.* *18*, e3000571.

Weiss, P. (1941). *Self-Differentiation of the Basic Patterns of Coordination* (Lippincott Williams & Wilkins).

Welker, W.I. (1964). Analysis of sniffing of the albino rat. *Behaviour* *22*, 223–244.

Whittington, M.A., Traub, R.D., and Jefferys, J.G. (1995). Synchronized oscillations in interneuron networks driven by metabotropic glutamate receptor activation. *Nature* *373*, 612–615. http://www.ncbi.nlm.nih.gov/entrez/query.fcgi?cmd=Retrieve&db=PubMed&dopt=Citation&list_uids=7854418.

Wilson, H.R. (2003). Computational evidence for a rivalry hierarchy in vision. *Proc. Natl. Acad. Sci. USA* *100*, 14499–14503. <https://doi.org/10.1073/pnas.2333622100>. <https://www.ncbi.nlm.nih.gov/pubmed/14612564>.

STAR★METHODS

KEY RESOURCES TABLE

REAGENT or RESOURCE	SOURCE	IDENTIFIER
Deposited data		
Raw and analyzed data	This paper	https://doi.org/10.5281/zenodo.7062703
Chemicals, peptides, and recombinant proteins		
Cyanoacrylate glue	MacMaster-Carr	Loctite 401
Buprenorphine	Butler Schein	NDC420123179-05
Experimental models: Organisms/strains		
Two male Long Evans rats, 350 g	Charles River	Strain 006
Software and algorithms		
Julia programming language	Julia computing	https://juliacomputing.com
Code for simulation and numerical calculations	This paper	https://zenodo.org/record/7064635
Other		
Thermister	Measurement Specialties	GAG22K7MCD419
High-speed video camera	Basler	axA204 -90umNIR

RESOURCE AVAILABILITY

Lead contact

Further information and requests for resources should be directed to and will be fulfilled by Dr. David Golomb (golomb@bgu.ac.il).

Materials availability

This study did not generate new unique reagents.

Data and code availability

- All original data has been deposited at <https://doi.org/10.5281/zenodo.7062703> and is publicly available as of the date of publication. The DOI is listed in the [key resources table](#).
- All original code has been deposited at <https://github.com/david-golomb/vIRt> and is publicly available as of the date of publication. The DOI is listed in the [key resources table](#).
- Any additional information required to reanalyze the data reported in this paper is available from the [lead contact](#) upon request.

EXPERIMENTAL MODEL AND SUBJECT DETAILS

Our analysis involved data from past experiments, as noted in the text, and the acquisition and analysis of new data from rats. The Institutional Animal Care and Use Committee at the University of California San Diego approved the protocol for rats for all new data.

METHOD DETAILS

Summary of the rate model

Subpopulation indices: μ and ν , coded as $r \leftarrow vIRt^{ret}$, $p \leftarrow vIRt^{pro}$, $F \leftarrow vFMN$, and $B \leftarrow pBötC$.

Rate equations (Equations 32, 33, 34, 35, 36, and 37) are derived by summing the fast postsynaptic synaptic currents to each neuron and averaging over all presynaptic neurons (Ermentrout, 1994; Seung et al., 2000; Shriki et al., 2003; Golomb et al., 2006a; Hayut et al., 2011) (Equations 38, 39, 40, 41, 42, 43, 44, 45, and 46). They contain effective synaptic weights, denoted by "J", that are proportional to synaptic conductances as well as the difference between the average membrane potential and the synaptic reversal potential. The spike rate is a monotonic function of the total current; we choose a piecewise linear function (Equation 33) (insert in Figure 2C) with a conversion gain of β in units of rate/current, or 1/charge.

The pBötC-to-vIRt feed-forward circuit

The dynamics of the $vIRt^{ret}$ and $vFMN$ subpopulations are each controlled by two equations; one equation describes the activation of the synaptic inputs (Equations 50 and 54) the other the magnitudes of the adaption currents (Equations 51 and 55).

The rate equations for the vIRt and vFMN neurons are in terms of an effective interaction for the fast synapses, denoted J^{Fr} and given by (Equation 41)

$$J^{Fr} = Kg^{Fr} \langle \langle V_i^F(t) - V_{GABA_A} \rangle \rangle_t \quad (\text{Equation 6})$$

where g^{Fr} is the conductance of the vIRt^{ret} inputs to vFMN neurons, V_{GABA_A} is the reversal potential for GABA_A receptors, and $\langle \langle \dots \rangle \rangle_t$ means population- and time-averaged. Typical values of $\langle \langle V_i^F(t) - V_{GABA_A} \rangle \rangle_t$, found numerically, are 20 to 27 mV. V_i^F is the membrane potential of the i th vFMN neuron, and J^{Fr} has units of current.

Effective coefficients that represent the increase of adaptation with increasing spike rate are obtained from the conductances of adaptation currents, i.e.,

$$J_a^F = \gamma^F g_{adapt}^F \quad (\text{Equation 7})$$

for neurons in the vFMN and

$$J_a^r = \gamma^r g_{adapt}^r \quad (\text{Equation 8})$$

for neurons in the vIRt. The constants γ^F and γ^r are determined by a linear fit of the spike rate versus I_{ext} curves (Figure 2C) and J_a^F and J_a^r have units of charge. Lastly, the inhibitory input from the pBötC is given by

$$I^B = g^B \langle \langle V_i^r(t) - V_{GABA_A} \rangle \rangle_t \quad (\text{Equation 9})$$

and has units of current. V_i^r is the membrane potential of the i th vIRt^{ret} neuron. The input is in the form of a square-wave with frequency $f_{pBötC}$ and active duration $\Delta T_{pBötC}$.

Which parameters control the amplitude of a whisk? The amplitude depends on the number of spikes produced by vIRt^{ret} neurons during period $\Delta T_{pBötC}$ and is denoted by N_{spikes}^r . The formulas for N_{spikes}^r (Equations 62, 63, and 77) highlights the competition between the excitatory drive, i.e., $I_{ext}^r - I_0^r$, and the rhythmic inhibition from the pBötC. When I^B is moderate in magnitude, the vIRt^{ret} neurons cease to spike just after the beginning of the pBötC activity, and when it is sufficiently large the vIRt^{ret} neurons are silent during the whole pBötC activity period.

A further insight provided by the rate analysis (Equations 62 and 63) is that the response time of the feed-forward circuit is reduced from the time constant of the slow adaptation, i.e., τ_a^r , to $\tau_a^r / (1 + \beta^r J_a^r)$. While the slow adaptation current will be shown to be critical for the generation of oscillations by the full vIRt circuit, the slow-time is accelerated for feed-forward transmission. This leads to the rapid inhibition of vIRt^{ret} cells and the near synchrony of inhalation and whisking.

The vIRt oscillator

There are three operating domains of the network as a function of the difference in effective interactions (Equations 105 and 111), i.e.,

$$\Delta J_{syn} \equiv J_{inter} - J_{intra} \quad (\text{Equation 10})$$

where

$$J_{inter} = Kg_{inter} \langle \langle V_i^{vIRt}(t) - V_{GABA_A} \rangle \rangle_t \quad (\text{Equation 11})$$

and

$$J_{intra} = Kg_{intra} \langle \langle V_i^{vIRt}(t) - V_{GABA_A} \rangle \rangle_t. \quad (\text{Equation 12})$$

Both J_{inter} and J_{intra} have units of current.

Noting that (Equation 41)

$$\Delta g_{syn} \propto \Delta J_{syn}, \quad (\text{Equation 13})$$

we present results in the main text in terms of Δg_{syn} , where $\Delta g_{syn} = g_{inter} - g_{intra}$, to enable direct comparisons between calculated results from the rate equations and the results from simulations of the conductance-based equations.

Uniform state

The two vIRt subpopulations are concurrently active (Soloduchin and Shamir, 2018) (Equation 105) for values of ΔJ_{syn} less than that of a threshold, denoted J_{tr} , where $g_{tr} \propto J_{tr}$. The value of J_{tr} , in the simplifying limit of $\tau_s \ll \tau_a^r$ where τ_s is the time constant of synapses throughout the vIRt network, corresponds to the scale of the fast membrane current, i.e.,

$$J_{tr} \approx \frac{1}{\tau_s \beta^r}. \quad (\text{Equation 14})$$

The constant output is maintained even if the adaptation current goes to zero. The net neuronal activity is nominally given by the ratio between external input that drives the vIRt neurons and a term that includes the sum of the currents, inhibitory synaptic currents and adaptation, that quench activity (Equation 101).

Oscillatory state

The network activity oscillates between the vIRt^{ret} and vIRt^{pro} subpopulations when the value of ΔJ_{syn} exceeds J_{tr} , but lies below a second, larger threshold, denoted J_{det} , with $g_{\text{det}} \propto J_{\text{det}}$. The value of J_{det} is

$$J_{\text{det}} = J_{\text{tr}} + \frac{J_{\text{a}}^r}{\tau_s} \quad (\text{Equation 15})$$

where the additional term represents the scale of the slow adaptive current. In the oscillatory state, the average activity is linearly proportional to the external input minus the current threshold, $I_{\text{ext}}^r - I_0^r$. Critically, oscillations will occur even if $J_{\text{intra}} = 0$, i.e., for a network with connections only between the two subpopulations of vIRt neurons.

Our formulas highlight four features of the oscillatory output of the vIRt. The period of the rhythm, T_{vIRt} (Figures 5F and 5G), is found from the solution of a transcendental equation (Equation 124) of two dimensionless parameters. First, $1/T_{\text{vIRt}}$ decreases monotonously toward zero with increasing values of g_{inter} (Equations 127, 129, 132, 133, 134, 135, 136, 137, 138, and 139) (Figure 5F). Second, the period is independent of the strength of the external input, I_{ext}^r (Equations 116 and 124) (Figure 5G). Thus whisking frequency and amplitude decouple. Third, the period scales linearly with the adaptation time-constant, i.e., $T_{\text{vIRt}} \propto \tau_a^r$ (Equation 124). Lastly, the period is independent of the conversion gain, β^r , in the high gain limit.

Bistable state

The network dynamics turns bistable, with only one of the two subpopulations active, when $\Delta J_{\text{syn}} > J_{\text{det}}$. Here too, the average activity is linearly proportional to $I_{\text{ext}}^r - I_0^r$.

Glossary

- N^μ : number of neurons in the μ -th subpopulation, $\mu = r, p, F$, or B .
- $K^{\mu\nu}$: The average number of synaptic connections from ν -th subpopulation to μ -th subpopulation.
- $\tilde{C}_{ij}^{\mu\nu}$: connectivity matrix element between j -th neuron in ν -th subpopulation to i -th neuron in μ -th subpopulation.
- C : membrane capacitance per unit area.
- V_i^μ : membrane potential of the i -th neuron from the μ -th subpopulation.
- $I_{\text{ion},j}^\mu$: intrinsic ionic current from a specific type of the i -th neuron from the μ -th subpopulation. “ion” can be L, Na, NaP, Kdr, adapt, or h.
- g_{ion}^μ : intrinsic ionic conductance from a specific ionic type for the μ -th subpopulation. “ion” can be L, Na, NaP, Kdr, adapt, or h.
- Δg_L : width of the distribution of the leak conductance.
- Δg_{adapt} : width of the distribution of the adaptation conductance.
- V_{rev} : reversal potential of an ionic current. The current can be Na^+ , K^+ , h, GABA_A (for GABA-mediated synapses) or Glu (for glutamergic synapses).
- I_{ext}^μ : external input to a neuron from the μ -th subpopulation.
- $I_{\text{syn},i}^{\mu\nu}$: synaptic input from all the neurons from the ν -th subpopulation to the i -th neuron from the μ -th subpopulation.
- m : activation variable of I_{Na} .
- h : inactivation variable of I_{Na} .
- p : activation variable of I_{NaP} .
- n : activation variable of I_{Kdr} .
- z : activation variable of I_{adapt} .
- r : activation variable of I_h .
- $\text{var}_\infty^\mu(V)$: steady-state value of an activation or an inactivation variable as a function of V . “var” may be h, p, n, z, or r.
- τ_{var}^μ : time constant of an activation or an inactivation variable. “var” may be h, p, n, z, or r.
- $G_{\text{syn},j}^{\mu\nu}$: total synaptic conductance from all contributing neurons in ν -th subpopulation to neuron i in μ -th subpopulation.
- $g^{\mu\nu}$: average synaptic conductance from all neurons in ν -th subpopulation ν onto a neuron in μ -th subpopulation.
- $g_{\text{intra}} \equiv g^r = g^{\text{pp}}$: average synaptic conductance from all the neurons within the vIRt^{ret} subpopulation onto to one neuron in the vIRt^{ret} subpopulation. Ditto for the vIRt^{pro} subpopulation.
- $g_{\text{inter}} \equiv g^r = g^{\text{pr}}$: average synaptic conductance from all of the neurons within the vIRt^{ret} subpopulation onto to one neuron in the vIRt^{pro} subpopulation. And visa versa.
- \tilde{s}_j^r : a synaptic variable from presynaptic neuron j in the ν -th subpopulation.
- $t_{j,k}^r$: the time of the k -th spike of the j -th neuron in the ν -th subpopulation.
- τ_s^r : synaptic decay time constant.
- l : index of pBötC period of activity.
- $t_{\text{pBötC},l}$: starting time of activity in the l -th pBötC cycle.
- $T_{\text{pBötC},l}$: duration of the l -th pBötC cycle, composed of an active and a silent phase. If these durations are constant, then $T_{\text{pBötC},l} = T_{\text{pBötC}}$.
- $f_{\text{pBötC}} = 1/T_{\text{pBötC}}$: frequency of pBötC input to the vIRt system where $T_{\text{pBötC}} = \langle T_{\text{pBötC},l} \rangle_l$

- t_l^B : starting time of the l -th period of the pBötC.
 $\Delta T_{\text{pBötC}}$: duration of the active state of the pBötC.
 T_{rand} : variability of the time period of the pBötC.
 h^B : function denoting the dependency of the pBötC activity on time.
 $[\text{Ca}^{2+}]_i$: normalized intracellular $[\text{Ca}^{2+}]$ in the i -th muscle cell.
 C_k : coefficients used for calculating $[\text{Ca}^{2+}]_i$.
 τ_{wr} : rise time constant of $[\text{Ca}^{2+}]$ inside a cell.
 τ_{wc} : decay time constants of $[\text{Ca}^{2+}]$ inside a cell.
 r_0 : amplitude of Ca^{2+} entry to a cell.
 F : normalized muscle force.
 A_0 : coefficient controlling muscle force.
 θ : vibrissa sweep angle.
 τ_{wm} : time scale of the dependency of vibrissa angle on the muscle force.
 A_1 : coefficient controlling the dependency of vibrissa angle on the muscle force.
 M^μ : population-average spike rate of the μ -th subpopulation.
 $\text{ISI}_{\text{max,median}}^\mu$: the maximum value of the ISI for each neuron within the μ -th subpopulation is calculated and $\text{ISI}_{\text{max,median}}^\mu$ is the median of these maximal values.
 f_{vIRt} : frequency of vIRt-induced bursting oscillations, with $T_{\text{vIRt}} = 1/f_{\text{vIRt}}$
 CV_2^μ : coefficient of variation of the μ -th subpopulation (Holt et al., 1996).
 θ_{sd} : the standard deviation of $\theta(t)$.
 θ^{set} : the local maximum of $\theta(t)$.
 θ^{amp} : the whisking amplitude.
 $t_{\text{w,min}}$: time of the global minimum of $\theta(t)$.
 s^μ : population-averaged synaptic variable of the μ -th subpopulation (rate model).
 a^μ : population-averaged adaptation variable of the μ -th subpopulation (rate model).
 a_0^μ : a^μ for $t = 0^+$, just after the onset of pBötC activity.
 β^μ : slope of the f - I curve for the μ -th subpopulation (rate model).
 I_0^μ : current threshold of a neuron from the μ -th subpopulation (rate model).
 I_{ext}^μ : external current that drives a neuron from the μ -th subpopulation (rate model).
 I_{ext}^μ : external current into a neuron from the μ -th subpopulation minus the current threshold (rate model).
 J_a^μ : adaptation strength (rate model).
 τ_a^μ : adaptation time constant (rate model).
 $J^{\mu\nu}$: effective synaptic coupling between the ν -th and μ -th subpopulations (rate model).
 e^μ : +1 if the μ -th subpopulation has excitatory synaptic output and -1 if it has inhibitory output.
 $J_{\text{intra}} \equiv J^{\text{r}} = J^{\text{pp}}$: effective synaptic self-coupling within the vIRt^{ret} or the vIRt^{pro} subpopulations.
 $J_{\text{inter}} \equiv J^{\text{p}} = J^{\text{p}}$: effective synaptic self-coupling between the vIRt^{ret} and the vIRt^{pro} subpopulations.
 γ^μ : ratio between effective interactions J_a^μ (rate model) and synaptic conductances g_{adapt}^μ (CB model).
 $I_{\text{intra}}^{\text{CB}}$: average synaptic current from a vIRt subpopulation onto a neuron from the same subpopulation (CB model).
 $I_{\text{intra}}^{\text{rate}}$: average synaptic current from a vIRt subpopulation onto a neuron from the same subpopulation (rate model).
 I^{B} : current from the pBötC during its active phase to the vIRt^{ret} subpopulation.
 F_{fit} : fit of the muscle force. Related parameters: A_L , M_L^F , A
 P_{fit} : polynomial used to define F_{fit} in terms of the parameters M_1^F , M_2^F , M_3^F , B_2 , and B_3 .
 \hat{M}^μ : $\beta^\mu \times$ the total current into a neuron from μ -th subpopulation minus the current threshold (rate model).
 a_{func}^r : function defined by Equation 62.
 N_{spikes}^μ : number of spikes fired by a neuron from the μ -th subpopulation during pBötC activity.
 $N_{\text{spikes;func}}^r$: spike function defined by Equation 63.
 \hat{A} , \hat{B} , \hat{C} , \hat{D} : terms defined by Equation 66.
 $t_{M^F > 0}$: the time below which $\hat{M}_F(t) \geq 0$.
 $N_{\text{spikes; } M^F > 0}^F$: function defined by Equation 73.
 $T_{M^F = 0}$: the time below which $M^F(t) = 0$.
 \tilde{I} : term defined by Equation 92.
 F_m : proportionality constant in Equation 93.
 $I_{\text{onset}}^{\text{B}}$: the I^{B} value above which the vibrissae begin to oscillate.
 $I_{\text{sat}}^{\text{B}}$: saturation value of I^{B} .

- $T_{\theta, \max}$: time for maximal protraction.
 A_{stab} : 4×4 stability matrix.
 $A_{\text{stab}, \pm}$: reduced, 2×2 stability matrices.
 \vec{a} : two-dimensional vector, used for stability calculation.
 J_{tr} : trace of the matrix $A_{\text{stab}, -}$.
 J_{det} : determinant of the matrix $A_{\text{stab}, -}$.
 \tilde{J} : expression defined in Equation 116.
 J_{nor} : expression defined in Equation 132
 $\tilde{E}(T_{\text{vIRt}})$: expression defined in Equation 134.
 $\tilde{F}(T_{\text{vIRt}})$: expression defined in Equation 136.
 $\langle \dots \rangle_t$: average over time.
 $\langle \dots \rangle_i$: average over the neurons in a population.
 x : factor of blockade of inhibition in the vIRt^{ret}
 φ : phase of whisking oscillations.
 $t_{w,j}$: the time of the maximal whisking angle during the i -th whisk in the breathing cycle.

Conductance-based (CB) network model: architecture

The circuit model includes three subpopulations of neurons: inhibitory glycinergic/GABAergic vIRt^{ret} and vIRt^{pro} subpopulation and cholinergic vFMN motoneurons; see “Detailed background” in the Introduction (Figures 2A and 2E). vIRt^{ret} neurons correspond to vIRt^{PV} neurons in (Takatoh et al., 2022). The letters r, p, F, and B denote the vIRt^{ret} , vIRt^{pro} , vFMN, and preBöt neuronal subpopulations respectively; mathematical symbols have these letters as superscripts. The vIRt^{ret} and vIRt^{pro} subpopulations have the same properties unless otherwise stated. Quantities defining both the vIRt^{ret} , and vIRt^{pro} subpopulations are denoted by “r”.

The numbers and strengths of synaptic connections from vIRt neurons to other vIRt neurons and to vFMN neurons are known only in an approximate manner. The intrinsic properties of vIRt neurons and the synaptic connectivity within the vIRt can only be estimated. Our strategy is to define a set of parameter values, named “reference parameter set”, close to measured values when known (Golomb et al., 1994; Gutnisky et al., 2017). We vary parameters to explore the role of those parameters on the system dynamics. The number of vIRt neurons is estimated to be on the order of 100 to 1000 (Moore et al., 2013) and about 60 vFMN neurons project to an intrinsic muscle connecting two vibrissae (Guest et al., 2018).

CB network model: sizes and connectivity

The number N^μ denotes the number of neurons in the μ -th subpopulation.

- We choose $N^r = N^p = N^F = 100$.

Simulations show that taking a larger value of N has a small effect on the results of this manuscript. The probability that a neuron from the ν -th presynaptic subpopulation forms a synapse on a neuron from the μ -th postsynaptic subpopulation is governed by a uniform distribution with value $K^{\mu\nu}/N^\nu$ (Golomb and Hansel, 2000) (Figure 2A). The number $K^{\mu\nu}$ denotes the average number of inputs from the ν -th subpopulation that are projected to the μ -th subpopulation.

- We set $K^{\mu\nu} = K = 25$ for all μ and ν that $K^{\mu\nu} \neq 0$, i.e., $\mu = r, p, \text{ or } F$ and $\nu = r \text{ or } p$.

We define the matrix $\tilde{C}_{ij}^{\mu\nu}$ to be 1 if the j -th neuron from the ν -th subpopulation projects to the i -th neuron from the μ -th subpopulation, and 0 otherwise, such that $\langle \tilde{C}_{ij}^{\mu\nu} \rangle_{i,j} = K^{\mu\nu}/N^\nu$.

CB network model: dynamics of single vFMN neurons

The single-compartment conductance-based model of a motoneuron in the vFMN is based on (Harish and Golomb, 2010; Golomb, 2014). The model includes the transient Na^+ current, I_{Na} , the persistent sodium current, I_{NaP} , and the delayed rectifier K^+ current, I_{Kdr} , that generate spikes (Figure 2B). The slowly-activating current I_{adapt} , for example, an M-type K^+ current, generates the adaptation and afterhyperpolarization observed in motoneurons (Meunier and Borejsza, 2005). The model also includes the leak current I_{L} and the HCN or h-current I_{h} (Nguyen et al., 2004). The current balance equation for the membrane potential of the i -th neuron, V_i^F , where $i = 1, \dots, N^F$, is

$$C \frac{dV_i^F}{dt} = -I_{\text{L},i}^F - I_{\text{Na},i}^F - I_{\text{NaP},i}^F - I_{\text{Kdr},i}^F - I_{\text{adapt},i}^F - I_{\text{h},i}^F + I_{\text{ext}}^F - I_{\text{syn},i}^F \quad (\text{Equation 16})$$

where V is the membrane potential of the neuron and $C = 1 \mu\text{F}/\text{cm}^2$ is the membrane capacitance of the neuron.

The following equations and parameters for the ionic currents are implemented.

Leak current I_{L}^F

$$I_{L_i}^F = g_{L_i}^F (V - V_L) \quad (\text{Equation 17})$$

- $g_{L_i}^F$ is taken at random for each neuron, i , from a uniform distribution between $g_L - \Delta g_L$ and $g_L + \Delta g_L$. The random component prevents spurious synchronization of neuronal spikes.
- We use $g_L = 0.12 \text{ mS/cm}^2$, $\Delta g_L = 0.06 \text{ mS/cm}^2$, and $V_L = -70 \text{ mV}$.

The indices i and F are dropped for simplicity.

Transient Na^+ current, I_{Na} :

$$I_{\text{Na}}(V, h) = g_{\text{Na}} m_{\infty}^3(V) h (V - V_{\text{Na}}) \quad (\text{Equation 18})$$

$$m_{\infty}(V) = 1 / [1 + \exp(- (V - \theta_m) / \sigma_m)].$$

$$dh / dt = [h_{\infty}(V) - h] / \tau_h(V).$$

$$h_{\infty}(V) = 1 / [1 + \exp(- (V - \theta_h) / \sigma_h)].$$

$$\tau_h(V) = \tau_{h0} / [\exp(V - \theta_h) / \sigma_{h1} + \exp(- (V - \theta_h) / \sigma_{h2})].$$

- We use $g_{\text{Na}} = 100 \text{ mS/cm}^2$, $V_{\text{Na}} = 55 \text{ mV}$, $\theta_m = -28 \text{ mV}$, $\sigma_m = 7.8 \text{ mV}$, $\theta_h = -50 \text{ mV}$, $\sigma_h = -7 \text{ mV}$, $\tau_{h0} = 30 \text{ ms}$, $\sigma_{h1} = 15 \text{ mV}$, and $\sigma_{h2} = 16 \text{ mV}$.

Persistent Na^+ current, I_{NaP} :

$$I_{\text{NaP}}(V) = g_{\text{NaP}} p_{\infty}(V) (V - V_{\text{Na}}) \quad (\text{Equation 19})$$

$$p_{\infty}(V) = 1 / [1 + \exp(- (V - \theta_p) / \sigma_p)].$$

- We use $g_{\text{NaP}} = 0.04 \text{ mS/cm}^2$, $\theta_p = -53 \text{ mV}$, and $\sigma_p = 5 \text{ mV}$.

Delayed rectifier K^+ current, I_{Kdr} :

$$I_{\text{Kdr}}(V, n) = g_{\text{Kdr}} n^4 (V - V_{\text{K}}) \quad (\text{Equation 20})$$

$$dn / dt = [n_{\infty}(V) - n] / \tau_n(V).$$

$$n_{\infty}(V) = 1 / [1 + \exp[- (V - \theta_n) / \sigma_n]],$$

$$\tau_n(V) = \tau_{n0} / [\exp((V - \theta_n) / \sigma_{n1}) + \exp(- (V - \theta_n) / \sigma_{n2})].$$

- We use $g_{\text{Kdr}} = 20 \text{ mS/cm}^2$, $V_{\text{K}} = -90 \text{ mV}$, $\theta_n = -23 \text{ mV}$, $\sigma_n = 15 \text{ mV}$, $\tau_{n0} = 7$, $\theta_{n0} = -40 \text{ mV}$, $\sigma_{n1} = 40 \text{ mV}$, and $\sigma_{n2} = 50 \text{ mV}$.

Adaptation current, I_{adapt} :

$$I_{\text{adapt}}(V, z) = g_{\text{adapt}} z (V - V_{\text{K}}) \quad (\text{Equation 21})$$

$$dz / dt = [z_{\infty}(V) - z] / \tau_z$$

$$z_{\infty}(V) = 1 / [1 + \exp(- (V - \theta_z) / \sigma_z)]$$

- We use $g_{\text{adapt}} = 0.3 \text{ mS/cm}^2$, $\theta_z = -45 \text{ mV}$, $\sigma_z = 4.25 \text{ mV}$, $\tau_z = 75 \text{ ms}$

Hyperpolarization-activated h-current I_h :

$$I_h(V, r) = g_h r (V - V_h) \quad (\text{Equation 22})$$

$$dr / dt = [r_{\infty}(V) - r] / \tau_r(V).$$

$$r_{\infty}(V) = [1 + \exp(-(V - \theta_r) / \sigma_r)].$$

$$\tau_r(V) = \tau_{r0} / [\exp((V - \theta_{n1}) / \sigma_{n1}) + \exp(-(V - \theta_{n2}) / \sigma_{n2})].$$

- We use $g_h = 0.05 \text{ mS/cm}^2$, $V_h = -27.4 \text{ mV}$, $\theta_r = -83.9 \text{ mV}$, $\sigma_r = -7.4 \text{ mV}$, $\tau_{r0} = 6000 \text{ ms}$, $\theta_{n1} = -140 \text{ mV}$, $\theta_{n2} = -40 \text{ mV}$, $\sigma_{n1} = 21.6 \text{ mV}$, and $\sigma_{n2} = 22.7 \text{ mV}$.

External depolarizing current I_{ext} :

- vFMN neurons are excited and depolarized by excitatory (Hattox et al., 2002) and neuromodulatory (Cramer and Keller, 2006) inputs from several brain areas. We assume that those inputs evolve slowly with time and treat them as a constant external depolarizing current that enables vFMN neurons to spike in the presence of rhythmic inhibitory input.
- We use $I_{\text{ext}} = 3.1 \mu\text{A/cm}^2$.

External Inhibitory currents I_{syn} :

- The inhibitory synaptic input current from the activity of the vIRt^{ret} neurons is $I_{\text{syn}}^{\text{Fr}}$. It is discussed in detail below.

CB network model: dynamics of single vIRt neurons

The model of a vIRt neuron is derived from the vFMN neuron model. The current balance equation for the membrane potential of the i -th neuron, V_i^{μ} , where $\mu = r$ or p and $i = 1, \dots, N_{\mu}$, is

$$C \frac{dV_i^{\mu}}{dt} = -I_{L,i}^{\mu} - I_{\text{Na},i}^{\mu} - I_{\text{NaP},i}^{\mu} - I_{\text{Kdr},i}^{\mu} - I_{\text{adapt},i}^{\mu} + I_{\text{ext}} - I_{\text{syn},i}^{\text{Fr}} - I_{\text{syn},i}^{\text{PD}} - I_{\text{syn},i}^{\text{B}}. \quad (\text{Equation 23})$$

The parameter modifications with respect to the vFMN neuron model are:

- The adaptation conductance g_{adapt} is taken at random from a uniform distribution between $g_{\text{adapt}} - \Delta g_{\text{adapt}}$ and $g_{\text{adapt}} + \Delta g_{\text{adapt}}$, where $g_{\text{adapt}} = 7 \text{ mS/cm}^2$ and $\Delta g_{\text{adapt}} = 3 \text{ mS/cm}^2$. The random component prevents spurious synchronization of neuronal spikes.
- We now use $\theta_z = -28 \text{ mV}$, $\sigma_z = 3 \text{ mV}$, and $\tau_z = 83 \text{ ms}$ in Equation 21.
- vIRt neurons receive inputs from several brain areas (McElvain et al., 2018), that are represented here by an external current $I_{\text{ext}} = 20 \mu\text{A/cm}^2$ for both vIRt sub-populations.
- The synaptic currents $I_{\text{syn},i}^{\text{Fr}}$, $I_{\text{syn},i}^{\text{PD}}$, and $I_{\text{syn},i}^{\text{B}}$ are inhibitory inputs currents that originate from the activity of the vIRt^{ret}, vIRt^{pro} and pBötC neuronal subpopulations respectively.

CB network model: inhibitory synaptic currents

The rhythmic synaptic inputs that we consider are all inhibitory. The net such input that neuron i from subpopulation μ receives from all contributing neurons in presynaptic subpopulation ν is given by the sum:

$$I_{\text{syn},i}^{\mu\nu} = G_{\text{syn},i}^{\mu\nu}(t)(V_i^{\mu} - V_{\text{GABA}_A}). \quad (\text{Equation 24})$$

- The total conductance $G_{\text{syn},i}^{\mu\nu}$ for $\mu = F, p$, or r and $\nu = p$ or r is:

$$G_{\text{syn},i}^{\mu\nu}(t) = g_{\mu\nu} \sum_{j=1}^{N_{\nu}} \tilde{C}_{ij}^{\mu\nu} \tilde{s}_j^{\nu}(t). \quad (\text{Equation 25})$$

Unless noted, we assume symmetry in connectivity within the vIRt. Thus $g_{rr} = g_{pp}$ and $g_{rp} = g_{pr}$.

- We define $g_{\text{intra}} \equiv g^{rr} = g^{\text{pp}}$ and $g_{\text{inter}} \equiv g^{pr} = g^{pr}$.
- The pre-synaptic activation variable, \tilde{s}_j^{ν} from neuron j in the ν -th subpopulation is:

$$\tilde{s}_j^{\nu} = \sum_k \exp\left[-\left(t - t_{j,k}^{\nu}\right) / \tau_s^{\nu}\right] \Theta\left(t - t_{j,k}^{\nu}\right) \quad (\text{Equation 26})$$

where Θ is the Heaviside function.

- The j -th pre-synaptic neuron spikes at times $t_{j,k}^{\nu}$, where k is the spike index.

- The variable τ_s^{ν} is the time constant of synaptic decay.
- The pBötC inhibitory input to the vIRt sub-populations, i.e., the total conductance $G_{syn,j}^{\mu\nu}$ for $\mu = p$ or r and $\nu = B$, is modeled as lumped oscillating square-wave pulses, i.e.,

$$G_{syn,j}^{\mu B}(t) = g^{\mu B} h^B(t - t_{pBötC,l}) \quad (\text{Equation 27})$$

where $h^B(t)$ is a periodic sequence of rectangular pulses. The l -th cycle starts at time $t_{pBötC,l}$, $l = 1, 2, \dots$, and lasts for a duration of $T_{pBötC,l}$, such that $t_{pBötC,l+1} = t_{pBötC,l} + T_{pBötC,l}$, where $T_{pBötC,l}$ is the duration between the starting times of the l -th and the $(l + 1)$ -th cycles of the pBötC, and $t_{pBötC,1} = 0$.

- The pBötC is active during a time interval $\Delta T_{pBötC}$ following the cycle onset and, clearly, $T_{pBötC,l} > \Delta T_{pBötC}$. The activity function of the pBötC is therefore where, for the l -th cycle, $h_B(t - t_{pBötC,l}) = 1$ for $0 \leq t - t_{pBötC,l} \leq \Delta T_{pBötC}$ and is 0 for $\Delta T_{pBötC} < t - t_{pBötC,l} < T_{pBötC,l}$.
- The values of $T_{pBötC,l}$ are randomly chosen from cycle-to-cycle and are picked up at random from a uniform distribution between $T_{pBötC} - T_{rand}/2$ and $T_{pBötC} + T_{rand}/2$. All vIRt^{ret} neurons receive the same input from the pBötC.
- We choose $\tau_s^{\nu} = \tau_s = 10$ ms, $V_{GABA_A} = -80$ mV, $T_{pBötC} = 700$ ms, $T_{rand} = 150$ ms, and $\Delta T_{pBötC} = 70$ ms unless otherwise stated.
- The pBötC average frequency is $f_{pBötC} = 1/T_{pBötC}$.

CB network model: vibrissa movement

The transformation from spiking of vFMN neurons to vibrissa movement is computed based on a simplified version of a model of vibrissa movement (Simony et al., 2010). The normalized Ca^{2+} concentration in the muscle cells that belong to a motor unit, denoted $[Ca^{2+}]_i$, is determined by the presynaptic motoneuron. The value of $[Ca^{2+}]_i$ for the interval $t_{i,k}^F \leq t < t_{i,k+1}^F$, where $t_{i,k}^F$ is the time of the k -th spike of the i -th vFMN neuron, is

$$[Ca^{2+}]_i(t) = \frac{r_0 \tau_{wc}}{\tau_{wc} - \tau_{wr}} \left[e^{-(t - t_{i,k}^F)/\tau_{wc}} - e^{-(t - t_{i,k}^F)/\tau_{wr}} \right] + C_k e^{-(t - t_{i,k}^F)/\tau_{wc}}, \quad (\text{Equation 28})$$

where

$$C_k = \begin{cases} 0 & , k = 1 \\ C_{k-1} e^{-\Delta t_{i,k-1}/\tau_{wc}} + \frac{r_0 \tau_{wc}}{\tau_{wc} - \tau_{wr}} \left(e^{-\Delta t_{i,k-1}^F/\tau_{wc}} - e^{-\Delta t_{i,k-1}^F/\tau_{wr}} \right) & , k > 1 \end{cases} \quad (\text{Equation 29})$$

$$\text{with } \Delta t_{i,k}^F = t_{i,k+1}^F - t_{i,k}^F.$$

- The dependence of the normalized muscle force F on $[Ca^{2+}]_i$ is

$$F([Ca^{2+}]_i) = A_0 \frac{[Ca^{2+}]_i^4}{1 + [Ca^{2+}]_i^4}. \quad (\text{Equation 30})$$

- The vibrissa angle dynamics are over-damped and thus follow the muscle force according to a first-order linear differential equation

$$\frac{d\theta}{dt} = -\frac{\theta}{\tau_{wm}} + A_1 \sum_{i=1}^{N_F} F \quad (\text{Equation 31})$$

where the sum is over all the motor units that are innervated by vFMN neurons and belong to the same muscle. This approximation to the motion becomes exact for small whisking angles.

- Following Simony et al. (2010), we take $r_0 = 1.9$, $\tau_{wr} = 5$ ms and $\tau_{wc} = 6$ ms. We also take $A_0 = 1$ mg \times mm/ms², $\tau_{wm} = 20$ ms, and $A_1 = 12^\circ$ ms/(mg \times mm); the latter choice makes the variation of θ within the experimentally observed range.

Schema for a rate model

We reduce the CB model of the vIRt network to a rate model. The reduction is based on (Shriki et al., 2003; Golomb et al., 2006a; Hayut et al., 2011). The connections between the CB and rate description is in terms of the time-averaged spike rates of all the neurons in the μ -th subpopulation, where averaging occurs over long times, i.e., over many whisking cycles during oscillatory states, and over the neurons in a sub-population. This average is given by the parameter M^μ . For the rate model, M^μ , is assumed to depend on the effective input current to the neuron as a threshold-linear function

$$M^\mu = \beta^\mu \left[\sum_\nu J^{\mu\nu} \varepsilon^\nu s^\nu - a^\mu + I_{\text{ext}}^\mu - I_0^\mu \right]_+ \quad (\text{Equation 32})$$

The components of this formalism are:

- The parameter β^μ is the slope of the single-neuron f - I curve for a fixed value of a^μ . This curve is assumed to be linear above current threshold, defined by

$$[x]_+ = \begin{cases} 0 & , x \leq 0 \\ x & , x > 0 \end{cases} \quad (\text{Equation 33})$$

- The coefficient $J^{\mu\nu}$ is the effective synaptic coupling between the ν -th and the μ -th subpopulations. We define $J_{\text{intra}} \equiv J^{\text{rr}} = J^{\text{pp}}$ and $J_{\text{inter}} \equiv J^{\text{rp}} = J^{\text{pr}}$.
- The sign of the coupling is

$$\varepsilon^\nu = \begin{cases} +1 & , \text{excitatory synapses} \\ -1 & , \text{inhibitory synapses} \end{cases} \quad (\text{Equation 34})$$

- The population-averaged synaptic variable s^ν are dynamical variables of the system, evolving according to

$$\frac{ds^\nu}{dt} = -\frac{s^\nu}{\tau_s} + M^\nu \quad (\text{Equation 35})$$

where $\nu = p$ or r is the index of the presynaptic subpopulation and we took $\tau_s \equiv \tau_s^r = \tau_s^p$.

- The population-average of the activation variable of the adaptation current, I_{adapt} (Equation 21), evolves according to (Hansel and Sompolinsky, 1998)

$$\frac{da^\mu}{dt} = \frac{-a^\mu + J_a^\mu M^\mu}{\tau_a^\mu}, \quad (\text{Equation 36})$$

where J_a^μ is the adaptation strength and τ_a^μ is the adaptation time constant that is set to be equal to τ_z^μ of the μ -th subpopulation. The original rate formalism (Shriki et al., 2003; Golomb et al., 2006a; Hayut et al., 2011) was developed for only slow variations in population spiking activity. However, a^μ evolves slower than the other variables. Thus we consider a^μ as a separate dynamical variable for each subpopulation.

The role of adaptation conductances depends on the intrinsic neuronal properties and on the circuit in which the neurons are embedded. Adaptation conductances may linearize the f - I curve of a single neuron while it leaving it spiking tonically (Ermentrout, 1998), or generate bursting (Golomb et al., 2006b). It may generate synchronized bursts in networks of excitatory neurons (van Vreeswijk and Hansel, 2001), and asynchronized bursts in networks with inhibitory connections (Shapiro et al., 2007; this article). In these models, adaptation is key factor that supplies the reduction in spike rate that is essential for bursting oscillations. In fact, the adaptation time constant in our model scales the period of the oscillations.

- The parameter I_0^μ is the current threshold of a neuron from the μ -th subpopulation (insert in Figure 2C). We define

$$\tilde{I}_{\text{ext}}^\mu \equiv I_{\text{ext}}^\mu - I_0^\mu \quad (\text{Equation 37})$$

and take $\tilde{I}_{\text{ext}} = \tilde{I}_{\text{ext}}^r = \tilde{I}_{\text{ext}}^p$.

Reduction of a CB model to a rate model

To fit the rate model to the CB model, we compute the f - I curve of the single neuron model for several values of g_{adapt}^{μ} (Figure 2C). Such f - I curves are close to linear functions for large values of g_{adapt}^{μ} (Shriki et al., 2003). For simplicity, we consider only the effects of synaptic conductances on the input currents to the post-synaptic neurons, and not on the input conductance.

- For a single isolated neuronal subpopulation with external input I_{ext}^{μ} and without any synaptic coupling to itself or to other subpopulations, we compute the average spike rate at steady state from the rate model, (Equations 32, 35, and 36) (Hayut et al., 2011)

$$M^{\mu} = \frac{\beta^{\mu} [I_{\text{ext}}^{\mu} - I_0^{\mu}]_+}{1 + \beta^{\mu} J_a^{\mu}} \quad (\text{Equation 38})$$

- Under the additional assumptions that the adaptation constant J_a^{μ} in the rate model (Equation 36) is proportional to g_{adapt}^{μ} in the CB model (Equation 21), and that I_0^{μ} in the rate model is the value of I_{ext}^{μ} in the CB model for the onset of spiking of the single neuron model, we have

$$M^{\mu} = \frac{\beta^{\mu} [I_{\text{ext}}^{\mu} - I_0^{\mu}]_+}{1 + \beta^{\mu} \gamma^{\mu} g_{\text{adapt}}^{\mu}} \quad (\text{Equation 39})$$

where γ^{μ} is the proportionality constant between J_a^{μ} and g_{adapt}^{μ} .

- For the vIRt neuron model, we fit the right-hand-side of Equation 39 to the f - I curves or, here, M - I_{ext} , curves for $g_{\text{adapt}}^r = 3, \dots, 7$ mS/cm² and I_{ext}^r between $I_0^r = 0.29$ and 20 μ A/cm² (Figure 2C). We obtain: $\beta^r = 0.0175$ cm²/ms $\cdot\mu$ A and $\gamma^r = 24.7$ ms \cdot mV.
- For the vFMN neuron model, we fit the right-hand-side of Equation 39 for $g_{\text{adapt}}^F = 0.3$ and 0.6 mS/cm² and I_{ext}^F between $I_0^F = 0.46$ and 6 μ A/cm². We obtain: $\beta^F = 0.0305$ cm²/ms $\cdot\mu$ A and $\gamma^F = 61$ ms \cdot mV.
- To estimate $J^{\mu\nu}$, we note that the current originating from the ν -to- μ coupling during steady-state is $I_{\text{rate}}^{\mu\nu} = -J^{\mu\nu} \tau_s M^{\nu}$ (Equations 32 and 35). In the CB model, the population-average of the same current is, ignoring correlations (Equations 23, 24, 25, and 26) (Argaman and Golomb, 2018),

$$-I_{\text{CB}}^{\mu\nu} = -K^{\mu\nu} g^{\mu\nu} \langle \langle \bar{s}^{\nu} \rangle_t \rangle_i \langle \langle V^{\mu}(t) - V_{\text{GABA}_A} \rangle_t \rangle_i \quad (\text{Equation 40})$$

where $\langle \langle \dots \rangle_t \rangle_i$ denotes time- and population-averaging.

- The condition to obtain $I_{\text{rate}}^{\mu\nu} = -I_{\text{CB}}^{\mu\nu}$ is

$$J^{\mu\nu} = K^{\mu\nu} g^{\mu\nu} \langle \langle V^{\mu}(t) - V_{\text{GABA}_A} \rangle_t \rangle_i \quad (\text{Equation 41})$$

To estimate $\langle \langle V^{\mu}(t) - V_{\text{GABA}_A} \rangle_t \rangle_i$, we simulate the single neuron model without external input and average $V^{\mu}(t)$ over a long time. We find that the typical values of $\langle \langle V^{\mu}(t) - V_{\text{GABA}_A} \rangle_t \rangle_i$ are 27 mV for the vIRt neuron model ($\mu = r$ or p ; Equation 23) and 20 mV for the vFMN neuron model ($\mu = F$; Equation 16). These values correspond to the average membrane potential of a single neuron driven by the current I_{ext}^{μ} , ignoring the membrane potential during spikes above -25 mV.

- The synaptic currents are given by

$$I_{\text{syn},j}^B(t) = I^B h^B(t - t_{\text{pBötC},j}) \quad (\text{Equation 42})$$

where $I^B = g^{\text{rB}} \langle \langle V^r(t) - V_{\text{GABA}_A} \rangle_t \rangle_i$ (Equations 23, 24, and 27).

Rate model for vibrissa movement

We reduce the mechanical model (Equations 28, 29, 30, and 31) to a rate representation by computing the time-average of the muscle force, denoted F , as a function of the spike rate M^F for a tonically-spiking vFMN neuron (Equations 28, 29, and 30).

- The force is found by multiplying the spike rate of a single neuron by the number of vFMN neurons, i.e., N^F . It increases supra-linearly with M^F for moderate M^F values and saturates at high M^F values due to the nonlinear dependence of F on $[\text{Ca}^{2+}]_i$ (Equation 30) (Figure 2D).
- To quantify the dependency of F on M^F , we use the function:

$$F_{\text{fit}}(M^F) = A_L \log\left(1 + \frac{M^F}{M_L^F}\right) + A \frac{P_{\text{fit}}(M^F)}{1 + P_{\text{fit}}(M^F)} \quad (\text{Equation 43})$$

where

$$P_{\text{fit}}(M^F) = \frac{M^F}{M_1^F} + B_2 \left(\frac{M^F}{M_2^F}\right)^2 + B_3 \left(\frac{M^F}{M_3^F}\right)^3. \quad (\text{Equation 44})$$

Fitting Equation 44 to the curve obtained by simulations for M^F between 0 and 500 Hz yields the following parameters: $A_L = 1.02 \text{ mg}\cdot\text{mm}/\text{ms}^2$, $M_L^F = 77 \text{ s}^{-1}$, $M_1^F = 526 \text{ s}^{-1}$, $M_2^F = 612 \text{ s}^{-1}$, $M_3^F = 460 \text{ s}^{-1}$, $A = 9.23 \text{ mg}\cdot\text{mm}/\text{ms}^2$, $B_2 = -23$, and $B_3 = 152$. The fitted curve is almost indistinguishable from the simulation results (Figure 2D).

- In the rate representation, the vibrissa angle (Equation 31) becomes

$$\frac{d\theta}{dt} = -\frac{\theta}{\tau_{\text{vm}}} + F_{\text{fit}}(M^F). \quad (\text{Equation 45})$$

- For the special case of M^F constant in time, the vibrissa set-point angle is (Equations 43 and 45)

$$\theta_{\text{max}} = \tau_{\text{vm}} F_{\text{fit}}(M^F). \quad (\text{Equation 46})$$

Analytical solution of the rate model for the pBötC-vIRt^{ret}-vFMN circuit

We consider a feed-forward pBötC-vIRt^{ret}-vFMN circuit without any inhibitory connections between vIRt neurons.

- We assume that the pBötC input to the vIRt^{ret} (Equations 27 and 42) is periodic ($T_{\text{rand}} = 0$) and is equal to

$$I_{\text{syn}}^B(t) = I^B h^B(t - nT_{\text{pBötC}}) \quad (\text{Equation 47})$$

for $nT_{\text{pBötC}} \leq t < (n+1)T_{\text{pBötC}}$.

- The average activity of the vIRt^{ret} subpopulation (Equations 35 and 36) becomes:

$$M^r = [\widehat{M}^r]_+ \quad (\text{Equation 48})$$

$$\widehat{M}^r = \beta^r [I_{\text{ext}}^r - I^B h^B(t - nT_{\text{pBötC}}) - a^r] \quad (\text{Equation 49})$$

$$s^r = -\frac{s^r}{\tau_s} + M^r \quad (\text{Equation 50})$$

$$\dot{a}^r = \frac{-a^r + J_a^r M^r}{\tau_a^r}. \quad (\text{Equation 51})$$

- Similarly, the average activity of the vFMN subpopulation (Equations 35 and 36) becomes:

$$M^F = [\widehat{M}^F]_+ \quad (\text{Equation 52})$$

$$\widehat{M}^F = \beta^F [I_{\text{ext}}^F - J^F s^r - a^F] \quad (\text{Equation 53})$$

$$s^F = -\frac{s^F}{\tau_s} + M^F \quad (\text{Equation 54})$$

$$a^F = \frac{-a^r + J_a^r M^r}{\tau_a^r}. \quad (\text{Equation 55})$$

Note that the values of \hat{M}^r and \hat{M}^F can be either positive or negative.

- We solve [Equations 48, 49, 50, 51, 52, 53, 54, and 55](#) using the approximation $\tau_s \ll \tau_a^r$ and $\tau_s \ll \tau_a^F$. This implies

$$s^r = \tau_s M^r \quad (\text{Equation 56})$$

and

$$s^F = \tau_s M^F. \quad (\text{Equation 57})$$

- The network is feed-forward and we therefore first compute the values of M^r and a^r and then the values of M^F and a^F . We assume that the pBötC switches from silent to active at $t = 0$, after it has been oscillating for at least one cycle.
- Case of a slow breathing rate. This occurs when $\tau_a^r \ll T_{\text{pBötC}} - \Delta T_{\text{pBötC}}$ and $\tau_a^F \ll T_{\text{pBötC}} - \Delta T_{\text{pBötC}}$. The values of the activities a^r and a^F take on the steady state values, denoted by a_0^r and a_0^F respectively. a_0^r is found from [Equations 48, 49, 50, and 51](#) with $h_B(0^-) = 0$, so that

$$a_0^r = \frac{\beta^r J_a^r \tilde{I}_{\text{ext}}^r}{1 + \beta^r J_a^r}. \quad (\text{Equation 58})$$

Similarly, a_0^F is found from [Equations 52, 53, 54, and 55](#), so that

$$a_0^F = 0. \quad (\text{Equation 59})$$

- For faster breathing rates, we start with a particular value of a_0^r , compute $a^r(T_{\text{pBötC}})$ as described below, and find the steady-state value of a_0^r , i.e., the value obtained after many breathing periods by solving $a^r(T_{\text{pBötC}}) = a_0^r$. Using this value of a_0^r , we compute a_0^F by solving the equation $a^F(T_{\text{pBötC}}) = a_0^F$. In principle, the stability of this solution for a_0^r and a_0^F should be calculated. Comparison with simulation, however, shows that the solution is always stable, and we do not carry out the stability calculation here. We limit our calculation to the case where the vFMN subpopulation is silent before each duration of pBötC activity, i.e., $M_0^F(t) = 0$ for $\Delta T_{\text{pBötC}} < t < T_{\text{pBötC}}$. The calculation depends on the values of $\tilde{I}_{\text{ext}}^r - I^B$ and a_0^r . We consider three cases and several subcases ([Figure S1](#)).
- **A.** $\tilde{I}_{\text{ext}}^r - I^B > a_0^r$:

Here $\tilde{M}_0^r > 0$ and $M^r(t) > 0$ during the time of pBötC activity, i.e., $0 \leq t \leq \Delta T_{\text{pBötC}}$, because $a^r(t)$ decreases with increasing t . From [Equations 49 and 51](#),

$$a^r(t) = a_{\text{func}}^r(t, 0, a_0^r) \quad (\text{Equation 60})$$

for $0 \leq t \leq \Delta T_{\text{pBötC}}$, where

$$a_{\text{func}}^r(t, t_{\text{begin}}, a_{\text{begin}}^r) = \frac{\beta^r J_a^r (\tilde{I}_{\text{ext}}^r - I^B)}{1 + \beta^r J_a^r} + \left[a_{\text{begin}}^r - \frac{\beta^r J_a^r (\tilde{I}_{\text{ext}}^r - I^B)}{1 + \beta^r J_a^r} \right] e^{-(1 + \beta^r J_a^r)(t - t_{\text{begin}})/\tau_a^r}. \quad (\text{Equation 61})$$

Integrating $M_r(t)$ from $t = 0$ to the integration time $T_{\text{integ}} = \Delta T_{\text{pBötC}}$ yields that the total number of spikes during the time interval $\Delta T_{\text{pBötC}}$ is

$$N_{\text{spikes}}^r = N_{\text{spikes;func}}^r(\Delta T_{\text{pBötC}}, a_0^r) \quad (\text{Equation 62})$$

where

$$\begin{aligned}
 N_{\text{spikes;func}}^r(T_{\text{integ}}; a_{\text{begin}}^r) &= \int_0^{T_{\text{integ}}} dt M^r(t) \\
 &= \frac{T_{\text{integ}} \beta^r (I_{\text{ext}}^r - I^B)}{1 + \beta^r J_a^r} \\
 &= \beta^r \left(a_{\text{begin}}^r - \frac{\beta^r J_a^r (I_{\text{ext}}^r - I^B)}{1 + \beta^r J_a^r} \right) \frac{\tau_a^r}{1 + \beta^r J_a^r} \left(1 - e^{-(1 + \beta^r J_a^r) T_{\text{integ}} / \tau_a^r} \right)
 \end{aligned}
 \tag{Equation 63}$$

The value of \hat{M}^F at time $t = 0^+$ is

$$\hat{M}^F(0^+) = \beta^F [I_{\text{ext}}^F - J^{Fr} \tau_s \beta^r (I_{\text{ext}}^r - I^B - a_0^r) - a_0^F].
 \tag{Equation 64}$$

We consider two subcases:

- **A1.** Subcase of **A** with $\hat{M}^F(0^+) \leq 0$, i.e., $I_{\text{ext}}^F - \tau_s \beta^r J^{Fr} (I_{\text{ext}}^r - I^B - a_0^r) - a_0^F \leq 0$:

Here we assume that $a_0^F = 0$, even if breathing is fast, and show that this assumption is self-consistent. Under this assumption, $\hat{M}^F(t)$ will not be larger than $\hat{M}^F(0^+)$ because a^r decreases with time and, as a result, $M^r(t) > M^r(0)$. Therefore, $a^F(\Delta T_{\text{pBötC}}) = 0$, $N_{\text{spikes}}^F = 0$, the vibrissa does not move and $\theta_{\text{max}} = 0$. During the time interval between $\Delta T_{\text{pBötC}}$ and $T_{\text{pBötC}}$, a^F only decreases (see below). Therefore, $a^F(T_{\text{pBötC}}) = 0$ and the assumption $a_0^F = 0$ is self-consistent.

- **A2.** Subcase of **A** with $\hat{M}^F(0^+) > 0$:

To compute $\hat{M}^F(t)$ for $t > 0$, we substitute $a^r(t)$ (Equation 51) and $M^r(t)$ (Equation 49) in Equations 53 and 55 and obtain

$$\begin{aligned}
 \frac{da^F}{dt} &= \frac{-a^F + \beta^F J_a^F (I_{\text{ext}}^F - \tau_s J^{Fr} M^r - a^F)}{\tau_a^F} \\
 &= -\tilde{A} a^F + \tilde{B} + \tilde{C} e^{-\tilde{D}t}
 \end{aligned}
 \tag{Equation 65}$$

where

$$\begin{aligned}
 \tilde{A} &\equiv \frac{1 + \beta^F J_a^F}{\tau_a^F}, \\
 \tilde{B} &\equiv \frac{\beta^F J_a^F}{\tau_a^F} \left[I_{\text{ext}}^F - \frac{\tau_s \beta^r J^{Fr} (I_{\text{ext}}^r - I^B)}{1 + \beta^r J_a^r} \right], \\
 \tilde{C} &\equiv \frac{\tau_s \beta^r J^{Fr} \beta^F J_a^F}{\tau_a^F} \left[a_0^r - \frac{\beta^r J_a^r (I_{\text{ext}}^r - I^B)}{1 + \beta^r J_a^r} \right], \\
 \tilde{D} &\equiv \frac{1 + \beta^r J_a^r}{\tau_a^r}.
 \end{aligned}
 \tag{Equation 66}$$

The solution of Equation 65 is

$$a^F(t) = \frac{\tilde{B}}{\tilde{A}} + \left(a_{\text{begin}}^F - \frac{\tilde{B}}{\tilde{A}} - \frac{\tilde{C}}{\tilde{A} - \tilde{D}} \right) e^{-\tilde{A}(t - t_{\text{begin}})} + \frac{\tilde{C}}{\tilde{A} - \tilde{D}} e^{-\tilde{D}(t - t_{\text{begin}})}
 \tag{Equation 67}$$

where $t_{\text{begin}} = 0$ and $a_{\text{begin}}^F = a_0^F$. The activity $\hat{M}^F(t)$ is

$$\hat{M}^F(t) = \beta^F \left\{ I_{\text{ext}}^F - J^{Fr} \tau_s \beta^r [I_{\text{ext}}^r - I^B - a^r(t)] - a^F(t) \right\}
 \tag{Equation 68}$$

where

$$a^r(t) = a_{\text{func}}^r(t, 0, a_0^r).
 \tag{Equation 69}$$

Equations 66, 67, 68, and 69 are obtained from Equations 49, 50, 51, 52, 53, 54, 55, and 62 in a self-consistent manner so long as $\hat{M}^F(t) > 0$.

We define the time $t_{M^F > 0}$ to be the end of the time interval during which $\hat{M}^F(t) > 0$, starting from $t = 0$. If

$$\hat{M}^F(\Delta T_{\text{pBötC}}) < 0, \quad (\text{Equation 70})$$

we solve the equation $\hat{M}^F(t_{M^F > 0}) = 0$ numerically and find its solution $t_{M^F > 0}$. If the inequality Equation 70 holds, $\hat{M}^F(t) \geq 0$ for $0 \leq t \leq t_{M^F > 0}$ and $\hat{M}^F(t) < 0$ for $t > t_{M^F > 0}$. Otherwise, $t_{M^F > 0} = \Delta T_{\text{pBötC}}$. The value $a^F(t_{M^F > 0})$ is given by Equation 67 for $t = t_{M^F > 0}$. If $\Delta T_{\text{pBötC}} > t_{M^F > 0}$,

$$a^F(\Delta T_{\text{pBötC}}) = a^F(t_{M^F > 0}) e^{-(T_{\text{pBötC}} - t_{M^F > 0})/\tau_a^F} \quad (\text{Equation 71})$$

The number of spikes N_{spikes}^F is computed by integrating M^F from 0 to $t_{M^F > 0}$, i.e.,

$$N_{\text{spikes}}^F = N_{\text{spikes}; M^F > 0}^F(t_{M^F > 0}, a_0^r, a_0^F) \quad (\text{Equation 72})$$

where

$$\begin{aligned} N_{\text{spikes}; M^F > 0}^F(T_{\text{integ}}, a_{\text{begin}}^r, a_{\text{begin}}^F) &= \int_0^{T_{\text{integ}}} dt M^F(t, a_{\text{begin}}^r, a_{\text{begin}}^F) \\ &= \beta^F \left\{ \int_{\text{ext}}^F T_{\text{integ}} - \frac{T_{\text{integ}} \tau_s \beta^r J_a^{Fr}}{1 + \beta^r J_a^r} (\tilde{I}_{\text{ext}} - I^B) \right. \\ &+ \frac{\tau_s \beta^r J_a^{Fr} \tau_a^r}{1 + \beta^r J_a^r} \left[a_{\text{begin}}^r - \frac{\beta^r J_a^r}{1 + \beta^r J_a^r} (\tilde{I}_{\text{ext}} - I^B) \right] \left(1 - e^{-(1 + \beta^r J_a^r) T_{\text{integ}}/\tau_a^r} \right) \\ &+ \frac{\tilde{B}}{\tilde{A}} T_{\text{integ}} + \left(a_{\text{begin}}^F - \frac{\tilde{B}}{\tilde{A}} - \frac{\tilde{C}}{\tilde{A} - \tilde{D}} \right) \frac{1}{\tilde{A}} \left(1 - e^{-\tilde{A} T_{\text{integ}}} \right) \\ &+ \left. \frac{\tilde{C}}{\tilde{D}(\tilde{A} - \tilde{D})} \left(1 - e^{-\tilde{D} T_{\text{integ}}} \right) \right\}. \end{aligned} \quad (\text{Equation 73})$$

- **B.** $0 < \tilde{I}_{\text{ext}} - I^B < a_0^r$:

Here $M^r(t) = 0$ for $0 \leq t \leq T_{M^r = 0}$, where

$$T_{M^r = 0} = \tau_a^r \log \left(\frac{a_0^r}{\tilde{I}_{\text{ext}} - I^B} \right). \quad (\text{Equation 74})$$

- **B1.** Subcase of **B** for $T_{M^r = 0} < \Delta T_{\text{pBötC}}$:

For $0 \leq t \leq T_{M^r = 0}$,

$$a^r(t) = a_0^r e^{-t/\tau_a^r}. \quad (\text{Equation 75})$$

For $T_{M^r = 0} \leq t \leq \Delta T_{\text{pBötC}}$,

$$a^r(t) = a_{\text{func}}^r(t, T_{M^r = 0}, a^r(T_{M^r = 0})). \quad (\text{Equation 76})$$

The number of spikes fired by the vIRt^{ret} during the duration of pBötC activity is

$$N_{\text{spikes}; \text{func}}^r = N_{\text{spikes}; \text{func}}^r(\Delta T_{\text{pBötC}} - T_{M^r = 0}, 0). \quad (\text{Equation 77})$$

From Equations 53 and 55, for $0 \leq t \leq T_{M^r = 0}$, we find

$$a^F(t) = a_{\text{func}}^F(t) \quad (\text{Equation 78})$$

where

$$a_{\text{func}}^F(T_{\text{integ}}) = \frac{\beta^F J_a^F \tilde{I}_{\text{ext}}^F}{1 + \beta^F J_a^F} + \left[a_0^F - \frac{\beta^F J_a^F \tilde{I}_{\text{ext}}^F}{1 + \beta^F J_a^F} \right] e^{-\tilde{A} T_{\text{integ}}} \quad (\text{Equation 79})$$

and \tilde{A} is defined by Equation 66. As described for Case A2 above, we compute $a^F(t)$ and $\hat{M}^F(t)$ for $t > T_{M^F=0}$ using Equations 67 and 68 for $t_{\text{begin}} = T_{M^F=0}$ and $a_{\text{begin}}^F = a^F(T_{M^F=0})$.

● **B1.1.** Sub-subcase of **B1** for $\hat{M}^F(\Delta T_{\text{pBötC}}) < 0$:

$a^F(T_{M^F=0})$ is given by Equations 78 and 79. We compute $t_{M^F>0}$ as described for Case A2. The value $a^F(t_{M^F>0})$ given by Equation 67 with $t_{\text{begin}} = T_{M^F=0}$ and $a_{\text{begin}}^F = a^F(T_{M^F=0})$. Lastly, $a^F(\Delta T_{\text{pBötC}})$ is computed using Equation 71.

To compute N_{spikes}^F , we first compute the number of spikes fired by vFMN neurons during the time interval $0 \leq t \leq T_{M^F=0}$, during which there is no inhibition from the vIRt^{ret} and $M^F = 0$. For this purpose, we integrate Equation 53 and use Equations 78 and 79. We add this value to the number of spikes by the vFMN neurons when there is some inhibition from the vIRt^{ret}. The sum of the spikes in these two time intervals is

$$N_{\text{spikes}}^F = N_{\text{spikes}; M^F=0}^F(T_{M^F=0}, a_0^F) + N_{\text{spikes}; M^F>0}^F(t_{M^F>0} - T_{M^F=0}, a_0^F e^{-T_{M^F=0}/\tau_a^F}, a^F(T_{M^F=0})) \quad (\text{Equation 80})$$

where

$$N_{\text{spikes}; M^F=0}^F(T_{\text{integ}}, a_{\text{begin}}^F) = \frac{\beta^F I_{\text{ext}}^F T_{\text{integ}}}{1 + \beta^F J_a^F} - \frac{\tau_a^F \beta^F}{1 + \beta^F J_a^F} \left(a_{\text{begin}}^F - \frac{\beta^F J_a^F I_{\text{ext}}^F}{1 + \beta^F J_a^F} \right) \left(1 - e^{-(1 + \beta^F J_a^F) T_{\text{integ}} / \tau_a^F} \right). \quad (\text{Equation 81})$$

● **B1.2.** Sub-subcase of **B1** for $\hat{M}^F(\Delta T_{\text{pBötC}}) \geq 0$:

Here $a^F(T_{M^F=0})$ is given by Equations 78 and 79, and $a^F(\Delta T_{\text{pBötC}})$ is given by Equation 67 with $t_{\text{begin}} = T_{M^F=0}$ and $a_{\text{begin}}^F = a^F(T_{M^F=0})$. N_{spikes}^F is given by the equation

$$N_{\text{spikes}}^F = N_{\text{spikes}; M^F=0}^F(T_{M^F=0}, a_0^F) + N_{\text{spikes}; M^F>0}^F(\Delta T_{\text{pBötC}} - T_{M^F=0}, a_0^F e^{-t_{M^F=0}/\tau_a^F}, a^F(T_{M^F=0})). \quad (\text{Equation 82})$$

● **B2.** Subcase of **B** for $T_{M^F=0} \geq \Delta T_{\text{pBötC}}$:

Here

$$a^r(\Delta T_{\text{pBötC}}) = a_0^r e^{-\Delta T_{\text{pBötC}} / \tau_a^r}, \quad (\text{Equation 83})$$

$$a^F(\Delta T_{\text{pBötC}}) = a_{\text{func}}^F(\Delta T_{\text{pBötC}}), \quad (\text{Equation 84})$$

where $a_{\text{func}}^F(\Delta T_{\text{pBötC}})$ is given by Equation 79 and

$$N_{\text{spikes}}^r = 0, \quad (\text{Equation 85})$$

$$N_{\text{spikes}}^F = N_{\text{spikes}; M^F=0}^F(\Delta T_{\text{pBötC}}, a_0^F), \quad (\text{Equation 86})$$

where $N_{\text{spikes}; M^F=0}^F(\Delta T_{\text{pBötC}}, a_0^F)$ is given by Equation 81.

● **C.** Case of $I_{\text{ext}}^r - I^B < 0$

$a^r(\Delta T_{\text{pBötC}})$, $a^F(\Delta T_{\text{pBötC}})$, N_{spikes}^r , and N_{spikes}^F are given by Equations 83, 84, 85, and 86 respectively.

● In all cases (**A-C**), the value of $a^r(T_{\text{pBötC}})$ is

$$a^r(T_{\text{pBötC}}) = \frac{\beta^r J_a^r I_{\text{ext}}^r}{1 + \beta^r J_a^r} + \left[a_0^r(\Delta T_{\text{pBötC}}) - \frac{\beta^r J_a^r I_{\text{ext}}^r}{1 + \beta^r J_a^r} \right] e^{-(1 + \beta^r J_a^r)(T_{\text{pBötC}} - \Delta T_{\text{pBötC}}) / \tau_a^r}. \quad (\text{Equation 87})$$

Since we consider the case where $M^F = 0$ when the pBötC is silent, i.e., for $\Delta T_{\text{pBötC}} < t \leq T_{\text{pBötC}}$,

$$a^F(T_{\text{pBötC}}) = a^F(\Delta T_{\text{pBötC}}) e^{-(T_{\text{pBötC}} - \Delta T_{\text{pBötC}}) / \tau_a^F}. \quad (\text{Equation 88})$$

Analytical calculation of the vibrissa set-point angle at rest and at saturation for the pBötC-vIRt^{ret}-vFMN circuit

We compute the onset value of I^B , I_{onset}^B , above which the vibrissae start to oscillate, along with the saturation value I_{sat}^B above which the whisking amplitude saturates at a maximum value (Figure 3H). We perform this calculation for low-frequency whisking, for which the values of the adaptation a_0^r and a_0^f are given by Equations 58 and 59.

- The vibrissae are at rest ($\theta = 0$) if $\hat{M}^F \leq 0$ during the whole period of pBötC activity. Since a^r decreases and M^r increases with time after the onset of pBötC activity (Equation 62), we look for the value of I^B value for which $\hat{M}^F(0^+) = 0$. From Equation 53, this means that

$$\tilde{I}_{\text{ext}}^F - J^{Fr} \tau_s \hat{M}^F(0^+) = 0. \quad (\text{Equation 89})$$

Substituting Equation 49 and the steady-state value of s^r (Equation 50) in Equation 89, we find that the value I^B above which M^F is not indentially zero and the vibrissa starts to oscillate is:

$$I_{\text{onset}}^B = \tilde{I}_{\text{ext}}^r - a_0^r - \frac{\tilde{I}_{\text{ext}}^F}{\tau_s \beta^r J^{Fr}}. \quad (\text{Equation 90})$$

- The saturation value of the amplitude of θ during rhythmic whisking is obtained for the I^B value above which $T_{M^r=0} = \Delta T_{\text{pBötC}}$ (Equation 74). Using Equations 53, 59, and 79 for $M^r = 0$, we obtain

$$M^F(t) = \beta^F \tilde{I}_{\text{ext}}^F \left[1 + \frac{\beta^F J_a^F}{1 + \beta^F J_a^F} e^{-\tilde{\Gamma}t} \right]. \quad (\text{Equation 91})$$

where

$$\tilde{\Gamma} = \frac{1 + \beta^F J_a^F}{\tau_a^F}. \quad (\text{Equation 92})$$

- The dependency of the force term on M^F is nonlinear (Equations 43 and 45). Yet we can approximate it by linear dependency

$$\frac{d\theta}{dt} = -\frac{\theta}{\tau_{wm}} + F_m M^F \quad (\text{Equation 93})$$

where F_m is a proportionality constant.

- The time $T_{\theta, \text{max}}$ for maximal protraction is determined by calculating the maximal value of $\theta(t)$ computed by solving Equations 91, 92, and 93 for the initial condition $\theta(0) = 0$. This time is found to be independent of F_m , i.e.,

$$T_{\theta, \text{max}} = \frac{\tau_{wm}}{\tilde{\Gamma} \tau_{wm} - 1} \log \left[\frac{\beta^F J_a^F \tilde{\Gamma} \tau_{wm}}{1 + \beta^F J_a^F - \tilde{\Gamma} \tau_{wm}} \right]. \quad (\text{Equation 94})$$

This calculation is valid if $T_{\theta, \text{max}} \leq \Delta T_{\text{pBötC}}$. Otherwise, we replace $T_{\theta, \text{max}}$ with $\Delta T_{\text{pBötC}}$.

- To compute the value I_{sat}^B above which saturation is obtained, we look for the value of I^B for which $M^r(t) = 0$ for $0 \leq t \leq T_{\theta, \text{max}}$ based on self-consistency. Since $M^r = 0$ for this time interval, $a^r = a_0^r e^{-t/\tau^r}$ (Equation 51). Note that so long as (Equation 49 and 58)

$$\tilde{I}_{\text{ext}}^r - I^B - \frac{\beta^r J_a^r \tilde{I}_{\text{ext}}^r}{1 + \beta^r J_a^r} e^{-t/\tau_a^r} \leq 0, \quad (\text{Equation 95})$$

we have $M^r = 0$ and

$$I_{\text{sat}}^B = \tilde{I}_{\text{ext}}^r \left(1 - \frac{\beta^r J_a^r \tilde{I}_{\text{ext}}^r}{1 + \beta^r J_a^r} e^{-T_{\theta, \text{max}}/\tau_a^r} \right). \quad (\text{Equation 96})$$

- The value of M^F at saturation is computed by substituting $t = T_{\theta, \text{max}}$ in Equation 91. The whisking amplitude at saturation is given by the steady-state value of Equation 46, $\theta_{\text{max}} = \tau_{wm} F_{\text{fit}}(M_{\text{sat}}^F)$.

Analytical solution of the rate model for the vIRt^{ret}-vIRt^{pro} circuit

The dynamics of the two vIRt sub-population are described in terms of the population-averaged synaptic variables (Equation 35) and adaptation variables (Equation 36). In our analysis, we take $\beta^r = \beta^p$ for simplicity.

- For the case of a symmetric circuit composed of two vIRt sub-populations without pBötC input, this description involves four differential equations:

$$\begin{aligned} s^r &= -\frac{s^r}{\tau_s} + M^r \\ &= -\frac{s^r}{\tau_s} + \beta^r \left[\tilde{I}_{\text{ext}}^r - J_{\text{intra}} s^r - J_{\text{inter}} s^p - a^r \right]_+, \end{aligned} \quad (\text{Equation 97})$$

$$a^r = \frac{-a^r + J_a^r \beta^r \left[\tilde{I}_{\text{ext}}^r - J_{\text{intra}} s^r - J_{\text{inter}} s^p - a^r \right]_+}{\tau_a^r}, \quad (\text{Equation 98})$$

$$\begin{aligned} s^p &= -\frac{s^p}{\tau_s} + M^p \\ &= -\frac{s^p}{\tau_s} + \beta^r \left[\tilde{I}_{\text{ext}}^r - J_{\text{inter}} s^r - J_{\text{intra}} s^p - a^p \right]_+, \end{aligned} \quad (\text{Equation 99})$$

$$a^p = \frac{-a^p + J_a^r \beta^r \left[\tilde{I}_{\text{ext}}^r - J_{\text{inter}} s^r - J_{\text{intra}} s^p - a^p \right]_+}{\tau_a^r}. \quad (\text{Equation 100})$$

Several types of fixed-point (FP) solutions are possible for Equations 97 through 100.

- **Uniform state:** Neurons in the two subpopulations spike at the uniform state, for which $M^p > 0$ and $M^r > 0$ with Soloduchin and Shamir (2018):

$$\begin{aligned} M^r &= M^p \\ &= \frac{\beta^r \tilde{I}_{\text{ext}}^r}{1 + \beta^r J_a^r + \tau_s \beta^r (J_{\text{intra}} + J_{\text{inter}})}. \end{aligned} \quad (\text{Equation 101})$$

If $\tilde{I}_{\text{ext}}^r < J_a^r \tau_s M^r$ (Equations 53 and 55), $M^r = 0$ and the set-point vibrissa angle, θ_{max} , is zero. Otherwise,

$$M^r = \frac{\beta^r \left(\tilde{I}_{\text{ext}}^r - \tau_s J_a^r M^r \right)}{1 + \beta^r J_a^r}. \quad (\text{Equation 102})$$

The stability matrix of this FP is determined by considering the vIRt circuit only (Equations 97, 98, 99, and 100):

$$A_{\text{stab}} = - \begin{pmatrix} \frac{1}{\tau_s} + \beta^r J_{\text{intra}} & \beta^r & \beta^r J_{\text{inter}} & 0 \\ \frac{\beta^r J_a^r J_{\text{intra}}}{\tau_a^r} & \frac{1 + \beta^r J_a^r}{\tau_a^r} & \frac{\beta^r J_a^r J_{\text{inter}}}{\tau_a^r} & 0 \\ \beta^r J_{\text{inter}} & 0 & \frac{1}{\tau_s} + \beta^r J_{\text{intra}} & \beta^r \\ \frac{\beta^r J_a^r J_{\text{inter}}}{\tau_a^r} & 0 & \frac{\beta^r J_a^r J_{\text{intra}}}{\tau_a^r} & \frac{1 + \beta^r J_a^r}{\tau_a^r} \end{pmatrix}. \quad (\text{Equation 103})$$

Substituting eigenvectors of the form $(\vec{a}, \pm \vec{a})^T$, where \vec{a} is a two-dimensional vector, yields two, 2x2 matrices:

$$A_{\text{stab}, \pm} = - \begin{pmatrix} \frac{1}{\tau_s} + \beta^r (J_{\text{intra}} \pm J_{\text{inter}}) & \beta^r \\ \frac{\beta^r J_a^r}{\tau_a^r} (J_{\text{intra}} \pm J_{\text{inter}}) & \frac{1 + \beta^r J_a^r}{\tau_a^r} \end{pmatrix}. \quad (\text{Equation 104})$$

Stability depends on the two eigenvalues having negative real parts, which implies that the anti-symmetric mode $(\vec{a}, -\vec{a})^T$ is the least stable. The conditions for receiving two eigenvalues with negative real parts are $\text{Tr}(A_{\text{stab}, -}) < 0$ and $\text{Det}(A_{\text{stab}, -}) > 0$, for which:

$$J_{\text{inter}} - J_{\text{intra}} < J_{\text{tr}} \quad (\text{Equation 105})$$

with

$$J_{\text{tr}} \equiv \frac{1}{\beta^r} \left(\frac{1}{\tau_s} + \frac{1}{\tau_a^r} + \frac{\beta^r J_a^r}{\tau_a^r} \right) \quad (\text{Equation 106})$$

and

$$J_{\text{inter}} - J_{\text{intra}} < J_{\text{det}} \quad (\text{Equation 107})$$

with

$$J_{\text{det}} \equiv \frac{1 + \beta^r J_a^r}{\beta^r \tau_s} \quad (\text{Equation 108})$$

If $\tau_s \ll \tau_a^r$ then $J_{\text{tr}} < J_{\text{det}}$, and the uniform FP will become unstable when $J_{\text{inter}} - J_{\text{intra}}$ increases above J_{tr} . Since $J_{\text{tr}} > 0$, J_{inter} should be larger than J_{intra} to destabilize the FP.

- **Bistable state:** Two stable symmetric FP coexists in the bistable state, one with $M^P > 0$ and $M^r = 0$, and the second with $M^r > 0$ and $M^P = 0$. In the first case,

$$M^P = \frac{\beta^r \tilde{I}_{\text{ext}}^r}{1 + \beta^r J_a^r + \tau_s \beta^r J_{\text{intra}}} \quad (\text{Equation 109})$$

is nonzero if $\tilde{I}_{\text{ext}}^r - J_{\text{inter}} s^P < 0$. From Equation 109, this condition becomes

$$J_{\text{inter}} - J_{\text{intra}} > \frac{1 + \beta^r J_a^r}{\beta^r \tau_s} \quad (\text{Equation 110})$$

or, from Equation 108,

$$J_{\text{inter}} - J_{\text{intra}} > J_{\text{det}}. \quad (\text{Equation 111})$$

With $M^r = 0$, the value of M^F for $\tilde{I}_{\text{ext}}^F > 0$ (Equations 53 and 55),

$$M^F = \frac{\beta^F \tilde{I}_{\text{ext}}^F}{1 + \beta^F J_a^F} \quad (\text{Equation 112})$$

For the other bistable state ,

$$M^r = \frac{\beta^r \tilde{I}_{\text{ext}}^r}{1 + \beta^r J_a^r + \tau_s \beta^r J_{\text{intra}}} \quad (\text{Equation 113})$$

and $M^P = 0$. Similar to the uniform case, $\theta_{\text{max}} = 0$ if $\tilde{I}_{\text{ext}}^F < J_{\text{tr}}^F M^r$. Otherwise, M^F is determined by Equation 102, and there is bistability of two protracted values of θ_{max} as a result of the vIRt dynamics, determined by Equation 46.

- **Oscillatory state:** This is the state of interest for whisking. No stable FP is found for $J_{\text{inter}} - J_{\text{intra}}$ between J_{tr} (Equation 106) and J_{det} (Equations 108 and 110). A limit cycle exists in this regime, in which the two vIRt subpopulations spike in alternation. Each population is active during a half time period $T_{\text{vIRt}}/2$, and is silent during the following half time period.
 - Following Soloduchin and Shamir (2018), we compute the amplitude and T_{vIRt} of the system in the limit $\tau_s \ll \tau_a^r$. We define the time $t=0$ as the time when the vIRt^{ret} subpopulation begins to be active and the vIRt^{pro} subpopulation becomes silent. During the time interval $0 \leq t \leq T_{\text{vIRt}}/2$, the active state of vIRt^{ret} subpopulation, s^r , reaches a quasi-steady-state value that evolves on the slow time-scale of order τ_a^r according to

$$s^r(t) = \frac{\tau_s \beta^r [\tilde{I}_{\text{ext}}^r - a^r(t)]}{1 + \tau_s \beta^r J_{\text{intra}}} \quad (\text{Equation 114})$$

The adaptation variable a^r evolves according to Equations 36 and 114, i.e.,

$$\dot{a}^r = \frac{\tilde{J}^r}{\tau_a^r} - \frac{1 + \tilde{J}^r}{\tau_a^r} a^r \quad (\text{Equation 115})$$

where

$$\tilde{J} \equiv \frac{\beta^r J_a^r}{1 + \tau_s \beta^r J_{intra}^r}. \quad (\text{Equation 116})$$

Defining $a_0^r = a^r(t = 0)$, the solution of Equation 115 is

$$a^r(t) = \frac{\tilde{J}}{1 + \tilde{J}} \tilde{I}_{ext}^r + \left(a_0^r - \frac{\tilde{J}}{1 + \tilde{J}} \tilde{I}_{ext}^r \right) e^{-(1 + \tilde{J})t / \tau_a^r}. \quad (\text{Equation 117})$$

The spiking rate is $M^r = 0$ during the time interval $T_{vIRt}/2 \leq t \leq T_{vIRt}$ and leads to

$$a^r(t) = a^r\left(\frac{T_{vIRt}}{2}\right) e^{-(t - T_{vIRt}/2) / \tau_a^r}. \quad (\text{Equation 118})$$

Using periodicity, i.e., $a^r(T_{vIRt}) = a_0^r$, we obtain

$$a_0^r = \frac{\tilde{J}}{1 + \tilde{J}} \frac{e^{-T_{vIRt}/(2\tau_a^r)} - e^{-(2 + \tilde{J})T_{vIRt}/(2\tau_a^r)}}{1 - e^{-(2 + \tilde{J})T_{vIRt}/(2\tau_a^r)}} \tilde{I}_{ext}^r \quad (\text{Equation 119})$$

and, together with Equation 117, we obtain

$$a_r(T_{vIRt}/2) = \frac{\tilde{J}}{1 + \tilde{J}} \tilde{I}_{ext}^r + \left(a_0^r - \frac{\tilde{J}}{1 + \tilde{J}} \tilde{I}_{ext}^r \right) e^{-(1 + \tilde{J})T_{vIRt}/(2\tau_a^r)}. \quad (\text{Equation 120})$$

To compute T_{vIRt} , we utilize the switch in M^p from zero to a positive value at $t = T_{vIRt}/2$ and the relation $a^p(T_{vIRt}/2) = a_0^p$, i.e.,

$$\tilde{I}_{ext}^r - J_{inter} s^r(T_{vIRt}/2) - a_0^r = 0. \quad (\text{Equation 121})$$

Inserting Equation 114 into Equation 121 leads to an equation for a_0^r , i.e.,

$$\tilde{I}_{ext}^r - J_{inter} \frac{\tau_s \beta^r}{1 + \tau_s \beta^r J_{intra}^r} \left[\tilde{I}_{ext}^r - a^r(T_{vIRt}/2) \right] - a_0^r = 0. \quad (\text{Equation 122})$$

The combination of Equations 119, 120, and 122 define an implicit transcendental relation for the bursting T_{vIRt} of the vIRt oscillator, i.e.,

$$J_{inter} = \frac{1 + \tau_s \beta^r J_{intra}^r}{\tau_s \beta^r} \times \frac{(1 + \beta^r J_a^r + \tau_s \beta^r J_{intra}^r) \left[1 - e^{-(2 + \tilde{J})T_{vIRt}/(2\tau_a^r)} \right] - \beta^r J_a^r \left[1 - e^{-(1 + \tilde{J})T_{vIRt}/(2\tau_a^r)} \right] e^{-T_{vIRt}/(2\tau_a^r)}}{(1 + \beta^r J_a^r + \tau_s \beta^r J_{intra}^r) \left[1 - e^{-(2 + \tilde{J})T_{vIRt}/(2\tau_a^r)} \right] - \beta^r J_a^r \left[1 - e^{-(1 + \tilde{J})T_{vIRt}/(2\tau_a^r)} \right]} \quad (\text{Equation 123})$$

Equation 123 can be written in terms of two dimensionless parameters, \tilde{J} and $\tau_s J_{inter} / J_a^r$, and the ratio $T_{vIRt} / 2\tau_a^r$:

$$\frac{\tau_s J_{inter} \tilde{J}}{J_a^r} = \frac{\left(\frac{1 + \tilde{J}}{\tilde{J}} \right) \left[1 - e^{-(2 + \tilde{J})T_{vIRt}/(2\tau_a^r)} \right] - \left[1 - e^{-(1 + \tilde{J})T_{vIRt}/(2\tau_a^r)} \right] e^{-T_{vIRt}/(2\tau_a^r)}}{\left(\frac{1 + \tilde{J}}{\tilde{J}} \right) \left[1 - e^{-(2 + \tilde{J})T_{vIRt}/(2\tau_a^r)} \right] - \left[1 - e^{-(1 + \tilde{J})T_{vIRt}/(2\tau_a^r)} \right]} \quad (\text{Equation 124})$$

The period scales linearly with τ_a^r . It is independent of the effective input, \tilde{I}_{ext}^r .

- For $T_{vIRt} \rightarrow \infty$, Equations 119 and 120 yield

$$a_0^r = 0 \quad (\text{Equation 125})$$

and

$$a^r(T_{vIRt}/2) = \frac{\tilde{J}}{1 + \tilde{J}} \tilde{I}_{ext}^r. \quad (\text{Equation 126})$$

Substituting Equations 114, 116, and 125 in Equation 121, we obtain

$$J_{inter} - J_{intra} = \frac{1 + \beta^r J_a^r}{\beta^r \tau_s}. \quad (\text{Equation 127})$$

The period T_{vIRt} diverges at the maximal value that $J_{inter} - J_{intra}$ may take for a limit cycle. Above that value, the system settles in a bistable state (Equation 110).

- For $T_{vIRt} \ll \tau_a^r$, Equation 119 yields

$$a_0^r = \frac{\tilde{J}}{2 + \tilde{J}} \tilde{I}_{\text{ext}}^r. \quad (\text{Equation 128})$$

Substituting this value in Equation 122 and using Equation 120, the condition for receiving very small T_{vIRt} becomes

$$J_{\text{inter}} - J_{\text{intra}} = \frac{1}{\beta^r \tau_s}. \quad (\text{Equation 129})$$

This condition coalesces with Equation 106 for $\tau_s \ll \tau_a^r$. Thus for $J_{\text{inter}} - J_{\text{intra}}$ just above the value where the uniform state becomes unstable, a limit cycle with a very short time period, on the time scale of τ_a^r , will emerge.

- To compute the total number of spikes fired by a neuron during the active phase, we substitute Equations 114 and 117 in Equation 97. For the half-cycle for which the vIRt^{ret} subpopulation is active, we obtain

$$M^r(t) = \frac{\beta^r}{1 + \tau_s \beta^r J_{\text{intra}}} \left[\frac{\tilde{I}_{\text{ext}}^r}{1 + \tilde{J}} - \left(a_0^r - \frac{\tilde{J}}{1 + \tilde{J}} \tilde{I}_{\text{ext}}^r \right) e^{-(1+\tilde{J})t/\tau_a^r} \right]. \quad (\text{Equation 130})$$

Using Equation 119 and knowledge that the spike rate is $M^r = 0$ for $T_{\text{vIRt}}/2 \leq t \leq T_{\text{vIRt}}$, we find that the time-average spike rate $\langle M^r(t) \rangle_t$ is given by

$$\begin{aligned} \langle M^r(t) \rangle_t &= \frac{1}{T_{\text{vIRt}}} \int_0^{T_{\text{vIRt}}} dt M^r(t) \\ &= \frac{1}{2} \frac{\tilde{J}}{1 + \tilde{J}} \frac{\tilde{I}_{\text{ext}}^r}{J_a^r} \\ &\times \left\{ 1 + \frac{\tilde{J}}{1 + \tilde{J}} \left(\frac{2\tau_a^r}{T_{\text{vIRt}}} \right) \frac{\left[1 - e^{-T_{\text{vIRt}}/(2\tau_a^r)} \right] \left[1 - e^{-(1+\tilde{J})T_{\text{vIRt}}/(2\tau_a^r)} \right]}{\left[1 - e^{-(2+\tilde{J})T_{\text{vIRt}}/(2\tau_a^r)} \right]} \right\}. \end{aligned} \quad (\text{Equation 131})$$

Note that $\langle M^r(t) \rangle_t$ is proportional to \tilde{I}_{ext}^r .

The oscillation period T_{vIRt} increases monotonically with J_{inter}

We show that T_{vIRt} increases monotonically with increasing values of J_{inter} for $T_{\text{vIRt}} > 0$.

- We write Equation 124 in terms of normalized variables, i.e.,

$$J_{\text{nor}} = \frac{1 - \tilde{E}(T_{\text{vIRt}}) e^{-T_{\text{vIRt}}/(2\tau_a^r)}}{1 - \tilde{E}(T_{\text{vIRt}})} \quad (\text{Equation 132})$$

where

$$J_{\text{nor}} \equiv \frac{\tau_s J_{\text{inter}} \tilde{J}}{J_a^r} \quad (\text{Equation 133})$$

and

$$\tilde{E}(T_{\text{vIRt}}) = \frac{\tilde{J}}{1 + \tilde{J}} \frac{1 - e^{-(1+\tilde{J})T_{\text{vIRt}}/(2\tau_a^r)}}{1 - e^{-(2+\tilde{J})T_{\text{vIRt}}/(2\tau_a^r)}}. \quad (\text{Equation 134})$$

Clearly, $0 < \tilde{E}(T_{\text{vIRt}}) < 1$.

- We show that $\tilde{E}(T_{\text{vIRt}})$ increases with T_{vIRt} . Differentiating $\tilde{E}(T_{\text{vIRt}})$ with respect to T_{vIRt} , we obtain

$$\frac{d\tilde{E}(T_{\text{vIRt}})}{dT_{\text{vIRt}}} = \frac{\tilde{J}}{2\tau_a^r (1 + \tilde{J})} \frac{e^{-(1+\tilde{J})T_{\text{vIRt}}/(2\tau_a^r)}}{\left[1 - e^{-(2+\tilde{J})T_{\text{vIRt}}/(2\tau_a^r)} \right]^2} \tilde{F}(T_{\text{vIRt}}) \quad (\text{Equation 135})$$

where

$$\tilde{F}(T_{\text{vIRt}}) = \left[(1 + \tilde{J}) - (2 + \tilde{J}) e^{-T_{\text{vIRt}}/(2\tau_a^r)} + e^{-(2+\tilde{J})T_{\text{vIRt}}/(2\tau_a^r)} \right] \quad (\text{Equation 136})$$

Therefore, we need to show that $\tilde{F}(T_{\text{vIRt}}) > 0$ for positive T_{vIRt} . We note that

$$\tilde{F}(0) = 0 \quad (\text{Equation 137})$$

Differentiating Equation 136 with respect to T_{vIRt} , we obtain

$$\frac{d\tilde{F}(T_{\text{vIRt}})}{dT_{\text{vIRt}}} = \frac{2 + \tilde{J}}{2\tau_a^r} e^{-T_{\text{vIRt}}/(2\tau_a^r)} \left[1 - e^{-(1+\tilde{J})T_{\text{vIRt}}/(2\tau_a^r)} \right] \quad (\text{Equation 138})$$

This means that $d\tilde{F}(T_{\text{vIRt}})/dT_{\text{vIRt}} > 0$ for $T_{\text{vIRt}} > 0$, $\tilde{F}(T_{\text{vIRt}})$ is an increasing function of T_{vIRt} , and, because of Equation 137, is positive. We have therefore shown that $d\tilde{E}(T_{\text{vIRt}})/dT_{\text{vIRt}} > 0$ for $T_{\text{vIRt}} > 0$

- To show that $dJ_{\text{nor}}/dT_{\text{vIRt}} > 0$, we differentiate Equation 132 with respect to T_{vIRt} and obtain

$$\frac{dJ_{\text{nor}}}{dT_{\text{vIRt}}} = \frac{\frac{d\tilde{E}}{dT_{\text{vIRt}}} \left[1 - e^{-T_{\text{vIRt}}/(2\tau_a^r)} \right] + \frac{\tilde{E}}{2\tau_a^r} e^{-T_{\text{vIRt}}/(2\tau_a^r)} (1 - \tilde{E})}{\left[1 - \tilde{E}(T_{\text{vIRt}}) \right]^2} \quad (\text{Equation 139})$$

Since, $d\tilde{E}/dT_{\text{vIRt}} > 0$ and $0 < \tilde{E} < 1$ for $T_{\text{vIRt}} > 0$, the numerator is positive, $dJ_{\text{nor}}/dT_{\text{vIRt}} > 0$. From Equations 132 and 133, we obtain that $dT_{\text{vIRt}}/dJ_{\text{inter}} > 0$.

Numerical methods details

Simulations of the conductance-based model were performed using the fourth-order Runge-Kutta method with time step $\Delta t = 0.01$ ms. Simulations with smaller Δt reveal similar statistics of neuronal spiking patterns, such as spike rates M , averaged over many whisking cycles, or CV_2 . Differences between individual voltage time courses, however, diverged over large integration time interval. Statistics were computed after removing an initial transient of 1 s, over an interval of 6 s (Figures 2C, 2D, 3B–3D, 3F–3H, 4B–4D, 4F–4H, 5B–5M, 6A–6F, 8B–8D and S2B–S2K) or 60 s (Figures 7D, 7E, 7F, S3A–S3D, and S4A–S4C). In numerical experiments to establish the dependence on system parameters (Figures 3F–3H, 5B–5M, 6D–6F, 7E, 7F, 8B–8D, and S2B–S2K), each data point is computed by averaging over five network realizations.

Simulations of the rate model (Figures 3H, 5D, 5E, 5H, 5I, S1, S2B–S2I, and S5) were performed using the fourth-order Runge-Kutta method with time step $\Delta t = 0.02$ ms.

Experimental methodological details for rats

Two, female Long Evans rats, aged 9 months and approximately 350 g, were maintained in standard cages on a natural light-dark cycle. For surgery, rats were anesthetized with isoflurane (Butler Schein). Body temperature was monitored and maintained at 37°C. Subcutaneous injections of 5 % (w/v) glucose in saline were given every 2 h for rehydration. Buprenorphine (0.02 mg/kg; Butler Schein) was administered i.p. for post-operative analgesia. These procedures are an extension of those in past studies (Hill et al., 2011).

Breathing signals were acquired by measuring respiration-related temperature changes. We implanted a thermistor (GAG22K7MCD419, TE Connectivity) in the nasal cavity (McAfee et al. (2016)). The change in temperature leads to a change in resistance of the thermistor, and was converted to a the period of a digital pulse generator a CMOS timers (ICM7555 in as-table mode, Renesas electronics). The clock's pulse period is thus proportional to the change in nasal cavity temperature. The timer signal pulse train was sampled at 20 kHz and logged on a computer using the LabChart acquisition system (AD Instruments). The pulse frequency is measured by detecting individual pulses' onset and converting inter-pulse intervals to the frequency. The underlying signal was filtered between 1 and 15 Hz with a 3-pole Butterworth filter that was run backwards and forwards in time.

Head and vibrissa movements were recorded using a high-speed video camera (Basler axA204 -90umNIR). A 1445 by 485 pixel (24.5 cm × 8.2 cm) area was captured at 350 frames/s. During the recording sessions all vibrissae except C1, C2, and C3 were trimmed. The animal's head and the nose were marked by adhering a two white ellipsoidal beads, 5.4 mm long by 3.8 mm diameter, to the skin surface parallel to the rostro-caudal axis of the rat's head using super glue (Loctite 495). The markers' placement improved the robustness of the tracking algorithm (Clack et al., 2012; Mathis et al., 2018) and facilitated intrasubject comparisons. After successfully tracking the head and nose position, in each frame, the orientation angle and head markers position was used to place a square (500×500 pixel) region of interest around the animal's head. After further cropping, the underlying image is split in half, i.e., right and left part of the face, to make it compatible with a vibrissa tracking algorithm (Clack et al., 2012).

QUANTIFICATION AND STATISTICAL ANALYSIS

Vibrissa tracking

We used DeepLabCut (Mathis et al., 2018) to detect the position of each individual vibrissa base in single frame. Custom written scripts in MATLAB (MathWorks) and Python 3.6.9 were used to carry out and combine various tracking steps.

Population- and time-averaged quantities

The model parameter M_μ is the time-averaged spike rates of all the neurons in the μ -th subpopulation, where averaging occurs over many whisking cycles at the oscillatory state. We characterize several dynamical states of the vIRt subpopulations without pBötC input (Figure 5). In the *silent* state, neurons in the two subpopulations do not spike. In the *uniform* state, neurons in the two subpopulations spike tonically. In the *bistable* state, one subpopulation is active and neurons spike tonically, and the second subpopulation is silent. This state coexists with another state in which the two subpopulations switch roles. In the *oscillatory* state, the two subpopulations are active and silent alternately and neurons exhibit bursting behavior.

To find out if an active network is in an oscillatory state, we compute the maximal inter-spike interval (ISI) for each neuron in a subpopulation, and $ISI_{\max, \text{median}}^\mu$ denotes the median, over the subpopulation, of the maximum ISI for all of the neurons in the population. If, for the two vIRt subpopulations, $ISI_{\max, \text{median}}^\mu$ is larger than twice the average ISI of these subpopulations, the vIRt network is considered to exhibit bursting. Otherwise, it is considered to be tonically spiking. The subpopulation-bursting time period T_{vIRt} is determined based on auto- and cross-correlation analysis of the subpopulation spiking activity.

For tonic spiking, the coefficients of variation of and $CV_{2,j}^\mu$ of the i -th neuron in the μ -th subpopulation are computed from the definition of CV_2 of a neuron (Holt et al., 1996). In bursting states, ISI are included in the calculation of $CV_{2,j}^\mu$ only if they are smaller than $0.4T_{\text{vIRt}}$. By doing this, we consider the variation of ISIs only within each burst, and exclude ISIs that belong to different bursts. Therefore, neurons that do not have at least one burst with 3 spikes do not have a defined $CV_{2,j}^\mu$ value. The value $CV_{2,j}^\mu$ is calculated by averaging $CV_{2,j}^\mu$ over all the neurons in the μ -th subpopulation for which this value is defined.

Extracting whisking amplitudes

We extract the amplitude of the successive whisking amplitudes within a breathing cycle from simulations by comparing the vibrissa trace $\theta(t)$ with the initiation times of the pBötC activity $t_{\text{pBötC},j}$. We begin by computing the standard deviation of $\theta(t)$, θ_{sd} , along the entire simulation time interval, and the global minimum of $\theta(t)$, obtained in $t_{w,\min}$. We then begin from the time of the global minimum, and search for the local maxima and minima of $\theta(t)$ alternately for either smaller or larger than $t_{w,\min}$. We consider only the local extrema that their absolute difference from the previous extrema is larger than $0.8 \times \theta_{\text{sd}}$ ($0.1 \times \theta_{\text{sd}}$) (Figures 5M, 8B, and 8C). For each pBötC cycle starting at $t_{\text{pBötC},j}$, we find all the whisks such that their maximal angle, θ , occurs between $t_{\text{pBötC},j}$ and $t_{\text{pBötC},j+1}$, and these whisks are defined to belong to this breathing cycle. The whisk amplitude is half of the difference between the values of θ at its local maximal value and at the previous local minimal value.

Similar calculations are carried out for whisking signals obtained experimentally. Following (Moore et al., 2013), the initiation time of the pBötC activity measured experimentally, $t_{\text{pBötC},j}$, are defined to precede the maximal value of the breathing signal from the thermocouple by 30 ms.